1-1-2013

The Effect Of Tangential Velocity Component In Abrasive Jet Micro-Machining Of Borosilicate Glass

Md. A. Hasem
Ryerson University

THE EFFECT OF TANGENTIAL VELOCITY COMPONENT IN ABRASIVE JET MICRO-MACHINING OF BOROSILICATE GLASS

by

Md. Abul Hasem, B.Eng.

Ryerson University, Toronto, Ontario, Canada, 2010

A thesis

presented to Ryerson University

in partial fulfillment of the

requirements for the degree of

Master of Applied Science

in the program of

Mechanical and Industrial Engineering

Toronto, Ontario, Canada, 2013

AUTHOR’S DECLARATION

AUTHOR'S DECLARATION FOR ELECTRONIC SUBMISSION OF A THESIS

I hereby declare that I am the sole author of this thesis. This is a true copy of the thesis, including any required final revisions, as accepted by my examiners.

I authorize Ryerson University to lend this thesis to other institutions or individuals for the purpose of scholarly research.

I further authorize Ryerson University to reproduce this thesis by photocopying or by other means, in total or in part, at the request of other institutions or individuals for the purpose of scholarly research.

I understand that my thesis may be made electronically available to the public.

ABSTRACT

THE EFFECT OF TANGENTIAL VELOCITY COMPONENT IN ABRASIVE JET MICRO-MACHINING OF BOROSILICATE GLASS

Master of Applied Science, Mechanical Engineering, 2013, Md. Abul Hasem

Yeates School of Graduate Studies, Ryerson University

Generally two types of erosion testers are used in solid particle erosion testing: air blast erosion testers and mechanically powered erosion testers. In the first portion of this thesis, the feasibility of implementing a mechanically powered erosion tester for abrasive jet micro-machining applications using very small particles was studied. It was found that, due to the ultrahigh vacuum requirement, such a device would not be practical. Therefore, in the second part of the thesis, the designed rotary mechanism was utilized as a rotary disc target holder apparatus and blasted with a typical air blast system. The apparatus could add or deduct a tangential velocity component into the system, allowing for detailed studies of the effect that the tangential velocity component has on the erosion of borosilicate glass using 25-150 μm aluminum oxide particles. Although the tangential velocity effect has been ignored for brittle materials by most researchers, the present results show that it can have an important role in erosion rate.

Acknowledgements

I would like to convey sincere gratitude to my supervisor Dr. Marcello Papini for his guidance, motivation, and continuous support during my graduate studies. This thesis could not have been written without his sound advice and immense guidance.

I owe gratitude to Joseph Amankrah, Devin Ostrom, Alan Machin and Chao Ma for their technical support during this research.

I am very thankful to my wife, Trisha, for her immense patience and emotional support. Without her encouragement and understanding, it would have been impossible for me to finish this work.

This research was supported with funding from the Natural Sciences and Engineering Research Council of Canada (NSERC). I also gratefully acknowledge the financial support of the Department of Mechanical and Industrial Engineering and the School of Graduate Studies at Ryerson University.

Finally, I would like to thank my lab mates, Dr. David Ciampini for providing his expert opinions and Reza H. M. Jafar for sharing his experimental results and advice.

Md Abul Hasem

Table of Contents

List of Tables

List of Figures

List of Appendices

Nomenclature

The definition of symbols in alphabetical order:

Symbol	Name	Unit
a	Longer length of a loaded plate	[m]
a_p	Particle acceleration	[m/s^2]
a_r	Radial acceleration	[m/s^2]
a_{rel}	Relative particle acceleration	[m/s^2]
b	Supported width of a loaded plate	[m]
C	Constant	[non-dimensional]
c	Mean lateral crack extension	[µm]
D	Mean diameter of a single particle	[m]
D_s	Particle displacement	[m]
D_t	Particle-substrate contact period	[µs]
E	Erosion rate	[mg/g]
E	Young's modulus of elasticity	[GPa]
E_t	Transition energy of crack propagation	[J]
E_{cv}	Erosion classification value	[non-dimensional]
f_m	Maximum indentation force	[N]
F_0	Maximum load	[N]
F_1	Decreased load or relaxed load	[N]
F_c	Centrifugal force	[N]
F_d	Drag force acting on the particle	[N]
F_f	Friction force	[N]
k	Velocity exponent	[non-dimensional]
K	Generalized parameter for sphere on half-space contact	[non-dimensional]
m	Mass of abrasive	[g]
$\dot{m}$	Abrasive mass flow rate	[g/s, g/min]
m_p	Mass of a single abrasive particle	[µg]
m_f	Final mass of the container after blasting	[g]
m_i	Initial mass of the container before blasting	[g]
p	Uniform compressive surface pressure on plates	[kPa]
p_1	Initialization pressure	[kPa]
p_2	Final vacuum pressure	[kPa]
r	Radial location on the disc for stress measurement	[m]
R	Mean particle diameter	[µm]
R_a	Arithmetic average of surface roughness	[µm]
R_{Disc}	Radial distance of samples from the center of the disc	[cm]

r_o	Outer radius of the disc	[m]
r_i	Inner radius of the disc	[m]
R_q	Root mean squared surface roughness	[µm]
S	Volume flow rate capacity of the vacuum pump	[m^3/s]
t	Time duration of the blasting	[sec, min]
t	Thickness of a loaded plate	[cm]
t	Evacuation time	[sec]
V	Enclosed evacuated volume	[m^3]
V_d	Linear velocity of the samples mounted on the disc	[m/s]
V_Θ	Tangential component of velocity	[m/s]
V_n	Normal component of impact velocity	[m/s]
V_{Nozzle}	Particle velocity at impact	[m/s]
V_0	Particle initial normal velocity	[m/s]
V_p	The magnitude of particle velocity	[m/s]
V_r	Radial velocity of the particles	[m/s]
V_{rt}	Relative tangential velocity due to sample rotation	[m/s]
V_t	Tangential velocity of the particles	[m/s]
V_{Total}	Total impact velocity	[m/s]
x	The exponent for lateral crack extension	[non-dimensional]
y_m	Maximum deflection on a loaded plate	[cm]

Greek symbols

α	Global impact angle or impact angle	[deg]
α_E	Effective impact angle	[deg]
δ_m	Maximum indentation	[µm]
θ	Local impact angle	[deg]
ω	Rotational speed of the motor	[rpm, rad/s]
ρ	Mass density	[m^3/s]
ν	Poisson's ratio	[non-dimentional]
σ_m	Maximum compressive stress on a loaded plate	[Mpa]
σ_r	Radial stress	[Mpa]
σ_t	Tangential stress	[MPa]
σ_Y	Yield strength	[MPa]

Chapter 1: Introduction

1.1 Motivation

Solid particle erosion is a term used to describe the mechanical degradation of a solid material subjected to a stream of abrasive particles impacting on its surface. Traditionally, solid particle erosion has been studied in order to minimize the erosion of materials in many industrial applications. The abrasive jet micro-machining (AJM) technique has been developed utilizing the principals of solid particle erosion. AJM is a relatively new micro-fabrication technology in which a jet of high speed abrasive particles are utilized to erode the substrate creating micro-features such as micro-channels, micro-holes, etc. [1]. AJM can be used to machine glass [2-5], ceramics [6], metallic materials [7-9] and a variety of polymers [10-14].

AJM has some potential benefits over traditional chemical etching. AJM is capable of machining multi-depth, anisotropic patterns and suspended structures with relatively low cost compared to chemical etching [1, 15]. AJM has high etch rates [16] which can be directionally controlled compared to wet etching in glass which typically occurs uniformly in all directions [17]. Furthermore, AJM is more environmentally friendly, using fine aluminum oxide particles, as opposed to harmful acids used for chemical etching.

Glass is the most common material utilized in LCD or plasma flat panel displays, micro-fluidic, micro-electromechanical MEMS, and opto-electronic device fabrication due to its hardness, transparency and ease of machinability [18, 19]. Glass is a brittle material, having a maximum erosion rate at normal incidence (90° impact angle) [2-5].

Generally, two types of erosion testers can be found in the literature [20], i.e., the air blast erosion tester and the mechanically powered erosion tester. The air blast apparatus consists of a micro-blaster that combines air and abrasive into a mixture and air-abrasive jet is launched through a nozzle toward the target in a controlled manner. On the other hand, mechanically powered erosion testers utilize mechanical force to accelerate the abrasive particles towards the target. In order to reduce the feature size and extend the applicability of AJM, smaller abrasives are needed. But as the particle size decreases below 10 μm, the particle trajectories tend to be affected by the interaction of the fluid flow. A mechanical particle launching device working in a

vacuum condition seems appropriate in order to accommodate the use of smaller abrasive powders.

Most researchers have assumed that the solid particle erosion of brittle materials such as glass depends only on the component of incident particle velocity that is perpendicular to the target surface [1-5]. Only few researchers have noted the importance of the tangential velocity component of the impacting particle [21-23]. However, their investigation was more concentrated on the change in erosion mechanism due to the tangential component of velocity, rather than the magnitude of change in erosion rate due to the change in tangential velocity, which has not been studied in detail in the literature. Talia et al. [22-24] have carried out experiments to study the effect of erodent particle velocity, size, and shape on the erosion rate of glass using a rotary disc erosion tester. The rotating disc movement allowed the reduction or increase of the relative particle tangential velocity. The apparatus could also be used to separately study the effect of the particle velocity components, normal and tangential, on the erosion rates and mechanisms. They used the rotating disc to investigate erosion rates at shallow impact angles [24], but they did not study the magnitude change due to tangential velocity at a constant normal velocity. With these points in mind, the main objectives of this thesis are presented in the next section.

1.2 Thesis Objectives

The initial objective of the thesis was to study the feasibility of developing and manufacturing a mechanically powered micro-machining device to launch very small abrasive particles at a very high speed. To avoid fluid drag effects, the experiments were to be performed in a vacuum condition. However, it was found that the mechanically powered erosion tester suffered from several limitations which rendered it of little practical use in micro-machining. Therefore, the ultimate objective of the thesis was modified to instead use a revised version of the apparatus, similar to that of Talia et al. [22-24], to investigate the role of the tangential velocity component on the erosion rate of borosilicate glass impacted by aluminum oxide particles using a micro-blaster. This was accomplished by meeting the following secondary objectives:

- Design and implement a rotary disc target holder apparatus.
- Investigate erosion rate as a function of tangential component of velocity while keeping the normal component constant.
- Measure the erosion rate as a function of effective impact angle at various constant total velocities.
- Use the apparatus to determine the velocity exponent using a single blasting pressure, something that is impossible without the use of the rotating target apparatus.

These objectives will elucidate the role of tangential velocity component, often assumed negligible, on the erosion rate of borosilicate glass that is used in the AJM for micro-fluidic and MEMS devices.

Chapter 2: Literature Review

The initial objective was to design and implement a mechanically powered micro-machining apparatus. In order to design such a device, a study of similar type erosion tester designs from the literature was undertaken. It was also necessary to understand the basic principles associated with solid particle erosion, and Abrasive Jet Micro-machining (AJM). This chapter presents a detailed literature survey on these topics.

2.1 Mechanically Powered Erosion Testing Equipment

Solid particle erosion testing can be performed using two basic types of laboratory test equipment, i.e., air blast type and mechanically powered type [20]. Air blasting, in which the abrasive particles are accelerated by air pressure, is the most frequently applied technique. The process parameters are easily varied in air blast type erosion testers. However, the particle velocity may deviate strongly from that of the air making it difficult to control [25]. In mechanically powered type erosion testers, the particles are accelerated and launched with mechanical forces rather than compressed air. The three main types of mechanical erosion testers are: the centrifugal erosion tester [25-31], the rotary target with free falling abrasive particles [32], and the rotary cogwheel blaster [33].

2.1.1 The Centrifugal Erosion Tester

This form of erosion tester relies upon the centrifugal force imposed on the particles flowing through radial-positioned tubes in a rotating disc in order to accelerate the particles. Targets are stationed around the perimeter of the rotating disc. Abrasive particles are fed into the rotating disc through a vibratory feeder at the centre slot of the disc and accelerated in the radial tubes until they exit and strike the targets (Figure 2-1). The major advantage of this device is it allows simultaneous testing of multiple specimens under the same condition.

2.1.1.1 Design and Construction

The centrifugal accelerator erosion tester was first developed at the Tallinn Polytechnic Institute by Kleis in 1957 [26]. Initially, large high capacity centrifugal accelerators were designed (CAK-2). Later, reductions in size and portability were pursued (CAK-3 and CAK-4). For the sake of compactness, the belt drive was eliminated and the motor was coupled directly to the rotary disc. In addition, abrasive particles were fed into the rotating disc system by a vibratory feeder which provided a constant abrasive feed rate into the centre of the disc. It was possible to change the rotating speed and thus particle velocity with the aid of the control panel [26].

Soderberg et al. [25] slightly modified the design, naming it 'Erofuge' and derived the formula for particle velocity, particle fluxes and erosion rates. Based on the original design of Kleis et al. and modified design of Soderberg et al., the centripetal accelerator erosion test facility [27-31] that was used by the Wolfson Centre for Bulk Solids Handling Technology of the University of Greenwich consisted of a balanced disc whose velocity of rotation could be varied continuously or fixed at any given value. The disc was 0.12 m in radius and contained six radial channels made from a high quality alumina ceramic. These were 2.6 mm in internal diameter and 6.1 mm in external diameter. The target holder could hold ten targets at once. Each target holder could be angled independently to the flow in 5° increments for angles of orientation from 5°- 90° to the trajectory of the particles.

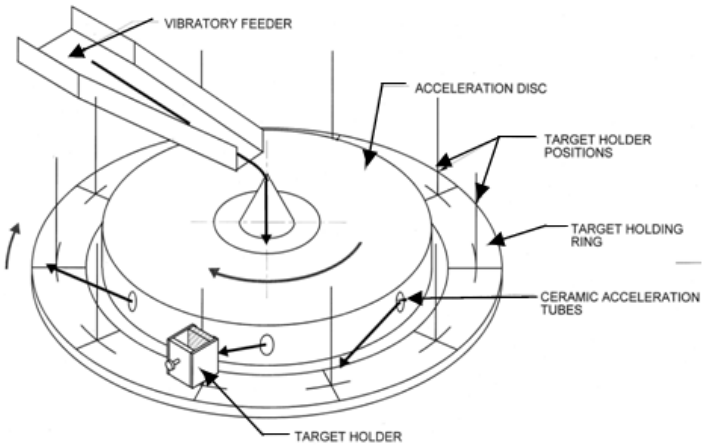

Figure 2-1: Schematic of the rotating disc accelerator erosion tester used at University of Greenwich [27].

2.1.1.2 Particle Acceleration Mechanism

Burnett et al. [27] represented a model for the particle acceleration for the centrifugal erosion tester. Based on an analysis of the particle acceleration mechanism in the centrifugal disc, the forces acting upon an individual particle within an acceleration tube are shown in Figure 2-2. The forces include the centripetal force caused by the rotation of the acceleration tube, the air drag force, the frictional force acting between the particles and the wall of the acceleration tube, and the coriolis force between the particle and the wall. Obviously, the centripetal force is the dominant contributor to particle acceleration in this type of erosion tester. The final particle velocity is controlled by the centripetal force [27]. The force equilibrium equation can be expressed as:

$$m_p a_r = F_c - F_f - F_d \tag{2-1}$$

where, m_{p} is the mass of a single abrasive particle, a_r is the radial acceleration, F_{c} is the centrifugal force, F_f is the friction force, F_d is the drag force acting on the particle. This Equation (2-1) may be used to calculate the radial velocity of the particle through the whole acceleration tube. The velocity vector of the ejected particles can be expressed as:

$$\boldsymbol{V}_{\mathbf{p}} = \boldsymbol{V}_{\mathbf{r}} + \boldsymbol{V}_{\boldsymbol{\theta}} \tag{2-2}$$

where, $\boldsymbol{V}_{\boldsymbol{\theta}}$ is the tangential component of velocity, $\boldsymbol{V}_{\boldsymbol{p}}$ is the magnitude of particle velocity, and $\boldsymbol{V}_{\boldsymbol{r}}$ the radial velocity of the particles.

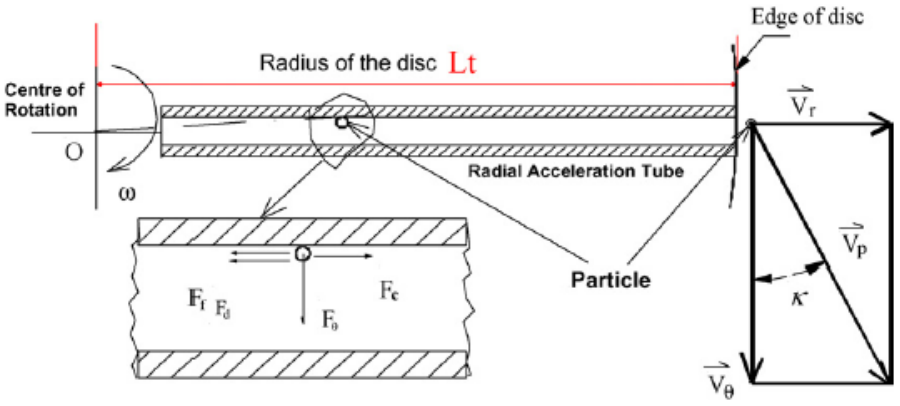

Figure 2-2: Schematic of the forces acting on a particle in the acceleration tube of a centrifugal tester [31].

2.1.1.3 Particle Dynamics

An understanding of particle dynamics is important when determining material erosive wear in any erosion tester, because particle impact conditions are primarily influenced by particle acceleration. A better understanding of particle dynamics in the testers aids in the control of erosion test conditions and therefore improves the accuracy of the measurement. Particle velocity and impact angle are important factors directly affecting erosion testing results [27]. The particle velocity and impact direction are influenced by the means of particle acceleration in an erosion test apparatus. Furthermore, the test apparatus also affects other parameters of particle dynamics such as particle rotation and particle concentration in the abrasive jet. The experimental determination of particle velocity, particle trajectory, particle dispersion, and particle rotation has shown how they influenced particle movement and therefore the particle impact conditions [28].

Deng et al. [28, 29] carried out a theoretical analysis and detailed experimental study of particle dynamics in the centrifugal erosion tester. A computational model was developed for the calculation of particle dynamic parameters. The model identified and quantified the forces acting on a particle in the acceleration tube of the tester. It was found that the greatest influence on the particle velocity was the centrifugal force acting on it because of the rotation of the disc. However, the frictional force between the particle and the wall of the acceleration tube was also found to be significant. The frictional force depends on the particle shape through its influence

on the tendency of the particle to spin. The air drag force has the smallest contribution on the particle velocity vector. The calculation result is supported by experimental results that show little effect of particle size on either particle velocity or exit angle [28].

2.1.1.3.1 Particle Shape

In the centrifugal erosion tester, the effects of uncertain particle dynamics are relatively small because the centripetal force is the major accelerating force and, for any given mass of particles, this force is unaffected by particle characteristics except for particle shape. The particle shape mainly affects the particle rotation but not the particle velocity. Simulation of particle acceleration in the centrifugal tester showed that the frictional force acting on the particles only contributed about 4% of total particle acceleration, that the centripetal force contributed about 95% of total particle acceleration, and that the air drag force contributed less than 1% [31]. In the case of different particle shapes, i.e., round or angular particles, the particle shape only influenced the tendency for the particle to either roll or slide, and therefore it changed the friction acting on the particle. Since the frictional force in the tester only contributes 4% of the particle acceleration, it will not change the particle velocity significantly. The air drag force contribution for particle acceleration in the centrifugal erosion testers is negligible.

2.1.1.3.2 Particle Velocity Distributions in the Jet

Deng et al. [28, 29] have discussed the influence of particle velocity distribution of the centrifugal erosion tester in their papers. Particle velocity distributions and exit angle were determined using three methods: (i) stroboscopic method, (ii) Ruff-Ives slotted plate velocimetry, and (iii) opto-electronic velocimetry, for a large number of particles under identical test conditions. A jet of low particle mass flux (to minimise inter-particulate collisions) was set-up for the measurement. It was found that the spherical shape particles were able to spin within the rotating disc with a consequently reduced coefficient of friction with the wall of the acceleration tube and, therefore, reach a higher radial velocity [28]. This may be compared with the behaviour of irregular shaped particles, where in certain cases spin may be precluded,

allowing only sliding with a resultant higher friction and reduced velocity [28]. The effects of inter-particle collisions within the tube and variations in the rotational speed of the acceleration disc also give rise to a velocity distribution. It is apparent that the particle velocity distribution in this type of erosion tester is quite narrow. The narrow range of the particle velocity is a major advantage of the erosion test in this type of erosion tester, compared with the gas-blast tester [20].

2.1.1.3.3 Particle Jet Dispersion

Burnett et al. [27] mentioned particle dispersion, but he failed to quantify the jet divergence for this type of erosion tester. Particle jet divergence occurs in the centrifugal accelerator type erosion tester due to the mechanism of inter-particle collision in the acceleration tubes. The particles may travel in different directions in a particle jet and therefore the particles may diverge leading to a lower impact flux at the target surface. Due to the tangential force acting between the particles and the wall, the particles tend to stay together as a group in the acceleration tubes, as the wall limits the particle scope to change direction. When the particles leave the tubes, the jet diverge only a small amount in the air because of the short distance travelled. However, in the tube the particles may still have some inter-particle collisions. These lead to particle dispersion of the particle jet. Because of the tendency of particles to group in the tube, the angle of particle dispersion for this type of erosion tester might be small [31].

Soderberg et al. [25] also showed that the particle jet may be slightly divergent, i.e., that the particles in the jet travel in different directions with a dispersion of angular trajectories and velocities. As a consequence of the mechanisms of particle acceleration in the testers, the intensity of the particle jet will be a maximum at the central axis of the acceleration tube. Therefore, the particle distribution in the jet can be defined as a function of the intensity of the particle stream in relation to the positional ordinate across the jet [31].

2.1.1.3.4 Particle Rotation

The significance of particle rotation on erosion has been recognized by many researchers, but relatively little work has been found in the literature. It is extremely difficult to measure the rotational velocity and direction of rotation for smaller particles and multiple particle impact tests. Consequently, studies have been limited to single impacts with large particles [31]. However, with high-speed photographic techniques, it is possible to estimate angular speeds of particles. In centrifugal erosion tester, inside the acceleration tubes, friction force tends to rotate the particles. This particle rotation depends on the shape of the particles and frictional force. When the particles are homogenous spheres, then the ease of rotation is greatest and consequently the particles will have a maximum rotational angular velocity. However, because of the frictional force, any particle contacting the wall must have a trend to spin and consequently may result in other particles spinning. This phenomenon is very specific for this type of erosion tester and has a big influence on the erosion rate [28].

2.1.2 Rotary Target with Free Falling Abrasive Particles

The principal idea of this erosion tester [32] was to accelerate the targets instead of accelerating the particles towards a stationary target. The targets were assembled at the periphery of a rotating disc and the particles free fall through a vibratory feeder. The significant features of this tester were:

- The system was run under vacuum condition
- The impact velocity could reach 250 m/s
- The impact angle could be varied
- The target holder could hold up to eight targets
- The mass flow rate of particle was kept very low
- There was a particle collection system after impact

The chamber was made of stainless steel with two glass windows for visual observations. The chamber was kept under vacuum condition with average pressure of 0.02 bars to minimise the aerodynamic effects. The collisions were recorded using a high-speed digital video camera.

The necessity of vacuum chamber was proven through a comparison between two results: one at a vacuum pressure and another at atmospheric pressure. It was found that at a lower impact velocity, (i.e., up to 30 m/s) there was an insignificant difference in the results. However, when the velocity was higher than 30 m/s, the breakage of the particles due to collisions with the target surface decreased at atmospheric pressure, i.e., at an impact velocity of 64 m/s, there were less than 80% of the undersized particles collected at atmospheric pressure than under vacuum conditions. When the rotating speed increased the particles were blown away before the collision because of the turbulent air stream generated from rotating disc acceleration. This result was also supported by visualization studies using the high speed video camera.

Although the apparatus could obtain accurate results for impact tests over a relatively wide range of parameter variations, it had a few disadvantages. The system was complicated to operate and much more expensive than traditional blast systems. It was also difficult to mount a load cell on the rotating targets in order to measure the impact loads. Moreover, when the impact velocity was increased, the particles tended to collide on the top part of the target, rather than the centre.

2.1.3 Rotary Cogwheel Blaster

The principal objective of this apparatus [33] was to generate a dust jet of micron and sub micron sized dust particles by impacting with a fast rotating cogwheel in vacuum condition. Compressed dust powder was fed onto the rotating cogwheel. The cogwheel then launched the powder covering a wide range of impact speeds and impact angles. The basic working principal of the cogwheel dust generator is shown in Figure 2-3. A circular 180 mm diameter and 5 mm thick aluminum disc consisting 120 small cogs rotates at a high speed. The compressed dust powder was pushed through a cylinder using a linear actuator. When the cylinder of compacted powder came in contact with the rotating cogwheel, the column of powder was broken and particles were accelerated at a tangent to the circumferential direction. The targets were mounted

at a desired angle of interest. The modulated laser illumination of the trajectory imaging system was used for determination of particle direction and velocity. The maximum rotational speed achieved was 10,000 rpm by using a simple DC motor and pressure inside the chamber was 0.02 mbar.

The complex de-agglomeration mechanism was explained using simplified assumptions. The de-agglomeration occurred in two steps. The compressed dust powders at first were broken into large agglomerates by mechanical stress and vibration. Then these agglomerates came in contact with the high speed cogwheel and burst into single particles in the dust jet.

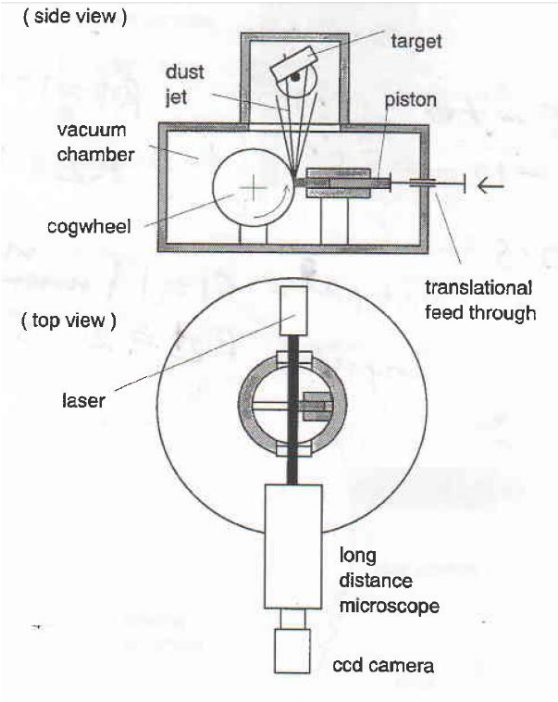

Figure 2-3: The basic experimental setup of the dust collision experiments [33].

In the particle velocity distribution, it was assumed that the maximum particle speed would be the rotation speed of the cogwheel. In fact, the observed particle velocity ranged from zero to maximum. It was found that all velocity distributions had two different maxima, one was close to the rotational speed and the other one was one quarter of the rotational speed of the

cogwheel. At low rotation speeds, the duration of one pass (contact period of cog and the powders) was long enough to allow many agglomerates to reach the plane surface of the cogs. This might be the reason that the velocity maximum close to rotation speed dominated at low speeds. The reverse situation occurred at a higher rotational speed.

At a lower rotational speed (below 3000 rpm) of the cogwheel, the de-agglomeration failed. In that situation large agglomerates were launched rather than launching single particles. It also failed if the vacuum was not sufficiently low. The rapidly rotating cogwheel generated an air stream that blew away the dust particles before they touched the cogwheel. Typically, this occurred at several tens to one hundred mbar. The particles decelerated at a very short distance and made a dust cloud instead of a dust jet. This effect was strongly dependent on how densely the powders were packed. Although it was very difficult to determine the actual particle fraction that was utilized (number of particles in the jet per number of particles coming out of the particle storage), an approximate investigation revealed that the particle utilization fraction was very low, i.e., between 2%-5%.

2.2 Solid Particle Erosion

Solid particle erosion mechanisms are classified broadly as either brittle or ductile. In brittle erosion material removal occurs due to deformation wear and fracture, while ductile erosion exhibits cutting wear. At shallower impact angles, cutting wear (ductile erosion) is favoured; while at impact angles approaching 90° deformation wear (brittle erosion) is promoted [34, 35].

2.2.1 Variables Affecting Solid Particle Erosion

Solid particle erosion is influenced by many experimental conditions. Variables affecting the erosion can be broadly broken down into three types [35]: impingement variables, particle variables, and material variables. The impingement variables are particle velocity, impact angle, and particle concentration. Particle variables include particle shape, particle density, and particle size. Material variables include all the mechanical properties of target which could be the

hardness, the toughness, the hardening behaviour, and the microstructure. Erosion rate is defined as the mass of the target material removed per unit mass of abrasive used (g) [19].

2.2.1.1 Impact Angle

Aquaro and Fontani [35] conducted studies on both ceramics (brittle materials) and metals (ductile materials) and suggested that the impact angle was the most significant indicator of the erosion mechanism. Ductile materials show the greatest wear rate at a shallow impact angle, while brittle materials wear most rapidly when the particles are incident normally to the surface [36]. Oka et al. [6, 34, 37, 38] found that the two parameters that most influenced solid particle erosion in the case of metals, ceramics and polymers were the impact angle and the hardness of the target.

Erosion rate of a target material at a certainly impact angle certainly depends on the ductility of the material if other experimental variables are kept constant. From Figure 2-4 (a) it is clear that the more ductile the material, the higher is the maximum normalized erosion and the shallower the impact angle at which the maximum occurs. For example, where the maximum normalized erosion for lead occurred at impact angle of 15º, gray cast iron had a maximum at about 40º. The plastic material (nylon 6 in Figure 2-4 (b)) showed even more ductile behaviour having maximum erosion at a 10º impact angle. The ceramic material (alumina) showed a brittle characteristic having a maximum erosion rate at normal impact.

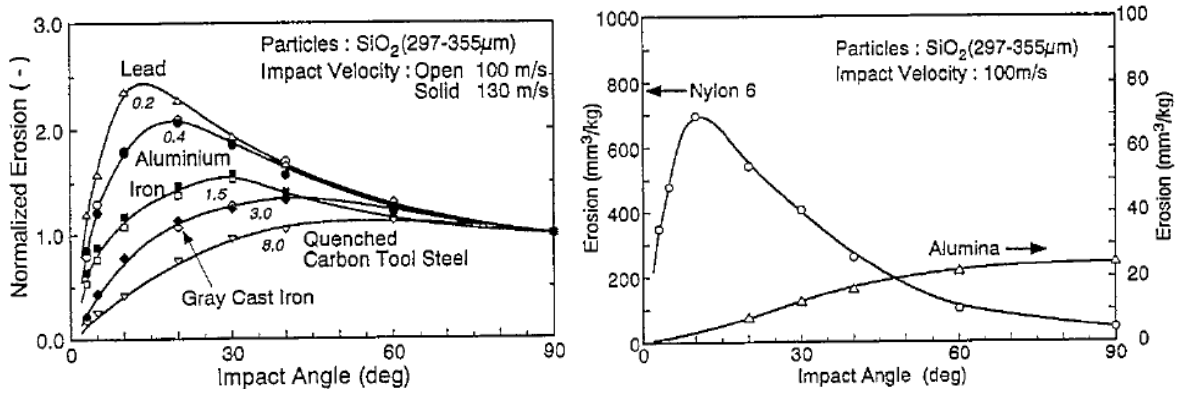

(a) (b)

Figure 2-4: (a) Normalized erosion rate for five metallic materials, (b) Erosion rate of a polymer and a ceramic material [34].

2.2.1.2 Particle Velocity

It is a well-established fact that the amount of erosion increases with increasing impact velocity. The velocity of the erodent particles is related to the erosion rate through an empirical power law relation expressed as:

$$E = C\,V^{k} \tag{2-3}$$

where, E represents the volume or mass of material eroded per mass of erodent, C is a constant, V is the normal velocity of the impacting particles and k is the experimentally determined velocity exponent. Oka et al. [34] observed that the value of k is between 2 and 3 for ductile metals, and between 3 and 5 for brittle materials. Many researchers found this velocity exponent to be in between 2-4 for glass [2, 3, 5, 39-41]. Oka et al. also found that the velocity exponent is independent of impact angle within experimental error. Hence, the velocity exponent was found to depend on the properties of the target material and the erodent particle.

Oka et al. [34] conducted a study on aluminum specimens for three different particle velocities. They have concluded that the normalized erosion rate (ratio of erosion rate to the normal impact erosion rate) dependence on impact angle was independent of impact velocity for ductile materials. Although the magnitude of the erosion rate increased (Figure 2-5(a)) due to the velocity increase from 50 m/s to 130 m/s, the normalized erosion rate remained the same (Figure 2-5(b)) for all three velocities. Oka et al. [37] also found that both impact velocity and particle size were independent of each other, i.e., the particle size did not affect the impact velocity dependence of erosion damage and the impact velocity did not affect the particle size dependence of normalized erosion damage.

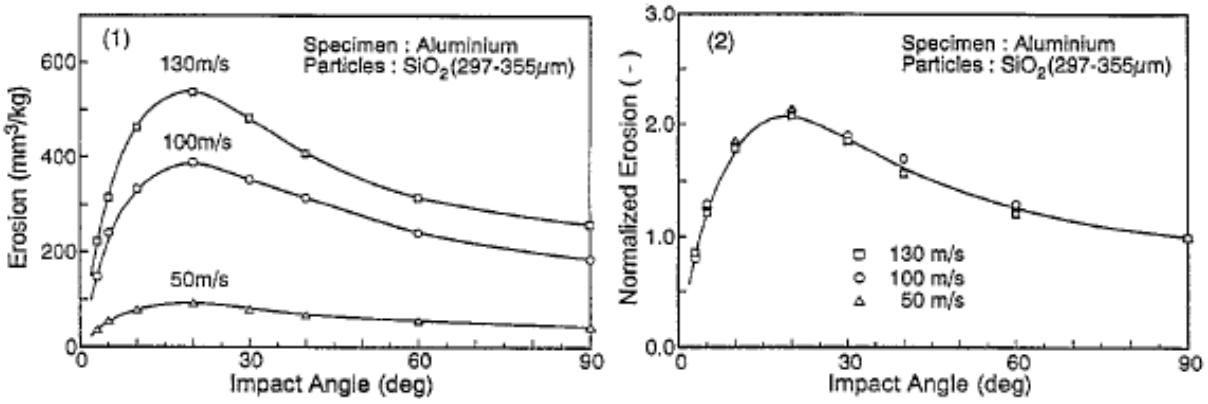

(a) (b)

Figure 2-5: The effect of particle velocity on (a) erosion rate, (b) normalized erosion rate for aluminum [34].

Oka et al. [6] also investigated the effect of impact velocity on the erosion rate for brittle materials. They found that the effects of impact velocity on impact angle dependence of normalized erosion were small with the combination of an Al_2O_3-1 specimen and a SiO_2 particle, but greater with SiC particle (Figure 2-6). One of the reasons could be that the angularity and hardness number of SiC particles was higher than that of SiO_2 particles. The behaviour of impact angle dependence became high as the impact velocity increased for the two particles.

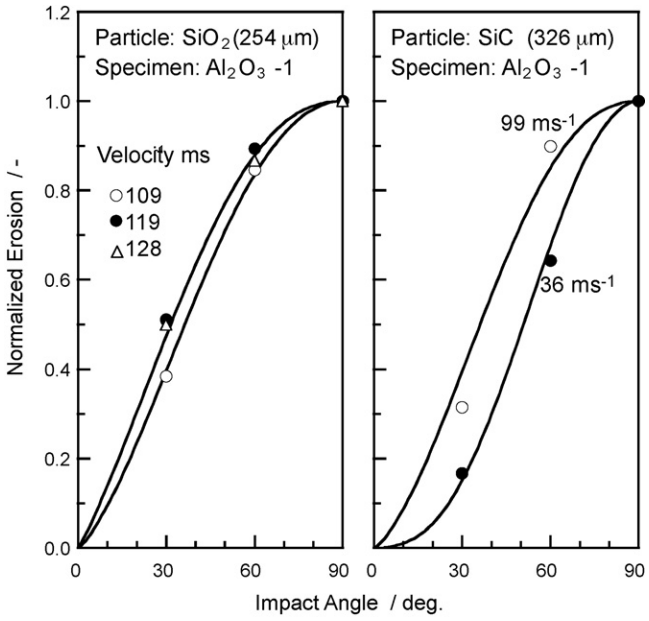

Figure 2-6: Effects of particle velocity on impact angle dependence of normalized erosion for alumina caused by silica sand and silicon carbide particles [6].

2.2.1.3 Particle Size

The increase in impact particle diameter clearly accelerates erosion damage. Increase in particle size leads to larger or deeper indentations. The larger or deeper the indentation, the greater the amount of material removed from the rim of the indentation [37]. Hutchings [36] has also observed a sharp decrease in erosion rate when the erodent particle size was reduced below a threshold value. This might be because the smaller particles do not have enough kinetic energy for erosion damage to occur. From the study it was also clear that the threshold particle size depended on the impact velocity; at a velocity of 150 m/s, no threshold effect was seen over the range of particle size investigated, but at lower velocities, there was a rapid decrease in erosion rate for small particles [36].

For ductile materials particle size has little effect on impact angle dependent normalized erosion. Impact energy is definitely increased by increasing particle size, but the relative aggressiveness of a particle appears to be nearly the same with a constant angularity independent

of particle size [37]. The ceramics (brittle materials) showed a different characteristic than metals. The effects of particle size on the impact angle dependence of normalized erosion for Al_2O_3-1 specimens and SiO_2 (194-428 μm) particles is shown in Figure 2-7. The impact angle dependence was relatively higher depending on the gradual increase in particle size [6].

Figure 2-8 shows an example of the effects of particle size on the impact velocity dependence at normal impact. The amount of erosion damage by small particles was lower than that by larger ones for the same impact velocity. The slope of the impact velocity dependence was about 2.5, and was independent of particle diameter for aluminum [37].

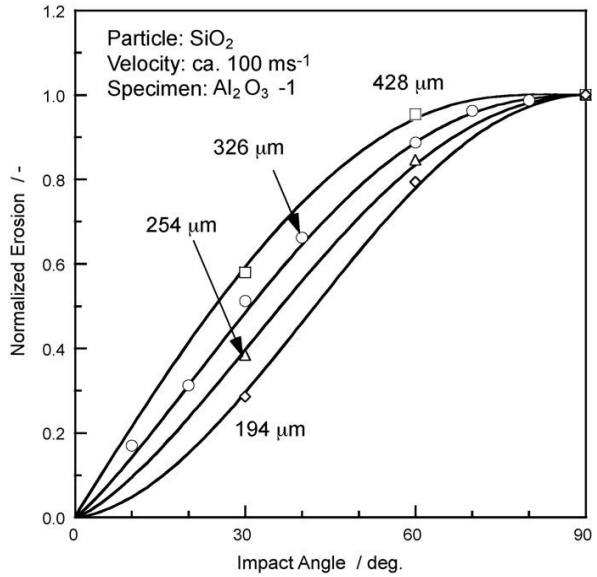

Figure 2-7: Effects of particle size on impact angle dependence of normalized erosion for alumina caused by silica sand particles [6].

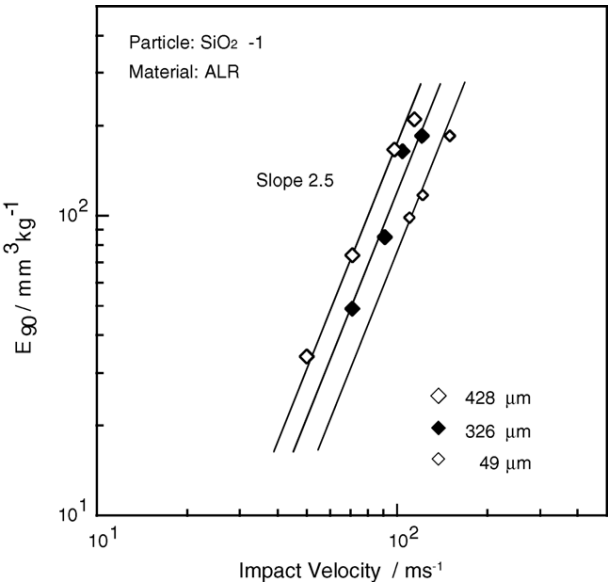

Figure 2-8: The effects of particle size on impact velocity dependence of erosion caused by the impact of silica particles [37].

2.2.1.4 Particle Shape

Hutchings [36] has investigated the effects of particle shape on the erosion of a silicate glass ceramic. Silica erodent particles were used of constant size (125-150 µm) but with angular and rounded shapes. Figure 2-9 shows the variation of erosion rate with impact velocity for the two types of silica particle at 30° impact angle. With the rounded particles, there was a sharp increase in erosion rate at velocities between 44 and 52 m/s, while with the angular particles a constant increase in erosion rate occurs with increases in velocity. Above 52 m/s, the erosion rate due to the angular silica was about 1.5 times that measured with the rounded silica, but below the transition point the rate was about 10 times [36].

Oka et al. [6] also found that angular particles caused higher erosion than round ones at shallower impact angles for brittle materials. It was found (Figure 2-10) that erosion rates caused by an angular SiC particle were greater than those caused by a round ZrO_2 particle. The impact angle dependence of normalized erosion caused by round particles of ZrO_2 was similar irrespective of the type of material, and was lower at lower impact angles, as compared with the angular particles. Surprisingly, the normalized erosion rate of the SiC materials damaged by SiC

particles was significantly lower at lower impact angles due to the reduction of cutting action by the angular particles [6].

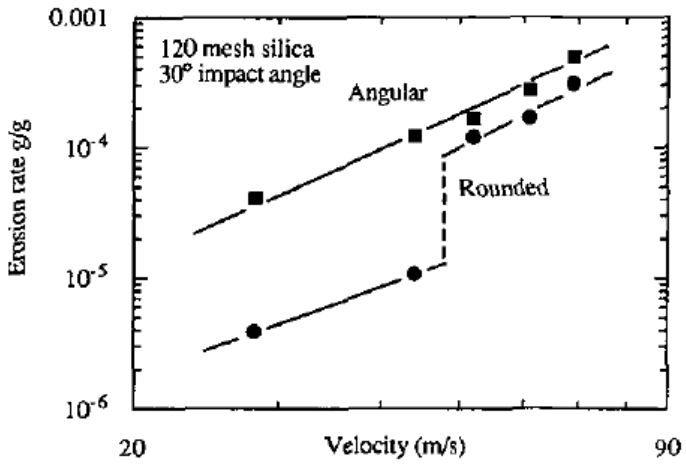

Figure 2-9: Erosion rate versus impact velocity for a silicate glass ceramic eroded by silica particles of two different shapes: angular and rounded [36].

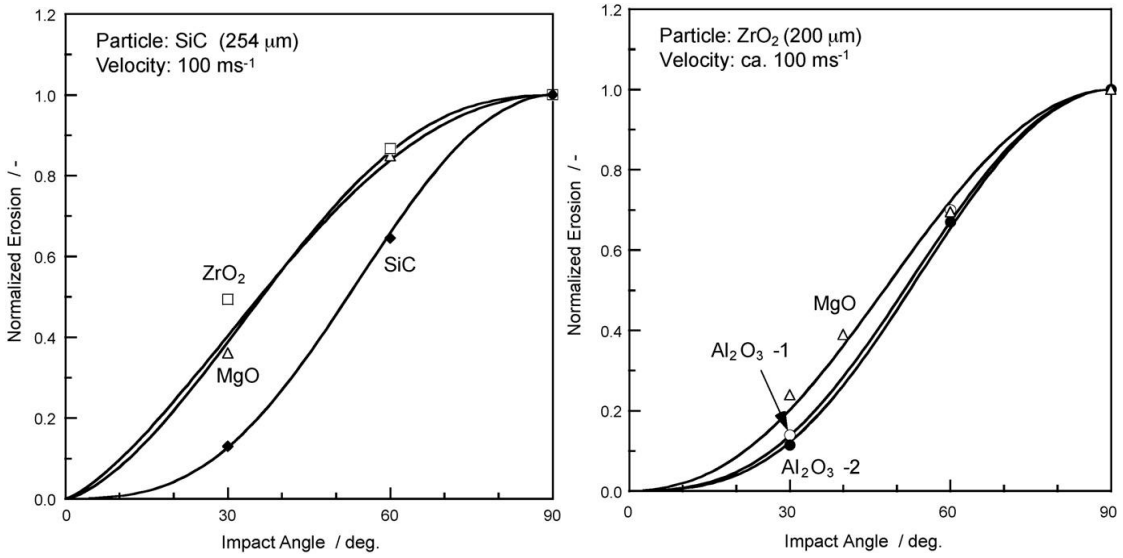

Figure 2-10: Impact angle dependence of normalized erosion rate by angular SiC and Round ZrO_2 particles in different ceramics [6].

2.2.1.5 Material Hardness

Finnie et al. [7] reported that material hardness is independent of the amount of erosion in the case of heat-treated carbon steels. However, Oka et al. [38] found from investigation of metallic materials that the dependence of erosion rate on impact angle depends strongly on the mechanical properties of the materials at the shallower impact angles. It was found that both the impact angle and maximum erosion rate value shifted with material hardness. The harder the material, the higher is the angle to reach the maximum erosion rate, and the maximum erosion rate was lower than for the softer material (Figure 2-11).

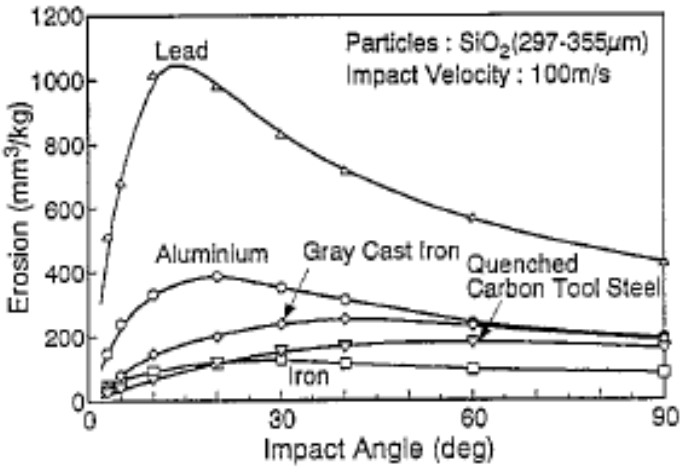

Figure 2-11: Erosion rate versus impact angle for five metallic materials [34].

It was also found that material hardness is the most dominant factor when it comes to impact angle dependence of normalized erosion. The effect of material hardness on the impact angle dependency of the normalized erosion was much higher than that of particle velocity and size [38].

2.2.1.6 Other Parameters

Solid particle erosion is a complex dynamic process with many variables influencing the erosion behaviour. In addition to the above discussed variables, some other significant properties are worth mentioning. For brittle materials, fracture toughness was probably a dominant factor which strongly influenced erosion behaviour. For ceramics the hardness might be a secondary factor as compared to fracture toughness [38]. Moreover, erosion rates of ceramic materials probably depend on material supply processes, binders and sintering [6].

When a particle strikes a surface it may remain essentially undamaged, or it may deform by plastic flow or fracture. Hard angular particles striking relatively soft targets will tend to produce plastic indentation, which in a ceramic may be accompanied by fracture (median and lateral cracking) and lead to erosion. However, if the particles are insufficiently strong and tough, they may distort or even fragment on impact. The damage they cause will then depend on the response of the target material, but it is unlikely to result in the localized indentation necessary to form lateral fractures, and the erosion rate will be lower. This particle fragmentation effect has been observed and reported by Hutchings [36] for a range of five different glass bonded sintered alumina. Their erosion rates and mechanisms were studied with silica, alumina and silicon carbide erodent particles. The erosion rates increased with erodent particle hardness in the sequence silica < alumina < silicon carbide, and the relative erosion resistance of the five alumina was found to vary significantly between the different erodent. This effect was large enough to change the ranking of the materials for different erodent materials. Generally, lower values of velocity exponent as well as lower absolute erosion rates are seen for the erosion of ceramics by softer particles such as alumina rather than silicon carbide, and this can also be explained by the increased crushing and fragmentation of the particles on impact [36].

The impact angle dependence of normalized erosion rate is not only influenced by material hardness, but also other mechanical properties of the target material. Oka et al. [38] has mentioned a distinct parameter called load relaxation ratio which was defined as:

$$\text{Load Relaxation Ratio} = \frac{(F_0 - F_1)}{F_0} \tag{2-4}$$

where, F_0 is the maximum load and F_1 is the decreased load or relaxed load. The load increased with testing time during the indentation process and then gradually decreased as the load was relaxed, after the completion of the indentation. The behavior of the load relaxation ratio depended upon the type of material and the extent of plastic deformation or brittleness [38]. It is generally considered that load relaxation increases with an increase in the ratio of load to the size of the indentation. This indicates the possibility of a constant load relaxation ratio against the increased indentation ratio. However, for all of the materials used in this study the load relaxation ratio decreased with the indentation ratio [38]. The decrease in the ratio is associated somehow with work-hardening or an unknown mechanical property of the material.

2.2.2 Modes of Solid Particle Erosion

2.2.2.1 Ductile Mode

Generally metallic and plastic materials behave in a ductile erosive manner, showing maximum erosion at shallower impact angle of about 20º. The material removal is the sum of material lost (shown in Figure 2-12) due to repeated plastic deformation and cutting (the particle strike the body scratching out some material from the surface). During the impact, when the material elastic limit is exceeded, plastic deformation occurs. The surface layer is destroyed and portions of it are removed.

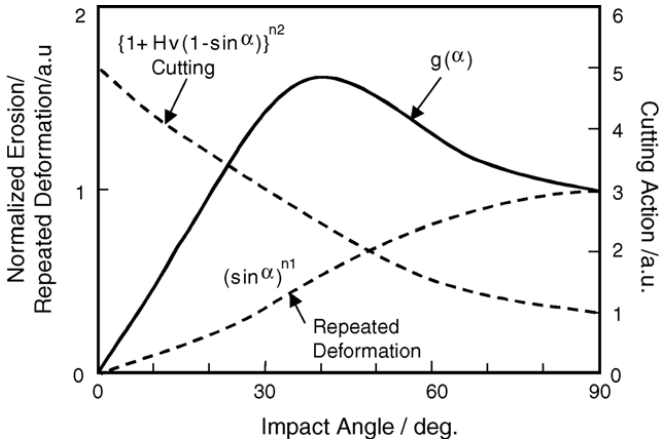

Figure 2-12: Ductile erosion arising from repeated plastic deformation and cutting action [37].

The particle velocity can be resolved in two components, one normal to the body surface (normal component) and another parallel (tangential component) to it. The normal component is responsible of the particle penetration in the body while the tangential one gives the particle scratching and cutting action [35]. Figure 2-13 given below shows a sample crater shape and material removal mechanism of a ductile material.

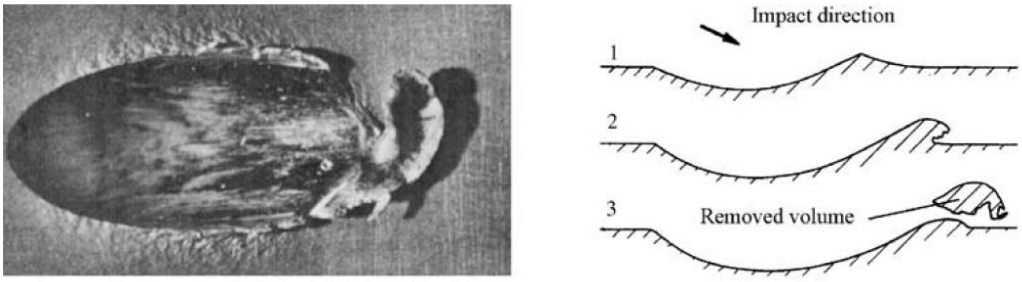

Figure 2-13: Crater shape and material removal mechanism for a ductile material [35].

For erosion in ductile materials there can be an initial weight increase issue under certain conditions due to particle deposition or embedment. For example, the experimental work on aluminum specimens conducted by Neilson & Gilchrist [42] using 210 μm alumina particles at normal impact, revealed an initial weight gain due to particle embedment. They also found similar behaviour when eroding copper, brass and mild steel.

2.2.2.2 Brittle Mode

When a brittle material is impacted by a hard sharp particle, the contact area is plastically deformed due to the high compressive and shear stresses and a radial crack is formed. After the impact, the plastic deformation leads to large tensile stresses that result in lateral cracks causing the material removal [5]. Figure 2-14(a) shows a very simplified representation of such an event, but in reality more than one lateral and redial/median crack could be present (Figure 2-14 (b)).

Verspui et al. [43] assumed that chips will be removed only when the lateral cracks reach the surface in their model. They assumed every lateral crack causes chipping, which in fact is an

overestimation of reality. Their assumption of every lateral crack causes chipping also accounts for the slight increase in surface roughness, since more material is removed from the surface. They found that in the standard case, the calculated crack length and the depth were of the same order of magnitude.

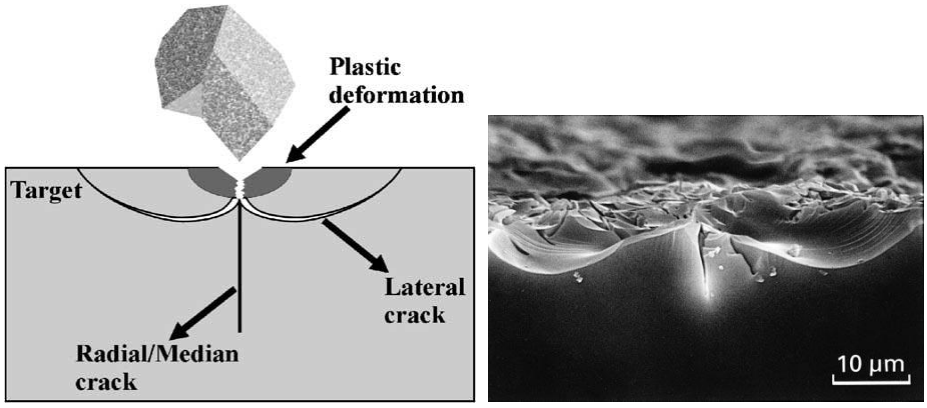

(a) (b)

Figure 2-14: (a) Simplified schematic diagram of crack formation [5], (b) SEM photograph of a lateral crack in an eroded borosilicate glass sample [4].

Oka et al. [34] found that the more brittle the material was, the more time it took to reach steady state. The impact angle dependence normalized erosion (erosion rate/erosion rate at normal impact) graph (Figure 2-15) showed that the harder alumina (Al_2O_3-1) curve shifted to a higher position, and that of the softer magnesia (MgO) shifted to a lower position.

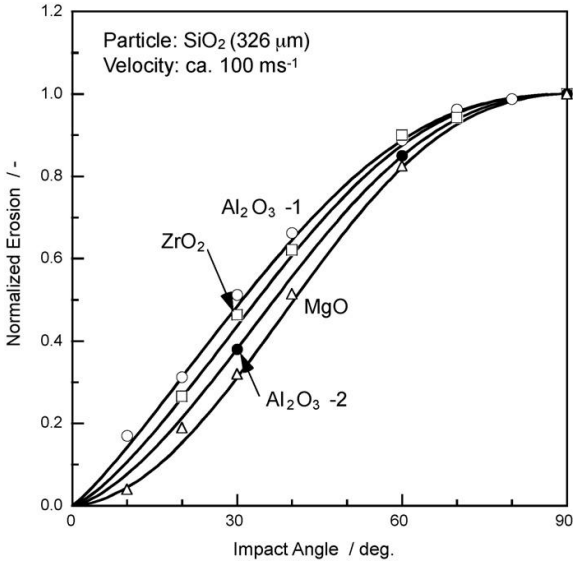

Figure 2-15: Normalized erosion for alumina (Al_2O_3-1 and Al_2O_3-2), zirconia (ZrO_2) and magnesia (MgO) materials caused by silica sand particles [14].

2.3 Transitions between Modes of Erosion

The wear mechanism changes significantly if the impact velocity of the particles and impact angle of the erosion is changed. Such a transition often represents a change in the nature of fracture and rate of material removal [36]. Transitions in wear mechanism can also be associated with a change in particle size, shape and hardness [37, 38]. Many researchers [2-5, 19, 43] mentioned that the erosion rate also depends on kinetic energy of the particles.

2.3.1 Ductile to Brittle Transition Due to Temperature Changes

Under two different impact conditions, it is possible for the same material to erode in both a ductile and brittle manner. The erosion mechanisms depends not only on the erodent kinetic energy [5] i.e., particle size and velocity, but also on the target material mechanical properties at different temperatures.

In the ductile to brittle transition temperature region, the ductile fracture process is independent of temperature, and it is determined by the composition, microstructure, and

mechanical properties of materials. The temperature dependence of the ductile to brittle fracture transition is determined by the temperature dependence of initiating a brittle fracture ahead of the fibrous crack tip. It is commonly accepted that the initiation of the brittle fracture is determined by the criterion of the local fracture stress being exceeded by the normal tensile stress ahead of the tip of the defect. The temperature dependence of the ductile to brittle fracture transition is a result of increasing the size of the active zone for initiating brittle cleavage fracture with decreasing temperatures [44].

Temperature is a significant factor in ductile to brittle transition. At very low temperature ductile materials could behave like brittle materials. Getu et al. [12-14] have also found a brittle behaviour of ductile polymers by developing a cryogenic abrasive jet micro-machining (CAJM) process. The process cooled the polymers below its glass transition, thereby allowing for material removal via brittle erosion mechanisms.

Rodriguez et al. [8] also noted a transition from ductile to brittle erosion as material hardness increased. They blasted AISI H13 and 4140 steel with silica sand erodent ranging from 150-425 μm. A shift in the angle of maximum erosion was noted as the hardness increased in the case of H13 steel. They found three distinct zones in the erosion curves: between 10-20°, the higher the hardness, the lower the erosion; between 20-30°, erosion remained constant with increasing hardness; and at angles of 60° and higher, higher erosion was observed with increasing material hardness signifying brittle erosion. The latter was said to be caused by the development of adiabatic shear bands which create sites for the nucleation and propagation of cracks, an indication of brittle erosion.

2.3.2 Brittle to Ductile Transition Due to Changes in Particle Kinetic Energy

Brittle erosion does not always occur for ceramics and other brittle materials. When particle speed and size are decreased, eventually the particles are unable to initiate cracking and will only plastically deform the target. This change in erosion mode is called the ductile to brittle transition, first described by Sheldon and Finnie [45]. They demonstrated that a brittle material glass eroded in a ductile manner using 9 μm SiC particles at 152 m/s. They explained this phenomenon with a fracture mechanics approach that assumed cracking occurs only when a flaw

is present in the glass. The plastically deformed area below the impact site becomes very small when the size and speed of the particles is reduced. The chance of encountering or completely covering a flaw and initiating a crack is thus decreased [45].

Hutchings [36] also showed through experimental studies that reducing the size of silicon carbide erodent particles from 125 μm to 9 μm, caused the angle of maximum erosion for soda-lime glass, moulded graphite and magnesia to shift from close to 90° to a much lower angle. This implies the behaviour changed from brittle to ductile.

Wensink and Elwenspoek [5] also conducted detailed research on brittle to ductile transition based on the incident kinetic energy of the erodent for three materials: soda-lime glass, Pyrex and silicon. They confirmed a ductile behavior of nominally brittle materials both by the rippled appearance of the eroded surface and by the variation of erosion rate with impact angle. The chance of lateral crack formation becomes smaller as the kinetic energy is decreased. They defined a new term called 'erosion classification value' E_{cv}, which is the ratio of erosion rate at 45° and 90° impact angle. Brittle erosion has an E_{cv} of about 0.45, whereas the E_{cv} of ductile erosion is larger than 1. When kinetic energy is reduced, the E_{cv} of brittle targets eventually increased to a ductile value of greater than 1. The transition does not occur suddenly, but extends over at least one decade of kinetic energy.

2.3.3 Transition Mechanisms

For indentation fracture in erosion theoretically two types are important: (1) Hertzian fracture and (2) lateral fracture [36].

2.3.3.1 Hertzian Fracture

Hertzian cracking is associated with the contact of rounded particles and preceded only by purely elastic deformation. In Hertzian fracture arising from the normal direction impact of an elastic particle; the critical velocity to cause fracture is a function of particle density, fracture toughness of target material, modulus of elasticity and the particle diameter. Alternatively, the critical spherical diameter to cause fracture depends on the velocity and other three parameters

mentioned above. The Hertzian fracture map (Figure 2-16) shown below explains how the erosion mechanism changes by variation of particle velocity and particle size [36].

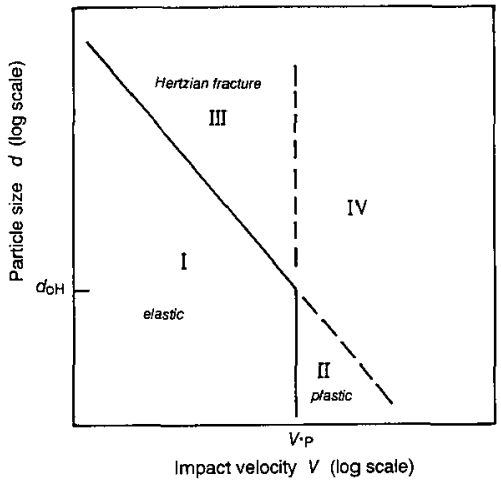

Figure 2-16: Hertzian fracture mechanism map showing the transition caused by particle size and velocity [36].

Region I (Figure 2-16) is for small particles and low impact velocities in which the deformation is purely elastic and the erosion rate is very low. Basically this region is associated with fatigue processes which may eventually lead to crack propagation under cyclic loading. Region II is for small particles (with diameter less than a threshold value) and an increase in impact velocity. At this stage plastic deformation of the target occurs and material will be eroded by ductile processes, although it is also possible that fatigue cracking may also occur in this region. Region III is for particles larger than the threshold size and at higher velocity, where erosion occurs by the formation and intersection of Hertzian cone cracks. Further increases in velocity within region III can bring the system into region IV, in which conditions for both Hertzian fracture and plastic flow are simultaneously satisfied. Under these circumstances erosion will probably involve both plastic flow and fracture [36].

2.3.3.2 Lateral Fracture

Lateral fracture is caused by the contact of hard angular particles and preceded by local plastic indentation and deformation of the surface. The critical load on a sharp rigid indenter to

cause lateral fracture in a brittle material is a function of the modulus of elasticity, fracture toughness, and hardness of the material. Using the relation it is possible to derive the threshold conditions with respect to critical particle size and velocity of the particle for the occurrence of lateral cracking [36].

Figure 2-17 shows the regions of particle size and normal impact velocity in which particles of rounded and angular shape will cause lateral fracture. The difference in slopes of the two lines leads to their intersection at threshold conditions of velocity and particle size. In region I, plastic indentation of the target by impinging particles will not be accompanied by lateral fracture. In this region, material will be removed by plastic processes, and the response of the material can be expected to be effectively ductile. It is still possible that lateral cracking may occur when conditions are near the boundary of the region, by fatigue processes driven by the cyclic stresses caused by multiple impacts. Region II represents intermediate conditions, in which angular particles will cause lateral fracture but more rounded ones will not. Region III results from the intersection of the two lines representing the critical conditions for lateral fracture by angular and rounded particles, and within this state the conditions for fracture by rounded particles are satisfied while those for angular particles are not. In region IV, the conditions for lateral fracture by all particles, whatever their shape, are satisfied, and the material will be eroded by brittle processes [36].

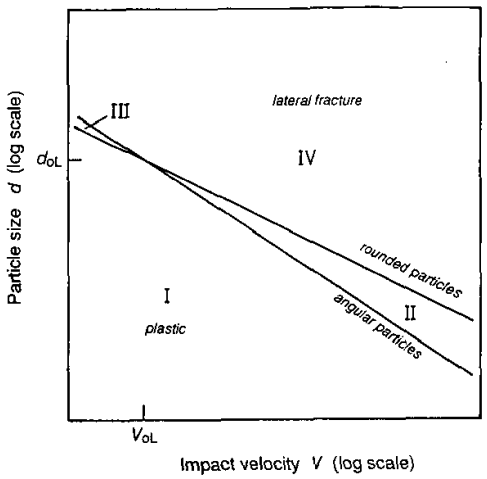

Figure 2-17: Lateral Fracture map showing the regions of particle size and normal impact velocity [36].

2.4 Effect of Velocity Components

Erodent particle velocity is divided into two components: normal velocity and tangential velocity, when blasted at an oblique impact angle. Both velocity components have significant role at erosion process (ductile and brittle materials), thus the study of particle velocity components has importance.

2.4.1 Effect of Velocity Components on Ductile Materials

At a normal impact, the normal velocity is the only component. But as the impact angle becomes shallower the tangential component of velocity dominates the erosion mechanism. This is a well-known fact that the solid particle erosion of ductile materials is dominated by the tangential component of velocity giving maximum erosion at shallower impact angles [37, 38]. Ballout et al. observed that the ripples form on pure aluminum (impacted by sharp alumina and spherical glass beads) parallel to the tangential velocity [22]. The ripple formation on the surface of pure aluminum impacted by solid particles has been seen to be most prominent near a 30º impact angle, and no ripples were formed when the target material was impacted at a normal angle. Instead, a formation of random bumps was observed [22].

2.4.2 Effect of Velocity Components on Brittle Materials

The contribution of normal velocity component to the erosion of brittle materials is a very well-established fact. The erosion rate maximizes at normal impact for brittle materials [6, 23]. Many researchers have mentioned that normal velocity is the only factor causing erosion in brittle material through crack initiation and propagation [2, 4, 5, 46-48]. In the surface evolution modeling of glass impacted by sharp particles, researchers [1, 3, 19] have commonly assumed that only the kinetic energy transfer normal to the target surface contributes to the development of the eroded surface. Some other researchers have also found that, for brittle materials, tangential effects are negligible [2, 46-48]. A rotating target holder is capable of varying tangential components of velocity while keeping the normal component constant which would

help to investigate the relative effect of tangential component. Such an investigation is one of the objectives of the present thesis.

The study by Srinivasan & Scattergood [21] was one of the few that investigated the tangential velocity effect on brittle materials. They conducted a study on lateral cracks in glass produced by alundum particle (200 μm) impacts, and studied single impact events in terms of lateral crack extensions and their probability of chipping at two angles of impact of 20 and 90°. Comparisons between these two sets of data were made at the same normal component of velocity to better assess the tangential component effects. Figure 2-18 also shows a velocity threshold below which the chipping probability is zero. The velocity threshold for 90° impact, obtained by extrapolation of the straight line to zero chipping probability, was approximately 12 m/s. This means experiments at velocities close to 12 m/s for the 90° impact condition confirmed that chip removal was negligible even though noticeable lateral cracking occurred. Although the limited data for 20° impact made it difficult to obtain a threshold value, it appears to be close to zero velocity as seen from Figure 2-18. The normal velocity threshold is lower at 20º than at 90º, i.e., at a constant normal component of velocity, the 20º impact was more effective at material removal. Assuming that erosion rates will scale with chipping probability, this suggests that oblique incidence is more erosive than normal incidence at the same normal velocity component for this study of single impacts [21].

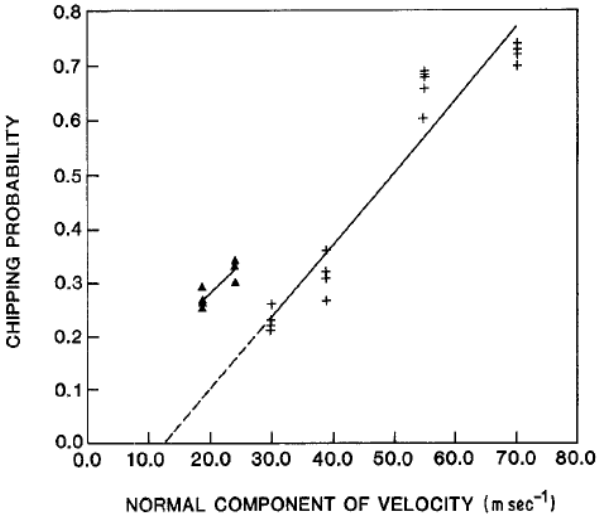

Figure 2-18: Chipping probability dependence on normal velocity component for glass impacted by alundum (200μm) particles: (+) normal impact, (▲) oblique impact at 20° [21].

Srinivasan & Scattergood [21] found that the normal impact data follows a power-law relationship between normal velocity component and the mean lateral crack extension:

$$c \propto V_n^x \tag{2-5}$$

where V_n is the normal component of impact velocity, c is the mean lateral crack extension and the exponent x is found to be 0.770. A logarithmic plot of lateral crack extension versus the chipping probability at a constant normal component of particle velocity (Figure 2-19) shows increased chipping probability for the 20º impact condition at the same value of lateral crack extension. Increased chipping and lateral crack extensions in the 20° impact situation has been explained in terms of linear elastic fracture mechanics, as opposed to the plastic deformation mechanism. Assuming the depth of lateral crack formation depends only on the normal velocity, the same power law when applied to oblique incidence with its normal component of velocity yields a crack extension value which is about 30 to 39% smaller than the experimentally observed value. This suggests that greater extensions could be due to the tangential velocity component, which is quite significant in case of 20° impacts [21].

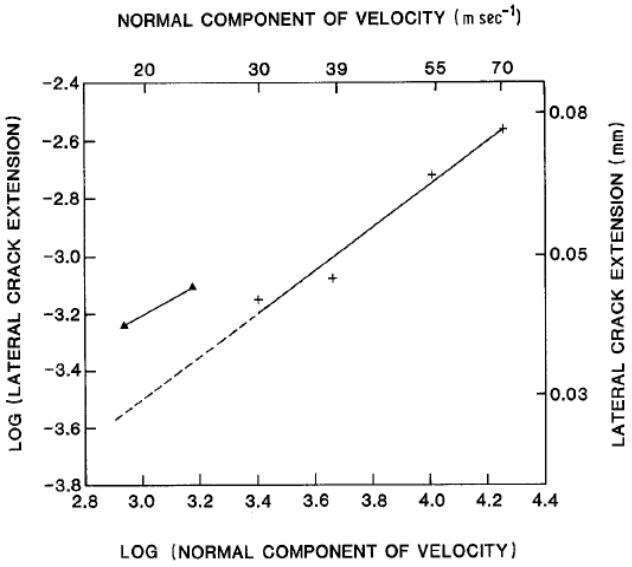

Figure 2-19: Logarithmic plot showing velocity dependence of lateral crack extension for glass impacted by alundum (200μm) particles: (+) normal impact, (▲) oblique impact at 20° [21].

Ballout et al. [23] have also conducted a study on S-glass impacted by alundum and spherical glass beads. They found that for impact angles up to 30°, a crack occurred in the forward direction of the tangential velocity (one direction). Above 30° impact angles, lateral crack occurred in various directions. They have also observed a bilinear behaviour when erosion rate versus normal velocity was plotted in a logarithmic scale (this is discussed more in Section 5.2 in Chapter 5). The difference between the two stages might be attributed to the mechanism of lateral crack propagation. In the first stage, the lateral crack propagates in the downstream direction of the impact beam (i.e., in the direction of the tangential velocity) thus causing concentrated damage. However, in the second stage, the tangential impact forces are weaker and the normal forces of impact are stronger, therefore, the lateral cracks are diffused around the impact site, and are relatively less concentrated, thus causing a less effective erosion process.

Ballout et al. [23] also showed the importance of the tangential velocity of the particle by testing the S-glass samples on a rotating disc. A full detail of this technique is discussed in Chapter 4 and Chapter 5. They showed a comparison plot (Figure 2-20) on a logarithmic scale to show the effect of tangential velocity. It was shown that the logarithmic erosion rate for the specimen with the eliminated particle tangential velocity followed a linear path, whereas with the presence of tangential velocity (static test) it was bilinear. Furthermore, for angles of impact larger than 30º, the erosion rates were almost the same as in stage II for the normal static test. However, as the impact angle decreased below 30°, the erosion rates become smaller than they were in stage I for the static test. This shows that, even though the measured erosion rate values in stage II were larger than those of stage I, the erosion process was relatively more efficient in stage I. This also indicates that the bilinear behavior of the logarithmic erosion rate is related to the importance of the tangential impact velocity at low impact angles.

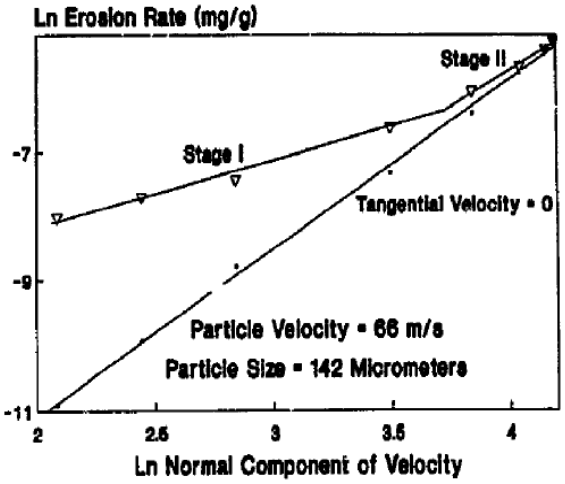

Figure 2-20: Comparison plots of the logarithmic erosion rate vs. normal velocity with an eliminated tangential velocity [23].

2.5 Dimensional Analysis in AJM

Regardless of the material removal mechanism, the material removal is usually expressed as a measured erosion rate, i.e., the ratio of the removed mass of the target material to the mass of the particles impacting the target. Erosion rate is often normalized by dividing it by its value for a normal impact (at $\alpha = 90°$). These are most commonly used non-dimensional parameters in AJM. In Equation 2-3, the constant (C) and velocity exponent (k) are dimensionless parameters. Due to the complexity of the associated phenomena, attempts at using generalized dimensionless groups to describe solid particle erosion over a wide variety of conditions have generally been unsuccessful. However, for single impact studies, Papini and Spelt used dimensional analysis to express the erosion rate in terms of a number of generally applicable dimensionless parameters characterizing the particle size, shape and process parameters [49, 50]. Papini and co-workers [51-54] also used dimensional analysis to generalize the effects of particle flux and other process parameters on the extent of interference between incoming and rebounding particles during erosion testing.

In surface evolution modeling, the particle mass flux, velocity distributions, the partial derivatives of the profile depth, time, coordinates are normalized by their values at the center of channel or hole [1, 55] to create dimensionless equations. Burzynski et al. [56] also conducted

dimensional analysis to express the particle velocity distribution within the jet. The particle mass flow rate, nozzle size, particle size, and blasting pressure all affect the number of particles in the nozzle have proposed a new dimensionless parameter, the mean number of particles across the nozzle diametrical cross section [56]. The non-dimensional distributions are useful for prediction of surface topography using analytical/numerical models and computational models [53-56].

2.6 Summary

Initially, mechanically powered erosion testers available in the literature were surveyed in order to learn from the previous designs, and to study their advantages and drawbacks for a novel mechanically powered erosion tester design and construction. A basic literature survey of solid particle erosion and abrasive jet micro-machining process was also performed. Process parameters, i.e., impact angle, impact velocity, particles size, particle shape, substrate hardness etc., affecting solid particle erosion were also studied from the available literature. The different mechanism of erosion for different type of materials (ductile and brittle) was reviewed. For the erosion of brittle materials, most of the research in the literature has mentioned the significance of normal velocity component. Although some researchers have realized the importance of tangential velocity, they did not actually measure the magnitude of erosion rate change due to tangential velocity change. Srinivasan and Scattergood [21] performed a study on chipping probability and lateral crack extension by single particle impact. They concluded that chipping probability and lateral crack extension was higher for higher tangential velocity at a constant normal velocity for single impact event. Talia et al. [23, 24] have only mentioned that erosion process was more effective when the tangential velocity was present. But none of the above researches conducted a quantitative measure on the change in erosion rate due to tangential velocity for an erosion system typical of that used in abrasive jet micro-machining. The aim of this thesis is to fill in those gaps in the literature by investigating change in erosion rate on borosilicate glass due to tangential velocity using granular alumina abrasive particles.

Chapter 3: Design of Mechanically Powered Erosion Tester

Initially, it was planned to design and construct an apparatus to launch very small abrasive particles at a very high speed, based on the rotary cogwheel blaster discussed in Section 2.1.3. In this chapter, the necessity of and purpose of implementing this type of an erosion tester, and its design constraints, components and limitations will be discussed.

3.1 Background

Currently, the smallest feature size possible using AJM is in the 50 μm range [57]. In order to reduce this minimum feature size and extend the applicability of AJM, a new particle acceleration mechanism must be developed in order to accommodate for the use of smaller abrasive powders. This is because as the particle size decreases below 10 μm, the particle trajectories tend to be affected by the interaction of the fluid flow with the target material. Since smaller particles have a low mass, those particles require a relatively high velocity in order to have sufficient kinetic energy to allow for brittle erosion damage on borosilicate glass. Also, in order to achieve a higher particle mass at a comparatively smaller volume, denser particles such as tungsten carbide and steel were preferred as media. Thus, the particle material, size, and launching velocity were critical parameters in the design process.

Since there is a minimum kinetic energy requirement in order for particles to damage the substrate in a brittle manner, machining with a practically achievable velocity could only be performed if a threshold for particle size for a brittle erosion mechanism was exceeded. A brittle to ductile transition map was constructed for different media-target systems as part of the initial research. There is a point where ductile and brittle regimes meet. This point is the start of ductile-brittle transition [2]. The design curve constructed below (shown in Figure 3-1) can be used as a guide to choose the size of particle at which the erosion would be brittle with a specified velocity. The graph showed a logarithmic relationship among particle velocity (m/s) and particle size (μm). The particle velocity in Figure 3-1, is a function of transition energy, particle type, and size, is given as [2]:

$$V = \sqrt{\frac{2E_t}{\frac{4}{3}\pi\rho(\frac{D}{2})^3}} \tag{3-1}$$

where, V = particle velocity (m/s), E_t = transition energy of crack propagation on the substrate (J). The minimum kinetic energy of a powder particle at which cracking still occurs, ρ = density of the particle material (kg/m^3), D = mean diameter of a single particle (m). The transition energy for crack propagation for substrate materials were obtained from Ref. [5].

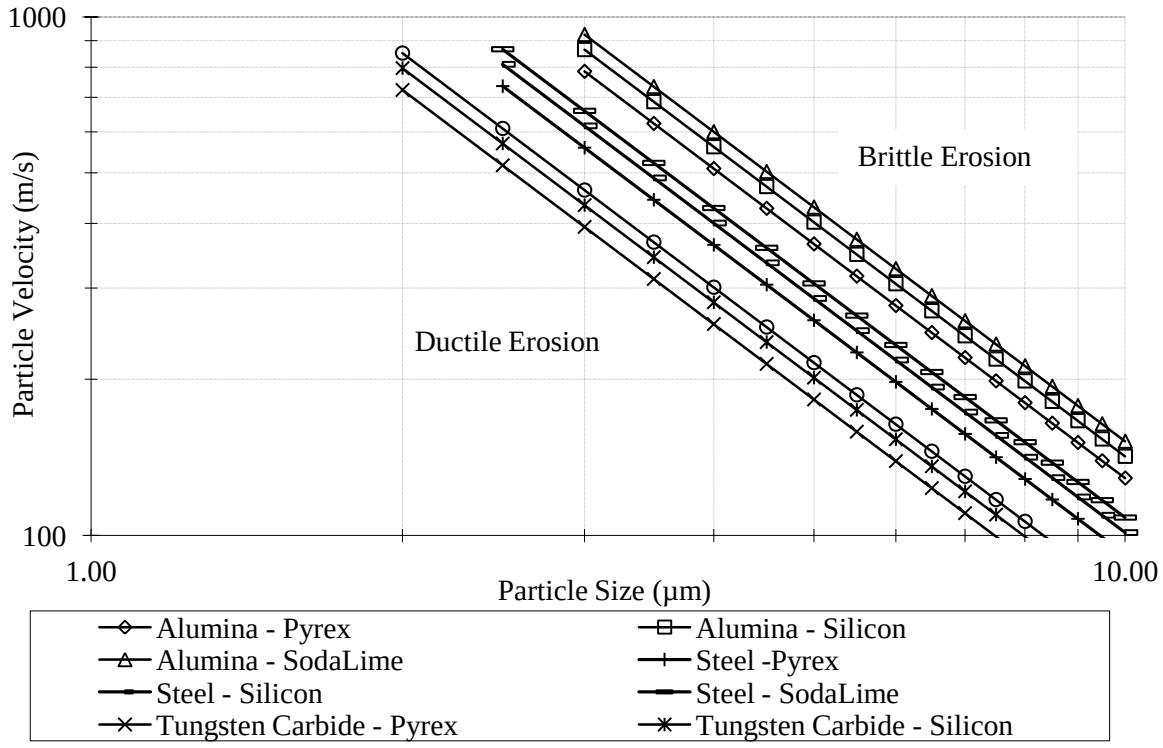

Figure 3-1: Logarithmic plot for particle velocity vs. particle size showing brittle to ductile transition graph for nine different systems [5].

The transition map was plotted for nine different systems, i.e., three different brittle target materials (pyrex, silicon, and sodalime glass), and three different abrasives (alumina, steel and

tungsten carbide). The region above the line corresponds to brittle erosion (the desired condition to allow for relatively rapid erosion) and that below the line the erosion is ductile. Figure 3-1 indicates that for all nine media-target systems, if the particle size is less than 10 μm, there is a minimum velocity requirement for a specific sized particle in order to cause brittle erosion; e.g., for the tungsten carbide particle-pyrex target system, brittle erosion using 5 μm tungsten carbide requires at least approximately 180 m/s particle velocity. For smaller particles,the velocity requirement for brittle erosion increased sharply.

Once the maximum velocity achievable by the particle launching device is found, it is thus possible to find the minimum particle size for a specific type of particle from Figure 3-1. For exampe, if the machine can launch the particles at 200 m/s on a silicon substrate, then tungsten carbide particles down to 5 μm can be used for brittle erosion on silicon; whereas the corresponding values are 6.5 and 8 μm for steel and alumina (aluminum oxide) particles, respectilvely. As the density of the particle increases (tungsten carbide> steel> alumina) the particle size can be reduced; meaning smaller size particles can be used at a given velocity.

3.2 Design

3.2.1 The Enclosure

After a series of prototypes (discussed in more detail in Appendix A), the final design of the rotary wheel blaster was manufactured. The rectangular enclosure was made out of six polycarbonate plates of 1.27 cm thickness, having the dimensions shown in Figure 3-2. Polycarbonate was a suitable enclosure material because it is transparent, light weight, impact resistant and relatively cheap. A polycarbonate door on the top allowed for access to the components in the chamber. For safety, an aluminum 6061-T6 alloy box housed the high speed rotating disc and shaft. The aluminum alloy box was mounted on the base of the chamber. A simplified representation of the design is shown in Figure 3-3.

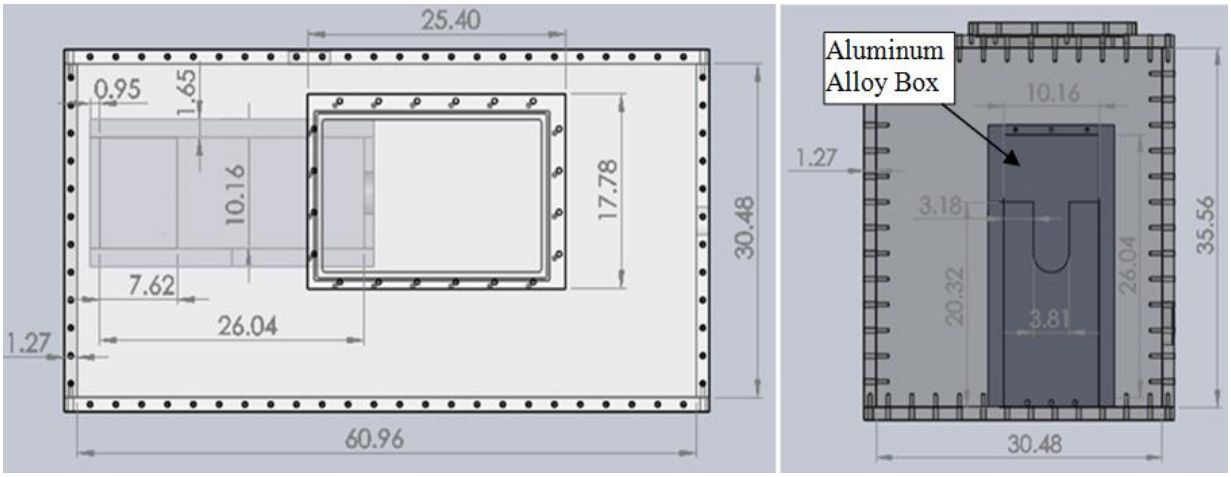

Figure 3-2: Top view and side view of the polycarbonate enclosure and aluminum box (all the dimensions are shown in cm).

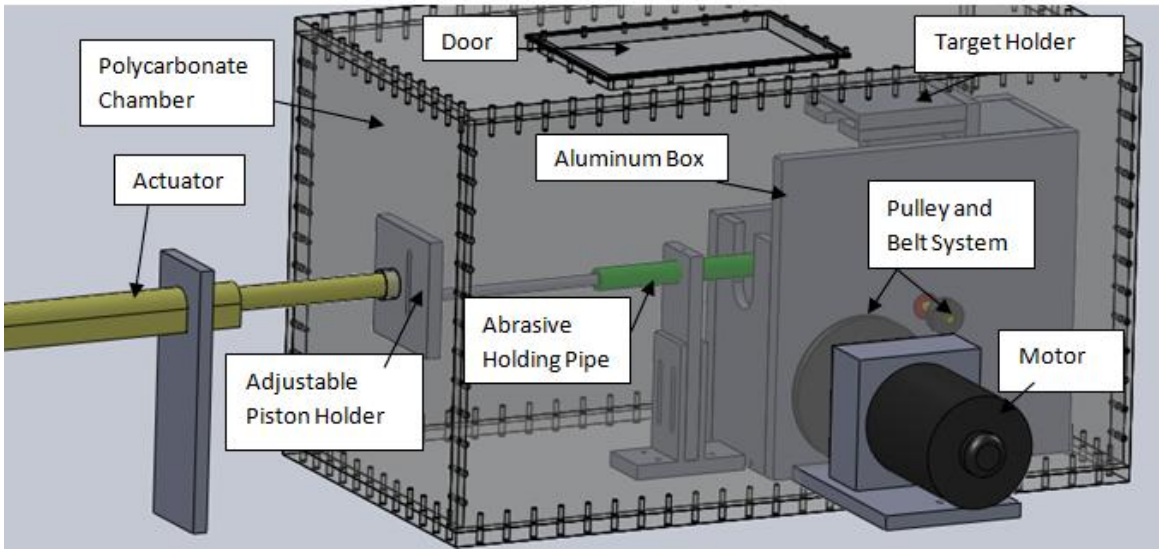

Figure 3-3: CAD design of the chamber showing major components.

3.2.2 The Rotary Device

An AC/DC 1 horsepower motor (model 2M191, Dayton Motor Co., Dayton, TX, USA) with maximum speed of 10,000 rpm was used. The motor was selected due to its versatility and power. It was kept outside the chamber to minimise dust contamination and overheating. A speed

controller (model 4X796, Electric Motor Warehouse, Burton, MI, USA) compatible with this type of motor which used 115 V AC from the wall power outlet was selected. The motor was used to rotate a disc coupled to a 12.7 cm long shaft. A pulley belt drive was used to increase the speed from the motor end to the shaft and disc. The pulleys were made of nylon (2L V-belts, Torque Transmission, Fairport Harbor, OH, USA) with an aluminum alloy hub. The smaller pulley dimensions were 3.8 cm outer diameter (OD), a 3.6 cm pitch diameter, and 0.8 cm bore. The larger pulley dimensions were 12.7 cm OD, 12.5 cm pitch diameter, and 1.3 cm bore. The belt pulley system could thus increase the motor speed by about 3.5 times neglecting all losses. The belt used was 48.5 cm long Truflex V-belt (model 2L190, Gates Co. Denver, CO, USA). The belt and pulley system and motor configuration are shown in Figure 3-4.

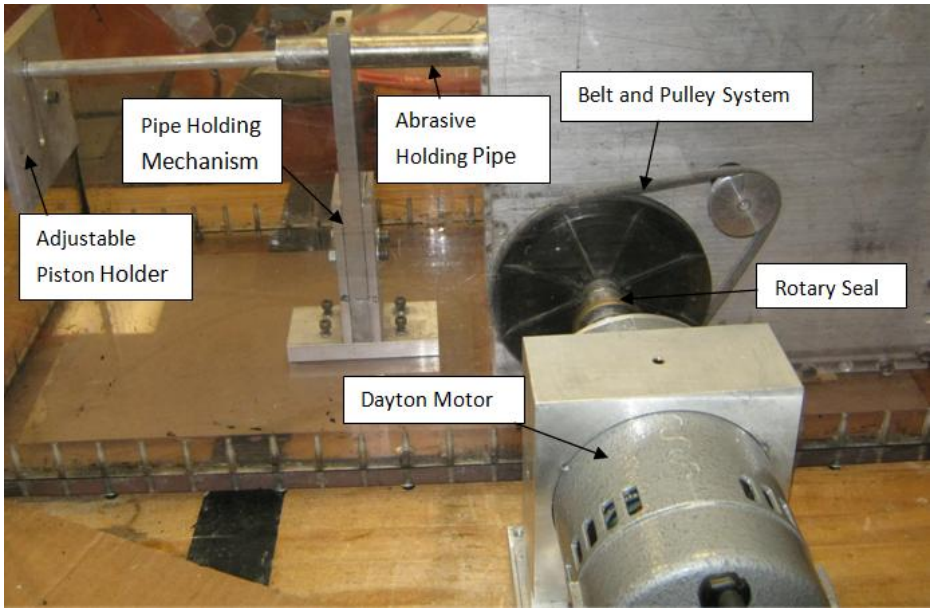

Figure 3-4: Motor side view of the mechanism showing belt and pulley system and abrasive feeding mechanism.

The disc was made of rigid high density polyethylene (HDPE) due to its wear resistance properties and light weight in order to reduce the load on the motor (HDPE is almost eight times less dense than carbon steel). The HDPE disc size was 19 cm diameter and 0.32 cm thickness

with a weight of 97.8 grams. The disc had four cogs, each separated by 90° separation distance. A stress calculation due to centripetal forces on the rotating disc is presented in Appendix B. The circular disc was attached to the rotating shaft which was made of carbon steel. The steel shaft was supported by two oil sealed high speed bearings (part # CR8x14x4HMS1R, SKF, Goteborg, Sweden) at both ends of the aluminum housing box. The rotational movement of the disc was transferred using a keyway and the axial movement was restricted using two flanges from both sides (Figure 3-5). The flanges were made of rigid HDPE and were also fixed to the shaft using four set screws at a 90° separation distance. The main shaft, disc and flanges rotated as a single unit when the motor was turned on.

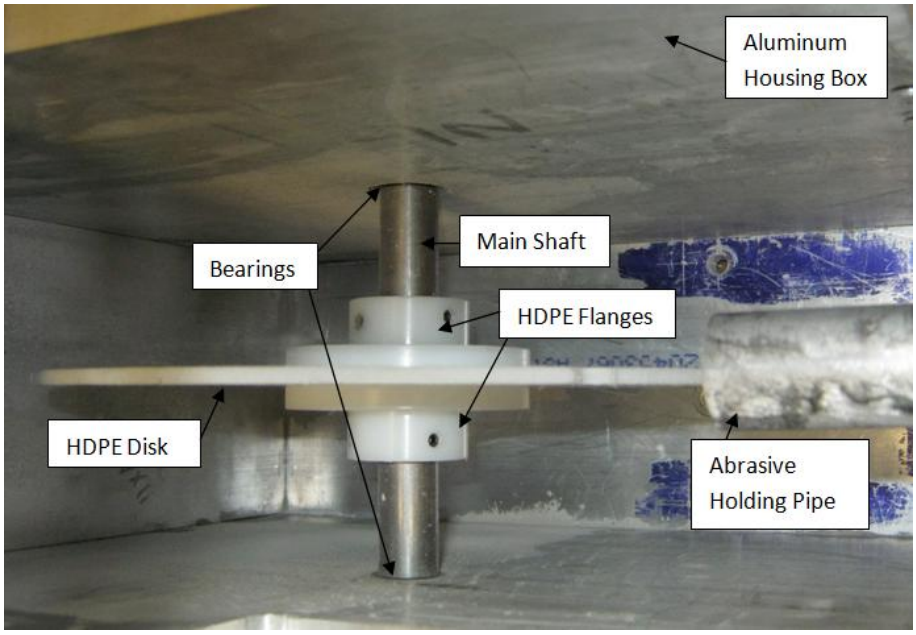

Figure 3-5: Components inside aluminum housing box.

3.2.3 Abrasive Feeding Mechanism

A linear actuator (model FA-150-S-12-12, Firgelli Automations Inc., Ferndale, WA, USA) that was capable of 30.5 cm stroke, 750 N full load, and required 12 V DC input voltage, was used to power the abrasive feeding mechanism. The actuator was powered by adjustable DC power supply (model HY3030E, Sinometer Instruments, Shenzhen, China) which could vary the

voltage from 0-12 V. The actuator speed could be changed by simply varying the voltage in the adjustable power supply. The actuator was kept outside the enclosure to reduce dust contamination and minimise the enclosure space. The actuator arm entered the enclosure through o-ring seal housing and was attached to the adjustable piston holder (Figures 3-3 and 3-4). The adjustable piston holder allowed changes in the vertical and horizontal position of the piston. The actuator and piston assembly worked as a single unit to move a 1.25 cm long polyoxymethylene (Delrin) piston inside the abrasive holding pipe to feed the abrasive in the rotating disc.

The planned media for erosion testing was tungsten carbide because of its very high density. The plan was to eventually use 5 μm tungsten carbide powders. However, initial proof-of-concept tests were conducted with 10 μm alumina particles since they were readily available and cheap. The abrasive powder with piston mechanism only worked with compacted abrasive sticks in which the abrasive moved as a single unit. When the abrasive was loose it tended to jam the piston inside the pipe because the fine abrasive powder got stuck in the very small gap between the piston and the pipe. The powder caused enormous friction with the outer surface of the piston and inner surface of the pipe. Dry lubrication was applied in the inner surface of the pipe and piston but it was not effective in solving the problem. The alumina powder was compacted using a cold compaction process using a mounting press machine (SIMPLIMET II, Buehler Ltd., Lake Bluff, IL, USA) with a 2.5 cm diameter and 10.2 cm long die. Alumina (10 μm) is a very fine powder which has a low effective starting density that increases during compaction. Compacted powder reduced the friction along the tube and created a pile of particles to be hit and launched by the cogs on the rotating disc (Figure 3-6 (a)).

Because of these problems with jamming, a new type of powder feeding mechanism was designed. This new type of powder feeding mechanism consisted of two tubes (Figure 3-7). The smaller tube holding the powder could move through the larger tube. The rotational movement was restricted by a groove on the side of the smaller tube and screw holes on the side of the larger tube. There was also a very narrow slot (0.16 cm wide) in the smaller tube for powder feeding. The smaller tube was pushed out of the larger tube by actuating the piston, resulting in the loose abrasive falling through the narrow slot. To collect the powder and project it towards the rotating disc, a small funnel was placed under the tube (Figure 3-6(b)). The jamming and compaction problem was solved by using this mechanism since the loose powder could not go

anywhere else but to feed through the bottom slot of the smaller tube into the funnel. The funnel elevation could be changed to change the particle launching trajectory.

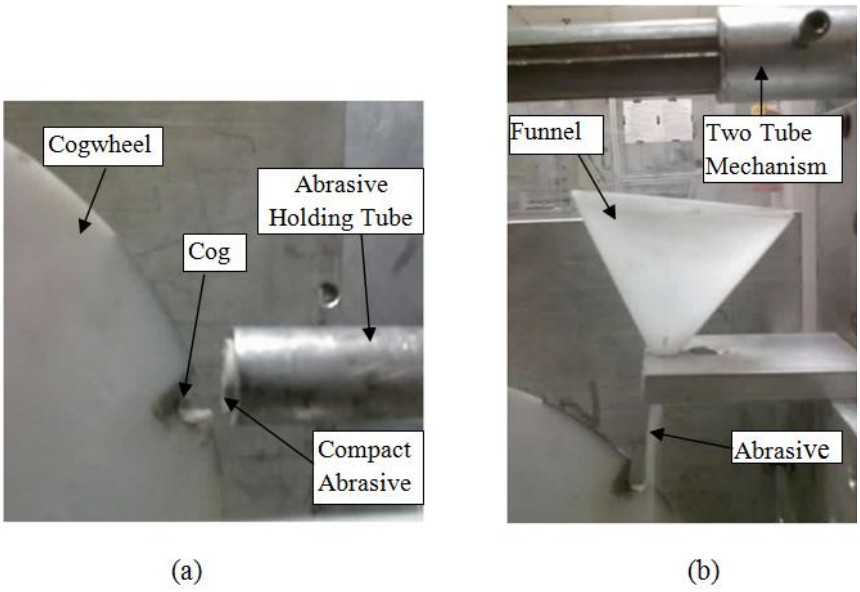

Figure 3-6: Two types of abrasive feeding mechanisms (a) scratching of compact abrasive, (b) launching free falling abrasive with new two tube abrasive feeding mechanism.

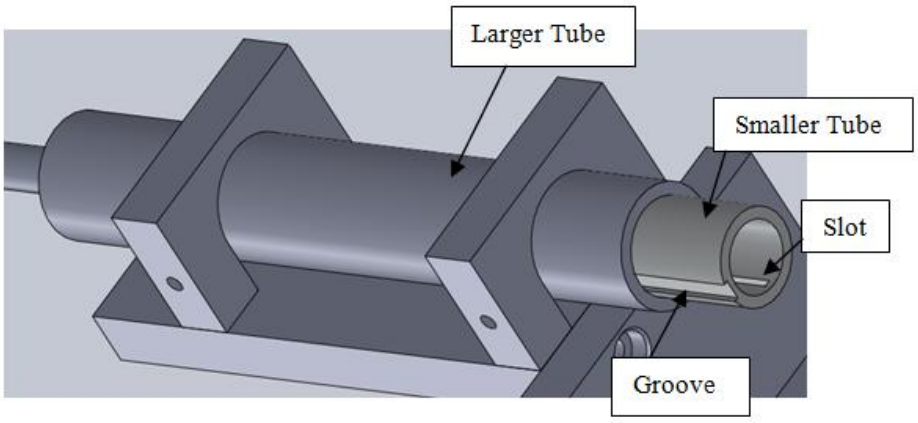

Figure 3-7: New powder feeding mechanism with two tubes. Abrasives drop down from the narrow slot when the smaller tube is pushed out.

3.2.4 Evacuating the Enclosure

The vacuum environment was created inside the chamber using a vacuum pressure pump (CPS-8B, model 180-1, US Vacuum Pumps LLC, Canton, TX, USA) attached to the chamber. It had oil-less diaphragm compressor and degassing rate of 8 CFM. The theoretical maximum vacuum attainable with that device was 101.31 kPa pressure i.e., 99.99% vacuum. The vacuum chamber was designed with a vacuum gauge to indicate the pressure inside the chamber. There was also a pressure relief valve to bring the chamber quickly to atmospheric pressure after every use. Stress and deflection calculations were conducted on the chamber walls, and are presented in Appendix C. The calculation showed a large deflection (1 cm) on the longest walls i.e., motor and pump side walls. Therefore, hard fibre bars of dimension 5 x 5 cm^2 were used as struts for reinforcement, and to restrict the deflection of the walls due to outside air pressure. Figure 3-8 shows an image of the assembled rotating disc erosion tester.

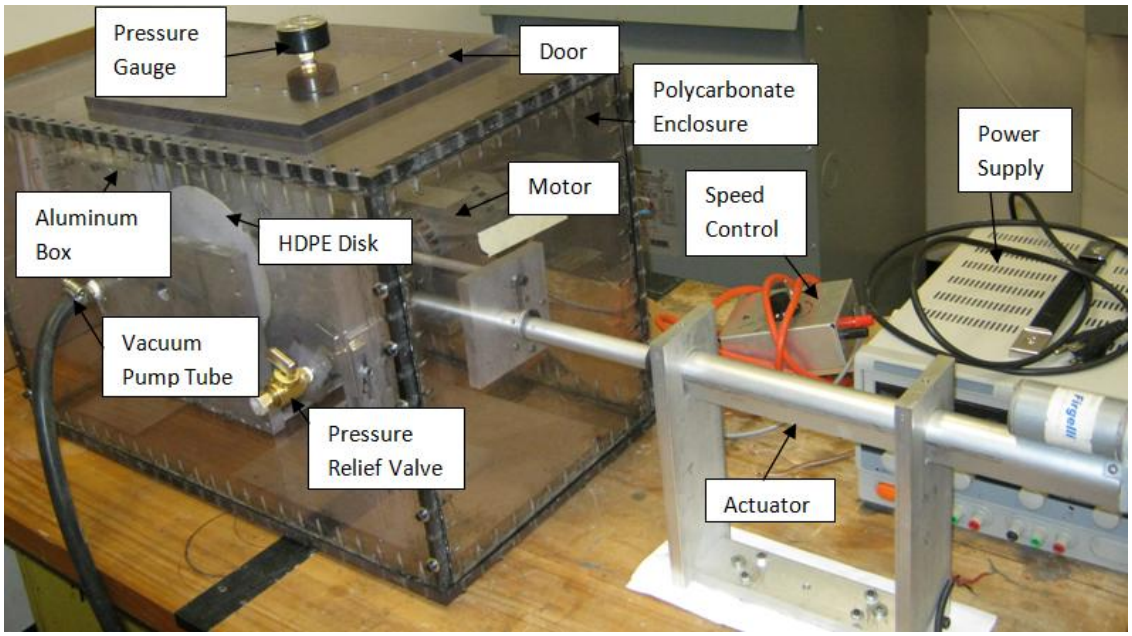

Figure 3-8: Assembled rotating disc erosion tester.

Sealing of the vacuum chamber against outside pressure was accomplished using 0.16 cm thick ultra-strength adhesive-backed oil-resistant buna-N rubber. The screws were placed at a 2.54 cm separation distance to create enough compression with the rubber sealing. The most critical points to seal in the chamber were the rotary shaft going into the chamber from motor and the linear feed-through from the actuator. Initially the rotary sealing was designed using a spring-loaded seal made of graphite PTFE. However, this type of spring loaded seal created large load on the motor which caused the motor to run slowly. Later a double sealed steel ball bearing was used as a rotary sealing. The linear feed-through was sealed through a series of buna-N o-ring seals housed in a steel chuck. Door sealing was accomplished by buna-N/ EPDM o-ring cords (dimension of 0.24 cm fractional width, 0.26 cm actual width). A glad (groove) design with a width of 0.28 cm and a depth of 0.20 cm was used to seal the door.

It should be noted that only the final design which was manufactured has been presented here in the main body of the thesis. Several earlier system designs were performed and are presented in Appendix A.

3.3 Limitations of the Mechanically Powered Erosion Tester

The mechanically powered erosion tester ultimately did not serve its purpose. An ultra-high (99.99%) vacuum was required but even after sealing the chamber only about 78 kPa vacuum (77%) was achieved. The main leakage was found to be from the rotary shaft inlet from the motor side. There was less leakage with the spring loaded PTFE seals but this caused a larger torque which affected the motor speed. A possible solution might have been to use a magnetic rotary seal for the shaft, but this was not tested due to its expense. There was also leakage from the linear actuator feedthrough. A professionally built vacuum chamber is recommended for this ultra-high vacuum requirement, although such chambers are very expensive.

Experiments with the compacted particles were conducted with the original powder feeding mechanism in which the rotating disc scraped the compacted particles and launched them towards the target. A large amount of agglomerated powder was found on the glass target rather than single particle impacts. Initially it was thought that the agglomeration might be because of static electricity, but discharging the glass sample through grounding did not

eliminate the problem. The use of a small vibrator on top of the glass sample to shake off the agglomerated powders may have been a solution.

Some experiments were also conducted with the redesigned powder feeding mechanism (Figure 3.6(b) and 3.7) under the achievable vacuum. Although the problems with the powder feeding were solved, experiments with double sided tape placed surrounding the rotating disc revealed that the free falling particles were launched on a wide variety of trajectories, rather than a single one towards the target. The air surrounding the surface of the rotating disc tended to blow the particles out of the way before they touched the cogs on the wheel. Moreover, the presence of air also reduced the velocity of the particles that were launched very quickly due to drag forces. This free falling particle feeding mechanism is probably better suited to the centrifugal erosion tester discussed in Section 2.1.1 [27-31], where the particles are fed into the centre of the disc. There were limitations on the motor speed as well. The belt and pulley system was designed to achieve a maximum of 30,000 rpm. However, the belt tension created a significant torque which caused the motor to draw much more current from AC power supply. The used speed controller was a semiconductor controlled rectifier (SCR) type, which chops a portion of the sine wave coming in from the plug, in order to change the speed. For better control, a pulse width modulation (PWM) type motor controller is recommended. Also due to the fact that the system was not perfectly balanced, there was a huge noise and vibration at a higher rpm of the motor. However, given the further expense associated with achieving the required vacuum in the chamber, no further effort on the design of a mechanically powered erosion tester was expended. Instead, the designed mechanism driving the rotation of the pulley/belt system was adapted to be used in the rotating target holder apparatus discussed in Section 4.2.

Chapter 4: Experiments

In this chapter, a traditional micro-blaster and a designed rotating disc apparatus similar to that used by Talia et al. [22-24] were used to investigate the effect of the change in tangential component of velocity on the resulting erosion rate of borosilicate glass. The design and implementation of the rotary disc apparatus was discussed in Section 4.2; and the advantages, use, and erosion rate calculation method using this device were given in Section 4.3.

4.1 Experimental Apparatus

The erodent particles were accelerated using an AccuFlo (Comco Inc., Burbank, CA, USA) micro-blaster into which a mixing device was installed in order to prevent particle agglomeration, and ensure a repeatable mass flux [60] (Figure 4-1). Experiments were performed using 25 μm to 150 μm nominal diameter granular aluminum oxide particles (Comco Inc.). Both 0.76 mm (part # MB1520-30), and 1.5 mm inner diameter (part # MB1520-60) nozzles (Comco Inc.) were used in the experiments.

The 1.5 mm inner diameter nozzle was used for the experiments to determine the tangential velocity dependence of erosion rate, at a constant standoff distance (the distance from nozzle tip to target surface) of 1 cm where the maximum velocity occurs [59]. This nozzle was also used for these experiments because it was well characterized experimentally, i.e., measured impact velocities determined by shadowgraphy were available in Ref. [59], for alumina particles of different sizes. The velocity estimation procedure is discussed in Section 4.4.

The 0.76 mm inner diameter nozzle was used at a 2 cm standoff distance for the experiments to determine the impact angle dependence on the erosion rate. These experiments required very shallow impact angles and very high rotating disc speeds. At these shallower impact angles, the 1 cm standoff distance, utilized with the 1.5 mm inner diameter nozzle, is too close to the rotary disc, causing interference with the mounting bolts on the rotary disc. Thus, the 0.76 mm inner diameter nozzle was utilized for these types of experiments.

The particle velocity was varied by changing the driving air pressure of the AccuFlo blaster. The resulting velocities and all other experimental parameters are given in Sections 5.1-

5.3. The nozzle was attached to a rotating mount and a manual stage which allowed variation of the impact angle, and elevation change while holding the nozzle to target standoff distance (shown in Figure 4-2) constant. 1.75 mm thick borosilicate glass (BOROFLOAT 33, Schott North America Inc., Elmsford, NY, USA) were cut into 1 cm x 2.5 cm samples and used as the target material.

A few modifications were made to the rotating disc particle accelerator design of Chapter 3 in order to utilize it as a rotary disc target holder. The belt and pulley system was meant to multiply the motor speed by 3.5 times at the disc end, but the torque was also multiplied by the same ratio of speed increase on the motor end. As explained in Section 3.3, the resisting torque due to the tension in the belt and imbalance in the system assembly was found to be too large for the motor, this was not well-managed by the controller. To avoid these problems, and for simplicity since the required max rotating speed was relatively small compared to that required for the rotating cogwheel setup, the belt and pulley system was eliminated and a direct drive was employed using a shaft coupling to merge the motor shaft with the main shaft. The motor speed was measured using a digital and noncontact tachometer (model 11765T58, Monarch Instruments, Amherst, NH, USA) with an accuracy of 0.01% and range 5-99,999 rpm.

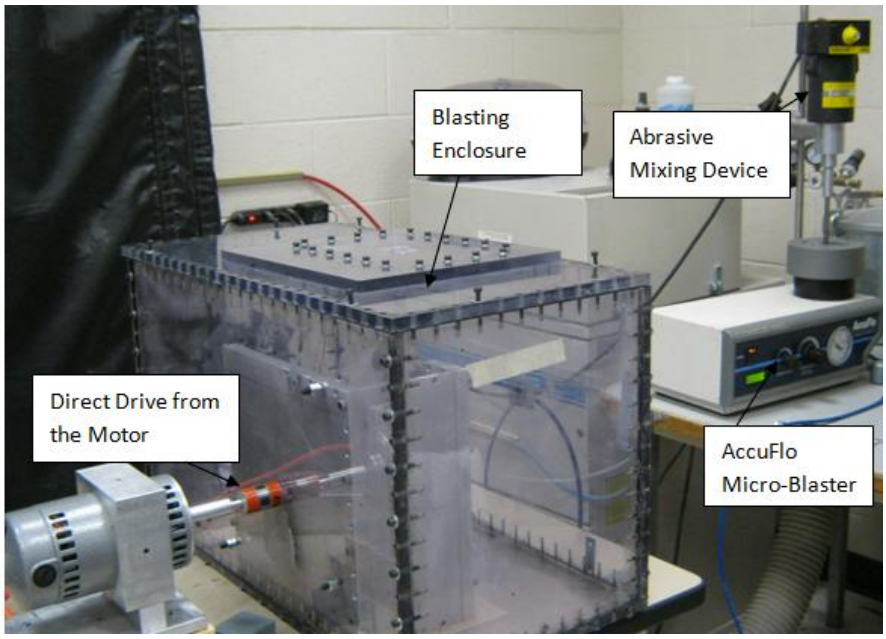

Figure 4-1: Experimental setup showing major components.

4.2 Rotary Disc Target Holder Design

A 20.3 cm diameter rotary disc target holder (Figure 4-2) was manufactured using an abrasive waterjet machining centre from 0.32 cm thick rigid HDPE. The disk could hold up to four samples, placed inside four grooves which were 90° apart from each other, as shown in Figure 4-3. The grooves were 6.4 cm long to allow the sample to be placed at different radial distances. A 0.8 mm steel sheet was used to protect the HDPE disc from erosion and to clamp the samples (Figure 4-2). The steel sheet was designed such that only a 2 cm length of the samples was exposed to the micro-blaster nozzle. The steel sheet could be replaced very easily if required because it was easily machined using the abrasive water jet machining center. There were screw clearance holes in both the HDPE disc and the steel sheet for clamping of the samples. The disc and the sheet were compressed together in the central area using two HDPE flanges from both sides (Figure 4-2). Blasting was possible down to 9 cm radial distance using this mechanism.

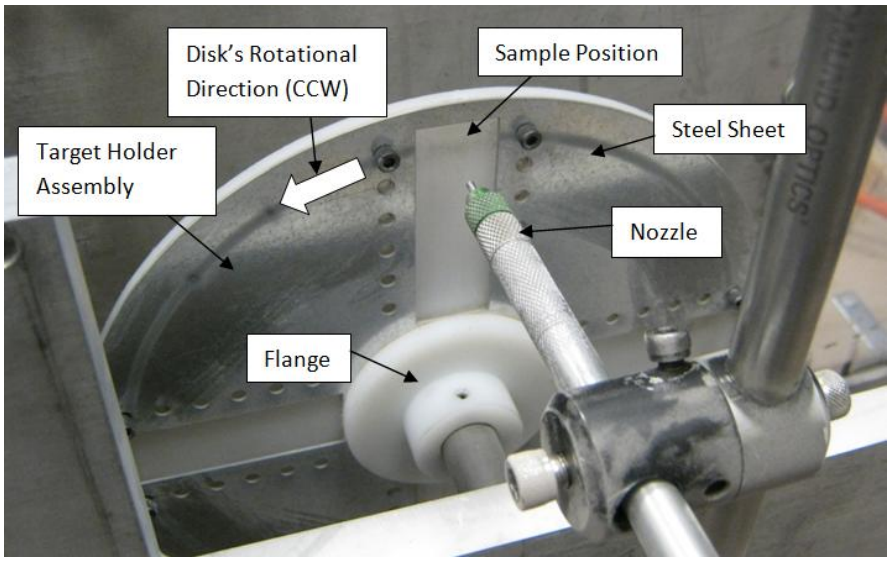

Figure 4-2: Rotary disc target holder assembly including nozzle position.

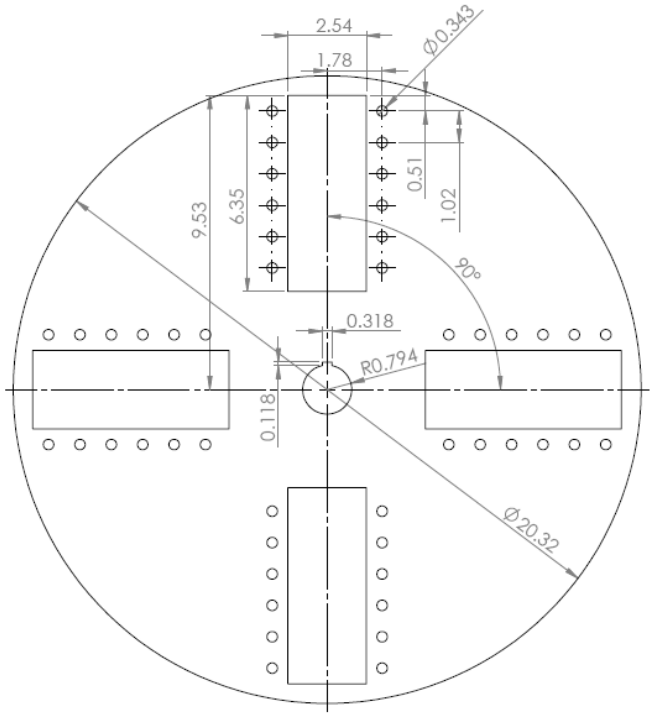

Figure 4-3: A 2D drawing of rotary disc target holder with dimensions in cm.

4.3 Experimental Procedure

The rotating disc allowed the reduction or increase of the relative particle tangential velocity depending on the disc rotating speed and impact angle. The apparatus enabled separate study of the effect of the particle velocity components, normal and tangential, on the erosion rates and mechanisms. This was useful for the study of the erosion rate change due to the change in tangential velocity component. The disc was positioned in front of the AccuFlo micro-blaster apparatus (Figure 4-2). For a static test at a shallower impact angles, the abrasive jet spreads over a larger area of the substrate, causing various effective impact angles throughout the channel cross-section (Figure 4-4). With this rotary disc apparatus, (when the disc rotated at a high speed) it was possible to achieve an almost half effective impact angle compared to the actual impact angle (see Equation 4-6 in Section 4.3.1 for equation to find effective impact angle). Furthermore, it could be used to obtain higher particle velocities with respect to the samples compared to the static tests. In the static test, the nozzle velocity of the particles is simply the

total velocity. However, using this apparatus, a tangential component of velocity could be added to the equation (Equation 4-5 in Section 4.3.1) of the total velocity.

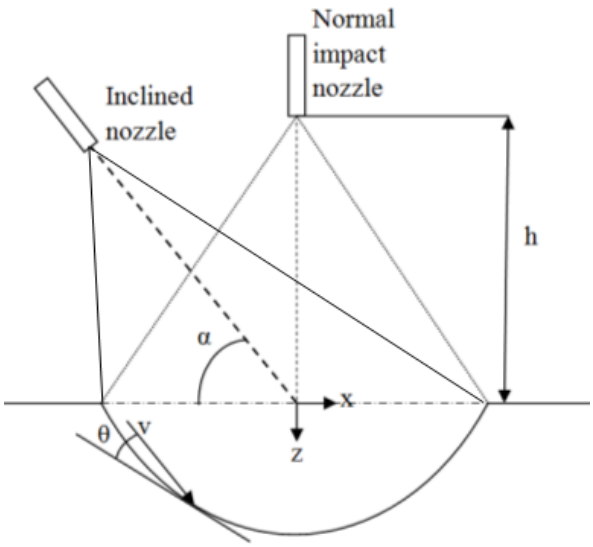

Figure 4-4: The global impact angle (α) and local impact angle (θ) of an oblique impact [9].

4.3.1 Velocity Component Calculations

At a given rotational speed, the linear velocity of the samples (V_d as seen in Figure 4-5), positioned at a certain distance from the centre of the disc (R_{Disc}), could be calculated. The tangential velocity of the particles (V_t) could also be calculated knowing the impact velocity (V_{Nozzle}) and impact angle (α). The difference between both velocities (V_d and V_t) was the relative tangential velocity (V_{rt}) of the particles. Henceforth in this thesis, the term 'tangential velocity' should be taken as the relative tangential velocity. If the linear target velocity (V_d) and tangential velocity (V_t) of the particles point towards opposite directions as shown in Figure 4-5 (b), then the relative tangential velocity is increased. Conversely, if the linear target velocity and tangential velocity of the particles point towards the same direction, the relative tangential velocity was decreased. The relative tangential velocity could also be cancelled with proper selection of motor speed and impact angle. Throughout this study, the disc rotated counter-clockwise within a speed range of 650-7,300 rpm.

The nozzle velocity was divided into two components as shown in Figure 4-5:

$$V_t = V_{Nozzle}\, cos(\alpha) \tag{4-1}$$

$$V_n = V_{Nozzle}\, sin(\alpha) \tag{4-2}$$

where, V_t = tangential velocity of the particles, V_n = normal velocity of the particles, V_{Nozzle} =the particle velocity at impact, and α = impact angle. The linear velocity of the samples due to disc rotation could be calculated as:

$$\boldsymbol{V_d = \omega} \text{ x } \boldsymbol{R_{Disc}} \tag{4-3}$$

where, $\boldsymbol{V_d}$ = the linear velocity of the samples mounted on the disc due to disc rotation, $\boldsymbol{\omega}$ = rotational speed of the motor, $\boldsymbol{R_{Disc}}$ = radial distance of samples from the center of the disc. The friction between particle and disc was ignored during V_d calculation because the impact time is negligible. Then the relative tangential velocity ($\boldsymbol{V_{rt}}$) due to sample rotation could be found as:

$$\boldsymbol{V_{rt} = V_d + V_t} \tag{4-4}$$

Finally, the total velocity (V_{Total}) and effective impact angle (α_E) becomes:

$$V_{Total} = \sqrt{(V_{rt}^2 + V_n^2)} \tag{4-5}$$

$$\alpha_E = \tan^{-1}\left(\frac{V_n}{V_{rt}}\right) \tag{4-6}$$

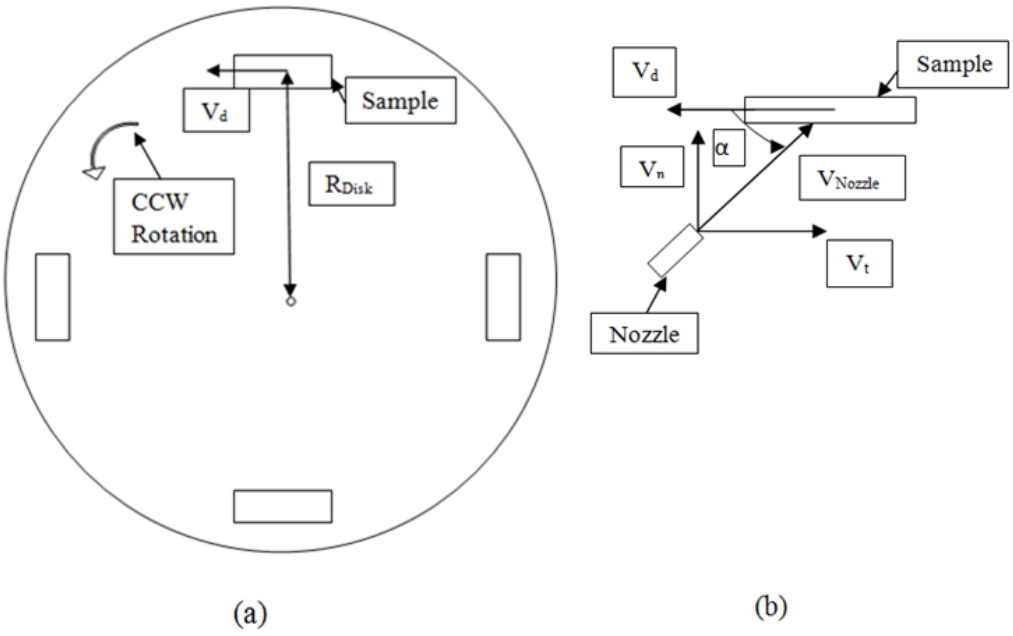

Figure 4-5: (a) Simplified front view of the apparatus, (b) top view of the apparatus showing velocity components (drawing is not to the scale).

In addition to a normal velocity and a relative tangential velocity, the placement of the samples on a rotating disc during solid particle impact introduced a radial motion to the impacting solid particles that may affect the erosion mechanism. However, the effect of this radial motion, which was primarily due to rotation, was found to be negligible. The analysis of the negligible radial motion, similar to that presented in Ref. [24], can be found in appendix D.

4.3.2 Erosion Rate Measurement

Erosion rate (mg/g) is defined as the mass of the target material removed (mg) per unit mass of abrasive used (g) [19]. The mass flow rate of the abrasive was measured using an enclosed container fitted with filter paper at the entrance to retain the particles while ensuring that there was an insignificant back pressure on the nozzle. The container was weighted using a digital mass balance (model CP 224S, Sartorius AG, Goettingen, Germany, with an accuracy of

± 0.01 mg) before and after blasting inside it for one minute Then the mass flow rate was extracted from the simple formula:

$$\dot{m} = \frac{m_f - m_i}{t} \tag{4-7}$$

where, $\dot{m}$ = abrasive mass flow rate (g/s), m_f = measured mass of the container after blasting (g), m_i = initial mass of the container before blasting (g), t = time duration of the blasting (s). The mass flow rate was measured at least two times before and two times after each test, and kept sufficiently low (depending on particle size and pressure used), so that the interference between incoming particles and those rebounding from the surface could be considered negligible [53, 54, 55]. Abrasive level in the tank was kept sufficiently high, and a mixing device was utilized to ensure the mass flow rate repeatability [58]. The mass flow rates and coefficient of variation for each experiment are given in Sections 5.1-5.3. The standard deviation of the mass flow rate before and after the test was found to be within 8% of the mean mass flow rate. The total mass of abrasives used on one sample during the test could be calculated from the equation below:

$$\textit{Total mass of used abrasives} = (\dot{m})\,(\textit{Dosage time}) \tag{4-8}$$

where, $\dot{m}$ = mean mass flow rate, and dosage time for this new experimental setup has been calculated in Section 4.3.3. The samples were blown with compressed air prior to determining the mass loss due to erosion, in order to minimize contamination by deposited particles. The mass reduction of the samples due to erosion was measured in two different methods: gravimetric (by weighing the samples before and after blasting using the digital mass balance), and volumetric (by measuring the channel volume using an optical profilometer (model ST400, Nanovea, Irvine, CA, USA,) with a depth resolution of 10 nm). For the volume measurement using the profilometer, the average of four two dimensional profiles measured across the channel width was multiplied by the channel length (which was 2 cm). The volume (cm^3) was multiplied by the 2.2 g/cm^3 density [62] of the borosilicate glass to determine the mass loss (g). Each data

point in the graphs (shown in Chapter 5) represented erosion rate of one sample measured by profilometer. Erosion rate of three samples were measured for each experiment.

4.3.3 Dosage Time Calculation

When abrasive was blasted and the disc was rotating, the samples were blasted only a small fraction of the total blasting time. That fraction of time was defined as dosage time. Only 2 cm of each sample were exposed for blasting. Assuming the sample position was at the furthest radial distance of 9 cm (Figure 4-6). The fraction of total blasting time one sample was exposed was:

$$\text{Fraction of time} = \frac{2.03}{2\pi r} = \frac{2.03}{2\pi\ 9.02} = 0.0359 \text{ or } 3.59\% \qquad (4\text{-}9)$$

This means the actual blasting dosage time on each sample was only 3.59% of the total blasting time, e.g., if the total blasting time was 5 min., the dosage time was only 10.8 s.

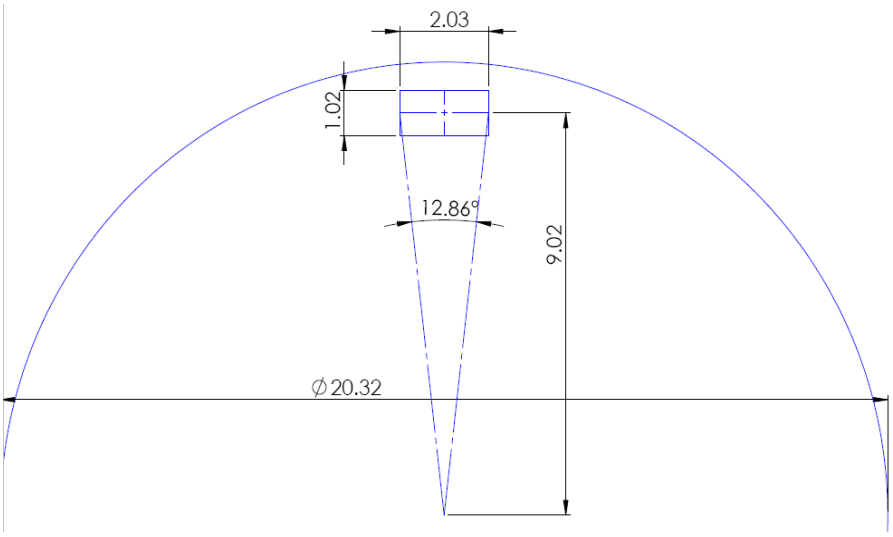

Figure 4-6: Dosage time calculation of the rotating disc (unit in cm).

4.4 Velocity Estimation Technique

Particle impact velocity depends on the air pressure, the particle size, the nozzle geometry, particle density, air density, air flow velocity and particle drag coefficient [63, 64]. Li et al. [65] developed a mathematical free-jet model to determine the particle velocity in a given location within an abrasive air jet. The model predicted a Gaussian or bell shape velocity profile across the jet with a maximum particle velocity at the jet center. Dehnadfar et al. [63] measured the particle velocities across the free-jet at a distance of 20 mm from the 0.76 mm inner diameter nozzle exit using laser shadowgraphy and compared the results to the model of Li et al. They [63] also found Gaussian velocity distribution which agreed with the model of Li et al. quite well for spherical particles but differed for the angular particles. The model of Li et al. significantly under predicted the measured particle velocity distribution because they assumed the particle to be spherical and thus did not account for the different particle drag coefficient for angular particles in their model. If the particles are non-spherical, the particle velocity distribution strongly depends on the drag coefficient, which in turn, depends on the particle shape and orientation. Therefore, Dehnadfar et al. introduced the drag coefficient into the model of Li et al. They measured the average sphericities of the powders using shadowgraphic images. With this modification of the drag coefficient, there was excellent agreement with the measured velocities for the spherical and non-spherical particles. Jafar et al. [59] measured the average particle velocities across the free-jet for 1.5 mm inner diameter nozzle at a 10 mm standoff distance using shadowgraphy method. Jafar et al.'s velocity data for 1.5 mm inner diameter nozzle was utilized in the present work in order to estimate the particle velocity at a given pressure.

4.5 Scatter Test

The rotary disc target holder could accommodate four samples. To utilize this advantage, it was necessary to investigate the variation in erosion rates from sample to sample, and from experiment to experiment. If the sample to sample variation was in same order of magnitude compared to experiment to experiment variation, it might be valid to represent three samples from one experiment as experimental scatter. Three experiments were performed at the same experimental conditions, each experiment containing three samples. Borosilicate samples blasted

by 25 μm alumina at 300 kPa for 3 minutes with the disc speed constant at 800 rpm. The erosion rate for each sample was measured using the optical profilometer. The average erosion rate of the three samples from each experiments was 11.20, 11.61, and 11.63 mg/g with a standard deviation of 0.183 (1.6%), 0.185 (1.6%), and 0.169 (1.5%) mg/g respectively. When three (same position on the disc) samples from three separate experiment were taken, the average erosion rate was 11.54, 11.29, and 11.61 mg/g with a standard deviation of 0.170 (1.5%), 0.261 (2.3%), and 0.305 (2.6%) mg/g. A scatter plot for nine samples is shown in Figure 4-7. As seen from data and graph comparison, the sample to sample variation was on the same order of magnitude with the experiment to experiment variation. So, each experiment was performed once using three samples for the scatter.

As mentioned in Section 4.3.2, both gravimetric and volumetric methods were used to calculate the erosion rate. The erosion rate from the mass loss measurements agreed with the volumetric profilometer measurements within 6.9% (Figure E-1 in Appendix E). The samples might have lost some mass while mounting and removing from the target holder, which was not due to the erosion by particles. This was probably the main reason behind the mass loss measurements overestimation from profilometer measurements. Although both methods were used for each erosion measurements, only the profilometer measurements were reported in Chapter 5. The gravimetric erosion rate measurement results were shown in Appendix E.

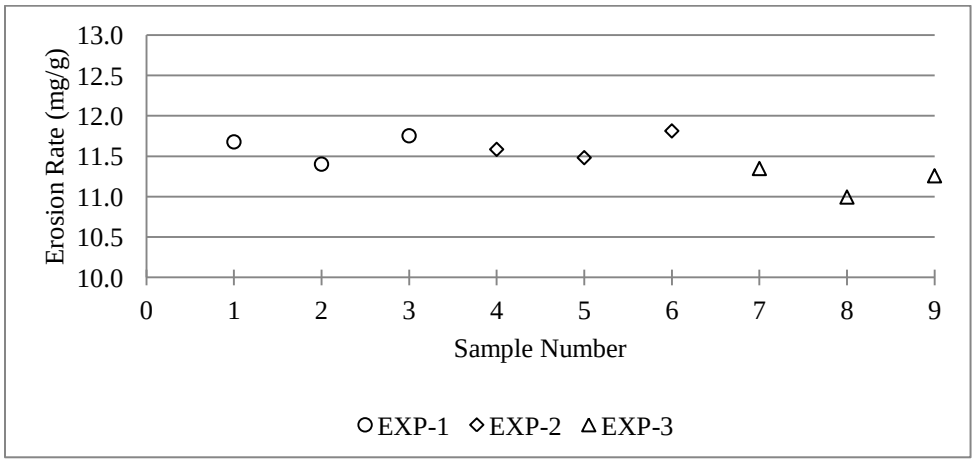

Figure 4-7: Scatter plot to compare sample to sample vs. experiment to experiment repeatability.

Chapter 5: Results and Discussion

This chapter presents the results of the erosion rate experiments performed using borosilicate glass samples on the rotary disc apparatus. The main advantage of this apparatus was that the tangential velocity component of the particle velocity could be easily changed by changing the rotational speed, thus lowering the effective angle of attack, and allowing erosion tests to be performed at relatively higher velocities. First, the dependence of the erosion rate on the tangential component of velocity was investigated experimentally for the borosilicate glass samples. Second, the erosion rate of glass as a function of impact angle was studied. Finally, the velocity exponent for borosilicate glass was determined experimentally. The experimental results are presented and discussed in the following sections.

5.1 Dependence of Borosilicate Glass Erosion Rate on Tangential Velocity

The relationship between the erosion rate and the tangential velocity component was studied experimentally. The investigation was divided into two parts. First, experiments were performed by changing the tangential velocity from 0–93 m/s while keeping the normal component of velocity constant. These experiments were conducted for three different constant normal components of velocity i.e., 75, 100, and 121 m/s for 50 μm granular aluminum oxide (alumina) particles. Later, the effect of particle size was investigated using three different sizes of particle i.e., 50, 100, and 150 μm angular alumina at 75 m/s constant normal velocity. The dependence of surface roughness on tangential velocity for borosilicate glass was also investigated (shown in Appendix F). It was found that the surface roughness was independent of tangential velocity; rather it depended upon the normal velocity and particle size.

5.1.1 Experiments at Constant Normal Velocity

The blasting pressure, impact angle and disc speed were varied in order to keep the normal velocity constant at 75, 102, and 121 m/s, while the tangential velocity varied in the range 0 to 93 m/s. The glass samples were mounted 9 cm from disc centre to maximize the tangential velocity. A 1.5 mm inner diameter nozzle at a 1 cm standoff distance and 50 μm

alumina as media were used for all experiments. Impact angles more than 90° were used to achieve a zero tangential velocity or 90° effective angle of attack. This means the nozzle was positioned in the same direction of the disc rotation. This way it was possible to cancel the tangential velocity due to sample rotation with the tangential component of nozzle velocity (see Figure 4-4 for clarification).

A summary of the experimental parameters for borosilicate glass impacted by 50 μm alumina particles at constant normal velocities of 75, 102, and 121 m/s are shown in Tables 5-1 to 5-4. In the tables the coefficients of variation for mass flow rate were calculated by [standard deviation/average] x 100%. The mass flow rates in Table 5-1 were sufficiently low to create negligible interference between incoming particles and those rebounding from the surface [60, 61]. The powder level in the reservoir was maintained at approximately a constant level to enhance repeatability [58]. Channels depths were kept below 220 μm with an aspect ratio (channel depth to width ratio) of 0.07 to ensure that the global impact angle and the local impact angle were effectively the same. The channels had relatively uniform profiles, with a maximum of 2.1% error [(profile area - mean profile area)/mean profile area] in profile area measurements and 0.02% error in centreline channel length measurements.

Table 5-1: Experimental parameters for constant normal velocities using 50 μm alumina.

Normal Velocity (m/s)	Tangential Velocity Range (m/s)	Mass Flow Rate Range (g/min)	Coefficient of Variation range (%)	Channel Depth Range (μm)
75	0-93	5.8-7.6	1.9-8.3	70-125
102	0-93	7.2-9.2	1.1-3.5	140-180
121	0-99	8.7-9.8	1.1-6.2	170-220

Table 5-2: Experimental parameters for 50 μm alumina at 75 m/s constant normal velocity.

Disc Speed (rpm)	Impact Angle (°)	Tangential Velocity (m/s)	Normal Velocity (m/s)	Total Velocity (m/s)	Effective Impact angle (°)	Blasting Pressure (kPa)
970	97	0.0	75.1	75.1	90.0	80
1665	83	25.1	75.1	79.2	71.5	80
1430	64	50.3	75.2	90.5	56.2	100
1460	51	75.0	75.5	106.4	45.2	140
1565	44	92.8	75.2	119.5	39.0	180

Table 5-3: Experimental parameters for 50 μm alumina at 102 m/s constant normal velocity.

Disc Speed (rpm)	Impact Angle (°)	Tangential Velocity (m/s)	Normal Velocity (m/s)	Total Velocity (m/s)	Effective Impact angle (°)	Blasting Pressure (kPa)
945	95	0.0	102.5	102.5	90.0	160
1680	85	25.0	102.5	105.5	76.3	160
1545	71	50.0	102.4	113.9	64.0	180
865	57	74.9	102.6	127.0	53.9	240
730	50	93.0	102.5	138.4	47.8	300

Table 5-4: Experimental parameters for 50 μm alumina at 121 m/s constant normal velocity.

Disc Speed (rpm)	Impact Angle (°)	Tangential Velocity (m/s)	Normal Velocity (m/s)	Total Velocity (m/s)	Effective Impact angle (°)	Blasting Pressure (kPa)
1825	98	0.4	121.1	121.1	89.8	240
840	82	25.0	121.1	123.7	78.3	240
1585	74	49.9	121.4	131.3	67.6	260
1910	65	74.7	121.3	142.5	58.4	300
1800	56	99.1	121.5	156.8	50.8	380

Figure 5-1 shows the three repeat measurements of the erosion rates plotted for the three different constant normal velocities i.e., 75, 102, 121 m/s in a single graph. As expected, the magnitude of the erosion rate increased with the increase in constant normal velocity at a fixed tangential velocity [2, 46-48]. Most researchers have assumed that the normal velocity is the only factor causing erosion in brittle material through crack initiation and propagation [1-5, 19]. For example, in the surface evolution modeling of features machined into glass using AJM, researchers [1, 3, 19] have commonly assumed that only the kinetic energy transfer normal to the target surface contributes to the advancement of the eroded surface. [2, 46-48]. According to this assumption, if the normal velocity is kept constant, the erosion rate should not change. However, the results of Figure 5-1 contradict this commonly held notion, since the tangential velocity component clearly affected the erosion rate. In other words, tangential component of velocity cannot be neglected in modeling erosion mechanism of glass.

To better assess the relative magnitude of change in erosion rate due to tangential effects, the normalized erosion rate (ratio of erosion rate at a given tangential velocity to that at zero tangential velocity) is plotted as a function of tangential velocity in Figure 5-2. The erosion rate at 75 m/s constant normal velocity had the maximum relative magnitude change. An increase in tangential component of velocity of 93 m/s increased the erosion rate by 55% for 75 m/s constant normal velocity, whereas the increases were only 13% and 44% for 102 m/s and 121 m/s constant normal velocities, respectively. The increase in erosion rate (13%) was smaller for 102 m/s constant normal velocity compared to 75 m/s (55%) and 121 m/s (44%). The erosion rate increase for 75 m/s was the highest; this might be due to the fact that tangential velocity increase of 93 m/s was relatively high compared to the 75 m/s constant normal velocity. However, using this reasoning, the erosion rate increase for 121 m/s should have been the lowest, which was not true. Apparently the mechanisms governing the increase in erosion rate due to the tangential velocity are complex. This may indicate that the amount of lateral crack propagation depends on an interrelation of normal and tangential velocity components, a topic for future work.

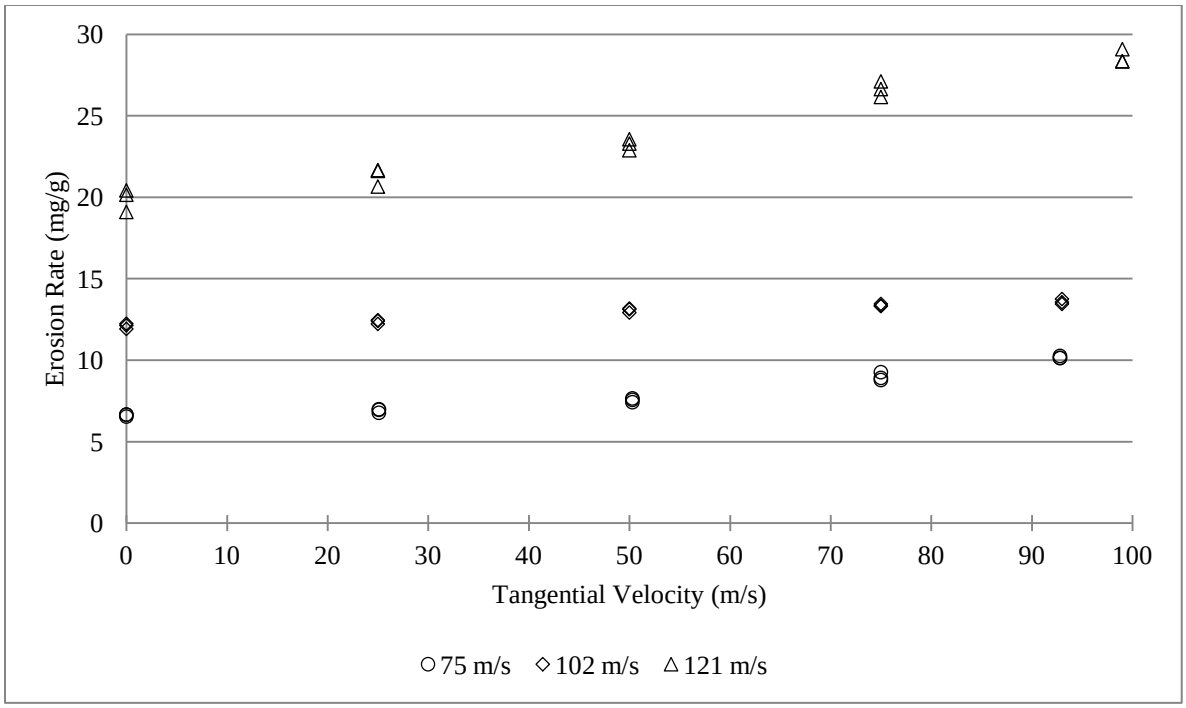

Figure 5-1: Erosion rate as a function of tangential velocity for borosilicate glass impacted by 50μm alumina particles at constant normal velocities of 75, 102, and 121 m/s.

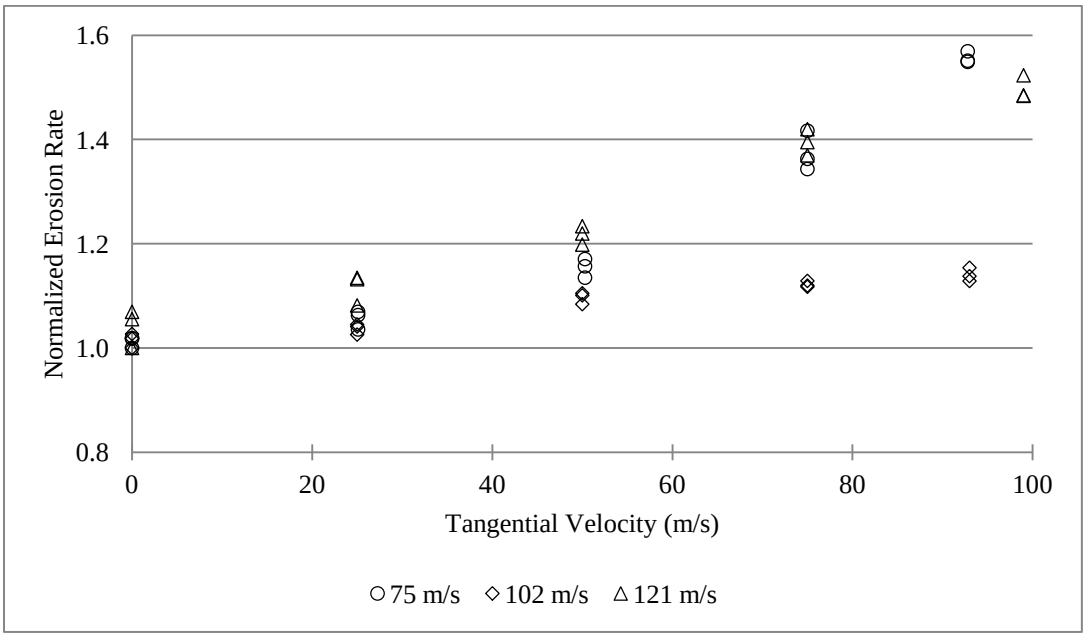

Figure 5-2: Normalized erosion rate vs. tangential velocity plot for borosilicate glass impacted by 50 μm alumina particles at constant normal velocities of 75, 102, and 121 m/s.

Figure 5-3 shows that the average erosion rate increased linearly with increasing total kinetic energy on a logarithmic scale. For this graph, the kinetic energy was calculated for each impacting particle assuming a spherical particle with a diameter equal to the nominal size of the particle. Particle size and shape were constant throughout this set of experiments, and the normal velocity was constant for each line. Only the total velocity increased due to the increase in tangential velocity. The slopes of the lines were 0.48 for 75 m/s, 0.19 for 102 m/s, and 0.69 for 121 m/s constant normal velocity. As mentioned before, from Figure 5-2, the relative erosion rate increase due to tangential velocity was the highest for 75 m/s constant normal velocity. As a function of total energy (comparing the slopes), the 121 m/s constant normal velocity case has the highest magnitude of change (slope was 0.69 for 121 m/s, compared to 0.48 for 75 m/s, and 0.19 for 102 m/s) in erosion rate. In Figure 5-3, the change in total kinetic energy was only due to the change in tangential component of kinetic energy because the normal kinetic energy was kept constant (both normal velocity component and particle size were constant). So the increasing trend of each line indicates the significance of the tangential component of kinetic energy. The slope of the lines may also be related to a tangential kinetic energy exponent similar to the normal kinetic energy exponent found in Refs. [4, 5]. These tangential kinetic energy exponents were much lower than the normal kinetic energy exponents i.e., 1.23 [4], and 1.42 [5] reported for Pyrex.

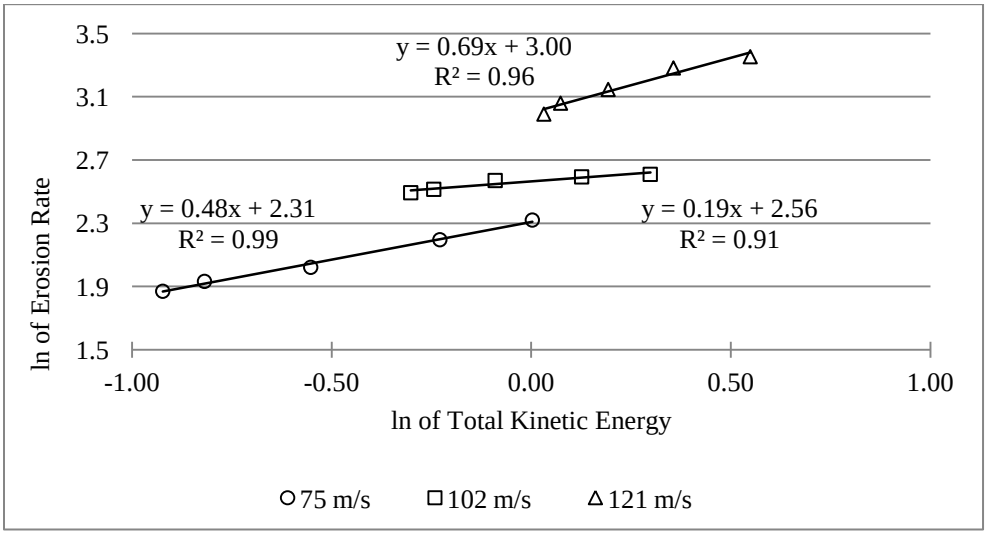

Figure 5-3: Logarithmic plot for erosion rate (mg/g) and total kinetic energy (μJ) of impacting particle at three different i.e., 75, 102, and 121 m/s constant normal velocities.

The erosion rate magnitude increased with increasing normal velocity from 75 to 121 m/s, which was expected. Srinivasan and Scattergood [21] conducted single impact studies using 80 grit (200 μm) alundum particles on window-plane glass in order to compare between normal and low-angle impact conditions at the same normal component of particle velocity. Based on these experiments, they calculated the probabilities of the occurrence of chip removal and non-removal events as fraction of the total impact events. They found that lateral crack extensions due to single impacts occur in all directions, and chipping probability increased with an increase of tangential velocity component at a constant normal velocity.

Two mechanisms are responsible in the erosion of glass: (i) material removal by cutting or ploughing; (ii) material removal due to the formation of cracks and crack propagation [35]. The dominant erosion mechanism for brittle materials is chip removal of the target material above the cracks [19]. A chip is removed if the lateral crack resulting from the impact deflects upward and intersects the surface. If the lateral crack remains below the surface, no chip is removed [21]. As seen in Figure 5-4, at a shallower impact angle, the lateral crack propagates in the forward direction of the tangential particle velocity. So the impact energy released by this crack propagation is more concentrated in one direction [23]. In contrast, as the impact angle increases the lateral cracks propagate in various directions, so less relative concentration of energy occurs [23]. Since tangential velocity dominated at shallower impact angles, more energy was released by the lateral crack propagation, and relatively larger pieces of the target material were chipped and removed than would have been without tangential velocity at the same normal velocity. This explains the dependence of erosion rate on tangential velocity.

The present results are also in agreement with Srinivasan and Scattergood [21], who has experimentally shown that at the same normal component of velocity, an impact at a shallow-angle produces a larger lateral crack extension than at a normal impact angle. The chipping probability is higher for low-angle impact than the normal impact at constant normal component of velocity. Assuming that the erosion rates are proportional to chipping probability, this suggests that oblique incidence should result in more erosion than normal incidence at the same normal velocity component. This explains why the erosion rate increased with increasing tangential velocity, even though the normal velocity was constant.

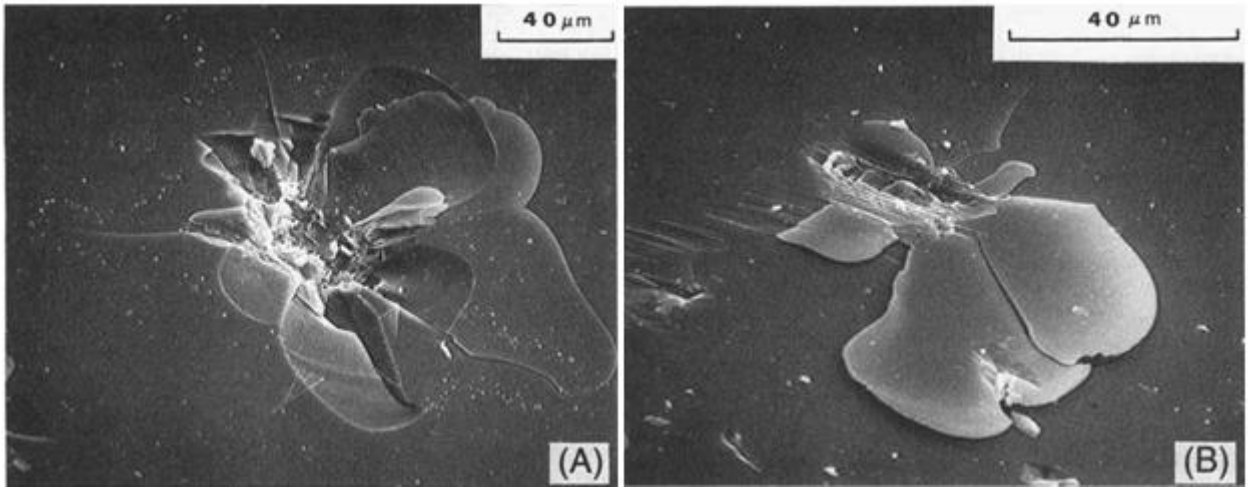

Figure 5-4: Scanning electron micrographs of glass surfaces impacted with 100-mesh SiC particles (A) at normal impact and (B) at 15º impact angle [66]

5.1.2 Particle Size Effects

The effect of particle size was also investigated at 75 m/s constant normal velocity by performing erosion rate experiments using 50, 100, and 150 μm nominal diameter particles. The erosion test parameters for 50 μm particles at 75 m/s constant normal velocity have been shown previously in Table 5-2. A summary of the experimental parameters for 100, and 150 μm alumina particles at constant normal velocities of 75 m/s are shown in Tables 5-5 to 5-7. The mass flow rate was higher for 100 and 150 μm particles compared to 50 μm because larger particles have higher mass. The mass flow rates in Table 5-5 were sufficiently low to create negligible interference between incoming particles and those rebounding from the surface [60, 61]. The powder level in the reservoir was maintained at approximately a constant level to enhance repeatability [58], as seen from the Table 5-5 that the mass flow rate fluctuation was less than 3.3%. Channels depths were kept below 240 μm with an aspect ratio of 0.08 to ensure that the global impact angle and the local impact angle were effectively the same, so that the erosion rate was not affected. The channels had relatively uniform profiles, with a maximum of 1.8% error in profile area measurements and 0.03% error in centreline channel length measurements.

Table 5-5: Experimental parameters for 50, 100, and 150 μm alumina particles at 75 m/s constant normal velocity.

Particle Size (μm)	Tangential Velocity Range (m/s)	Mass Flow Rate Range (g/min)	Coefficient of Variation range (%)	Channel Depth Range (μm)
50	0-93	5.8-7.6	1.9-8.3	70-125
100	0-93	13.3-19.6	1.7-3.3	100-200
150	0-93	14.8-23.8	80-240	170-220

Table 5-6: Experimental parameters for 100 μm alumina at 75 m/s constant normal velocity.

Disc Speed (rpm)	Impact Angle (°)	Tangential Velocity (m/s)	Normal Velocity (m/s)	Total Velocity (m/s)	Effective Impact angle (°)	Blasting Pressure (kPa)
830	96	0.0	75.0	75.0	90.0	150
1805	84	25.1	75.0	79.1	71.5	150
665	59.5	50.5	75.0	90.4	56.0	200
1230	52.1	70.1	75.0	102.6	46.9	240
1055	42.1	93.0	75.0	119.6	38.9	340

Table 5-7: Experimental parameters for 150 μm alumina at 75 m/s constant normal velocity

Disc Speed (rpm)	Impact Angle (°)	Tangential Velocity (m/s)	Normal Velocity (m/s)	Total Velocity (m/s)	Effective Impact angle (°)	Blasting Pressure (kPa)
985	97	0.2	75.1	75.1	89.9	190
1660	83	25.0	75.1	79.2	71.6	190
940	62	48.9	75.1	89.6	56.9	240
1425	53	70.5	75.6	103.3	47.0	300
1630	44	93.3	75.1	119.8	38.8	400

Figure 5-5 shows three repeat measurements of the erosion rate at each tangential velocity plotted for the three different particle sizes i.e., 50, 100, 150 µm alumina at a 75 m/s constant normal velocity. The magnitude of the erosion rate increased with an increase in particle size at a fixed tangential velocity. This was expected because larger particles have higher kinetic energies associated with the component of velocity normal to the target surface, and thus remove larger chips, causing a higher erosion rate [12, 14, 16, 31].

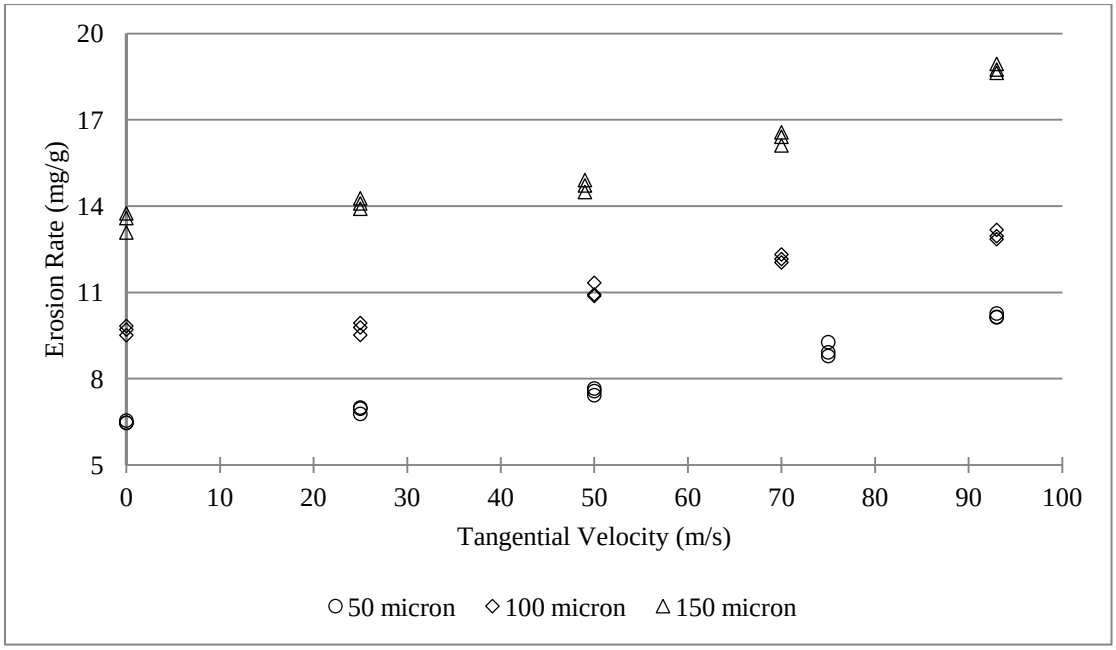

Figure 5-5: Erosion rate as a function of tangential velocity plot for three different alumina particle sizes i.e., 50, 100, and 150 µm at 70 m/s constant normal velocity.

To better assess the relative magnitude of change in erosion rate, the normalized erosion rate is plotted as a function of tangential velocity in Figure 5-6. The erosion rate using 50 µm particles had the maximum relative magnitude change. An increase in tangential component of velocity of 93 m/s increased the erosion rate by 55% for 50 µm particles, whereas the increases were only 36% and 43% for 100 µm and 150 µm particles, respectively. Although the magnitude of erosion rate increased with increasing particle size, the normalized erosion rate increase was lower for 100 and 150 µm alumina particles compared to 50 µm particles. This happened

probably because as the particle became larger, the crater or indent size was deeper for larger particles making it more difficult for the tangential velocity to affect the lateral crack extension. Considering the first four tangential velocities (0-75 m/s) in Figure 5-6, the changes were however within the limit of an experimental scatter.

The erosion rate increased due to the increase in tangential velocity of 93 m/s although the normal velocity was kept constant at 75 m/s. This similar trend occurred for three different particle sizes. This again proves that the erosion rate of glass is not only dependent on normal component of velocity, but both the normal and tangential velocity components.

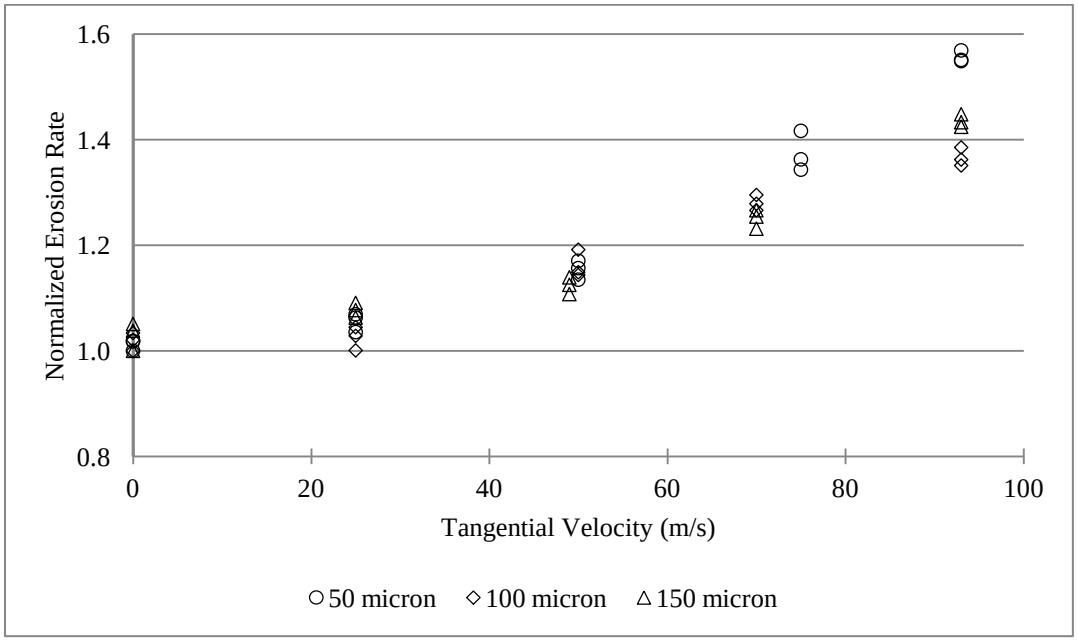

Figure 5-6: Normalized average erosion rate vs. tangential velocity on glass for three different alumina particle sizes i.e., 50, 100, and 150 µm at 70 m/s constant normal velocity.

The erosion rate as a function of total kinetic energy was plotted on logarithmic plots (Figure 5-7) for the three different particle sizes i.e., 50, 100, and 150 µm. This graph was similar to Figure 5-3 and all the assumptions made in calculating kinetic energy were the same. The logarithm of erosion rate increased linearly with the logarithm of the kinetic energy increase. The

slopes of the lines were 0.48 for 50 μm, 0.34 for 100 μm, and 0.34 for 150 μm alumina particles. The relative erosion rate increase for 50 μm particles was the highest, and other two particle sizes i.e., 100 and 150 μm had a similar increase rate. At a specific particle size and constant normal kinetic energy, the erosion rate increased linearly with total kinetic energy. This was again indicative of tangential kinetic energy effect on erosion rate. The conclusion is once again that both the normal and tangential velocity components and their relative magnitudes play a role in lateral crack extension leading to chip removal.

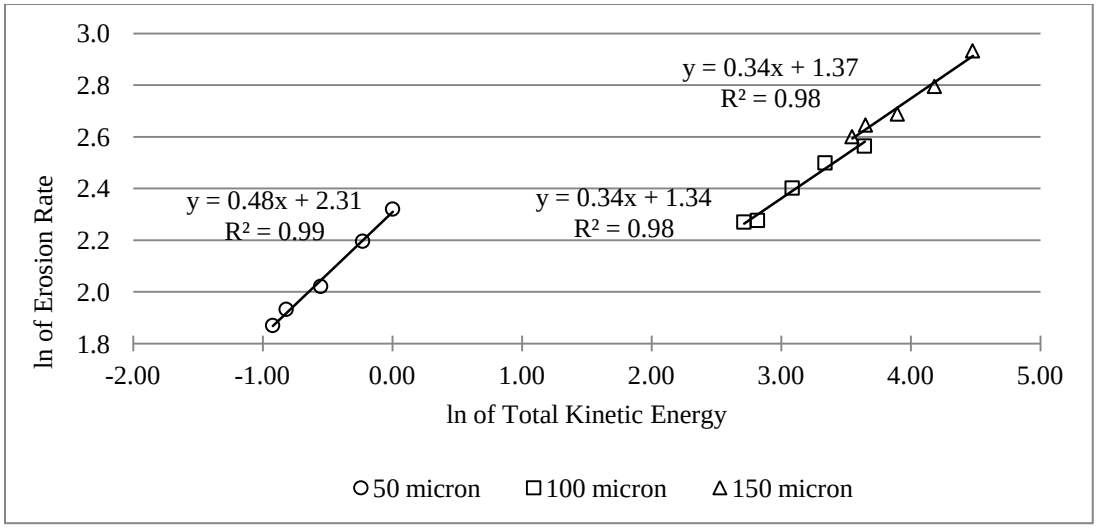

Figure 5-7: Logarithmic plot for erosion rate (mg/g) vs. kinetic energy (μJ) of impacting particle at three different i.e., 50, 100, and 150 μm alumina particles at 75 m/s constant normal velocities.

5.2 Dependence of Borosilicate Glass Erosion Rate on Impact Angle at a Constant Total Incident Velocity

Solid particle erosion testing at shallow angles of impact was limited by geometric constraints. On a static test (target static), at a shallower impact angle the abrasive jet spreads over a larger area of the substrate, causing a large range effective impact angles throughout the channel cross-section (Figure 4-4). With the rotary disc apparatus, it was possible to achieve an almost half effective impact angle compared to the actual impact angle (see Equation 4-6 in Section 4.3.1). Furthermore, it could be used to obtain higher particle velocities with respect to the samples compared to the static tests. Impact angle dependence erosion rate experiments for

borosilicate glass were performed for three different constant total velocities i.e., 100, 120, and 135 m/s using 50 μm nominal diameter granular alumina particles. In order to keep the total velocity constant and vary the effective angle of attack, parameters such as the blasting pressure, impact angle, and disc speed, were varied. The glass samples were mounted 9 cm from disc centre in all cases, except for the 10º impact angle experiments where the samples were at 6 cm from the disc centre. A 0.76 mm inner diameter nozzle at a 2 cm standoff distance was used in all the experiments.

A summary of the experimental parameters for borosilicate glass impacted by 50 μm alumina particles at constant total velocities of 100, 120, and 135 m/s are shown in Tables 5-8 to 5-11. The mass flow rates in Table 5-8 were sufficiently low to create negligible interference between incoming particles and those rebounding from the surface [60, 61]. The powder level in the reservoir was maintained at approximately a constant level to enhance repeatability [58], as seen from the Table 5-8 that the mass flow rate fluctuation was less than 5.2%. Channels depths were kept below 130 μm with an aspect ratio of 0.04 to ensure that the global impact angle and the local impact angle were effectively the same, so that the erosion rate was not affected. The channels had relatively uniform profiles, with a maximum of 3.1% error in profile area measurements and 0.05% error in centreline channel length measurements.

Erosion rates were plotted against effective impact angle for all three total velocities i.e., 100, 120, and 135 m/s in Figure 5-8. As the impact angle increased, the erosion rate increased with a maximum at normal impact, which is typical brittle erosive behavior [6, 36, 43]. Figure 5-8 below shows erosion data for a total of 54 samples.

Table 5-8: Experimental parameters for 50, 100, and 150 μm alumina particles at 75 m/s constant normal velocity.

Constant Total Velocity (m/s)	Mass Flow Rate Range (g/min)	Coefficient of Variation range (%)	Channel Depth Range (μm)
100	1.6-3.6	1.9-4.1	5-40
120	2.3-3.5	2.8-5.2	7-75
135	2.9-4.4	1.1-4.4	7-130

Table 5-9: Experimental parameters for 50 μm alumina at 100 m/s constant total velocity.

Disc Speed (rpm)	Impact Angle (°)	Tangential Velocity (m/s)	Normal Velocity (m/s)	Total Velocity (m/s)	Effective Impact angle (°)	Blasting Pressure (kPa)
7150	25	99.7	16.5	101.1	9.4	20
1210	23	93.7	34.9	100.0	20.4	100
1410	40	81.8	57.4	100.0	35.0	100
1960	60	63.3	77.3	100.0	50.7	100
1250	83	23.8	97.1	100.0	76.2	120
780	94	0.1	100.1	100.1	90.0	130

Table 5-10: Experimental parameters for 50 μm alumina at 120 m/s constant total velocity.

Disc Speed (rpm)	Impact Angle (°)	Tangential Velocity (m/s)	Normal Velocity (m/s)	Total Velocity (m/s)	Effective Impact angle (°)	Blasting Pressure (kPa)
7085	25	114.7	23.7	117.1	11.7	40
820	23	111.6	44.1	120.0	21.5	160
980	40	95.7	72.5	120.0	37.1	160
1400	60	69.7	97.6	120.0	54.5	160
1400	83	27.7	116.7	120.0	76.7	200
880	94	0.0	119.4	119.4	90.0	220

Table 5-11: Experimental parameters for 50 μm alumina at 135 m/s constant total velocity

Disc Speed (rpm)	Impact Angle (°)	Tangential Velocity (m/s)	Normal Velocity (m/s)	Total Velocity (m/s)	Effective Impact angle (°)	Blasting Pressure (kPa)
7145	25	126.8	29.1	130	12.9	60
1300	23	126.1	48.3	135.0	20.9	260
1530	40	109.2	79.4	135.0	36.0	260
1640	60	78.9	109.6	135.0	54.2	300
1000	75	43.7	127.7	135.0	71.1	400
1740	97	0.0	135.0	135.0	90.0	500

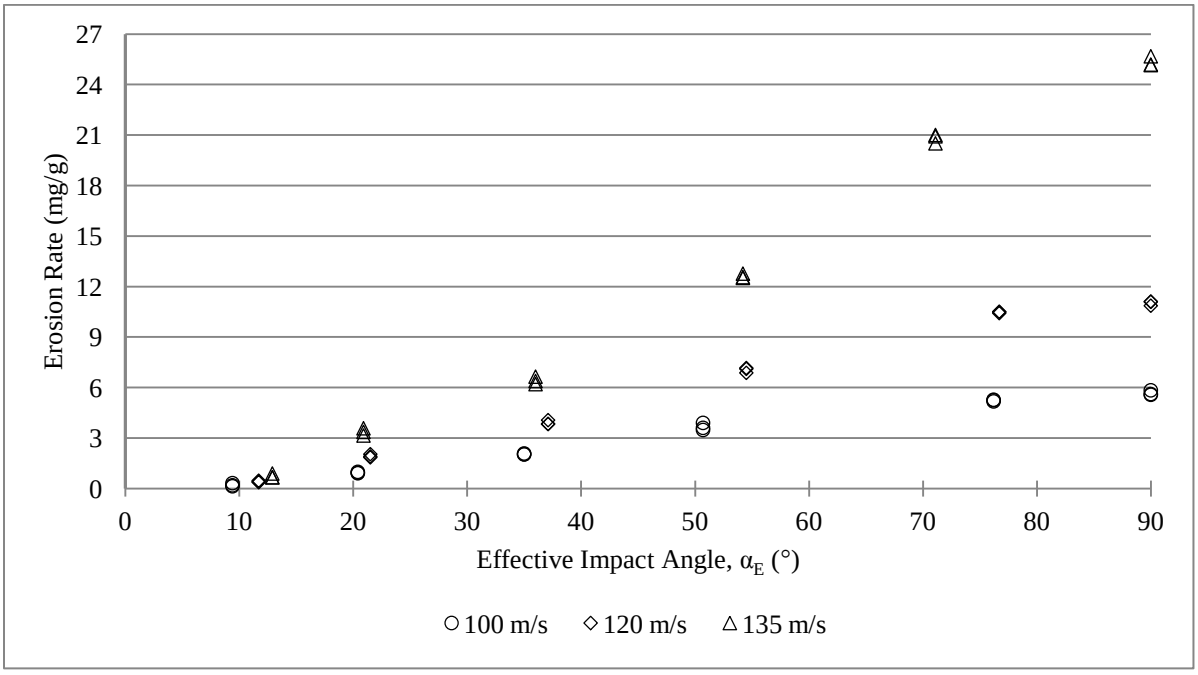

Figure 5-8: Erosion rate vs. effective impact angle for borosilicate glass impacted by 50 μm alumina with constant total velocity of 100, 120, and 135 m/s, and effective impact angles ranging from 9° to 90°.

The magnitude of erosion rate increased with the total velocity which was expected. There are several models for the erosion rate on brittle materials [2, 36], in which the erosion rate depends on the particle impact velocity. In this case, the erosion rate is roughly proportional to the component of the impact velocity normal to the substrate [6, 23, 35, 66]. However, the erosion rate was not completely dependent on normal component of velocity, as shown in Figure 5-9. In this figure, normalized erosion rates were plotted against effective impact angle. It is seen that that the normalized erosion rate (ratio of erosion rate at oblique impact and erosion rate at normal impact) depends only slightly on impact velocity for borosilicate glass. This agrees with the findings of Oka et al. [6] for alumina (ceramic, brittle material) substrate impacted by silicon dioxide (SiO_2, 254 μm) and silicon carbide (SiC, 326 μm) particles. If the erosion rate were to only depend on the normal component of velocity as discussed by Ghobeity et al. [1], the normalized erosion rate versus effective impact angle plot should follow a $[\sin(\alpha_E)]^{1.43}$ curve (the experimental data points should all fall on the same line), which clearly did not happen. The data points found to be lower than the sine curve instead of higher, although there was both velocity components present at oblique incident. It seems that the tangential velocity component did not contribute much in crack propagation as expected. It was inferred from Figure 5-9 that the data points for 135 m/s constant total velocity were furthest away from the sine curve, while that of 100 m/s were the closest. This suggests that at a higher total velocity the difference was higher due to the effect of tangential velocity. Also the data was much lower at intermediate impact angles. This topic needs further investigation to apply it into surface evolution modelling of borosilicate glass.

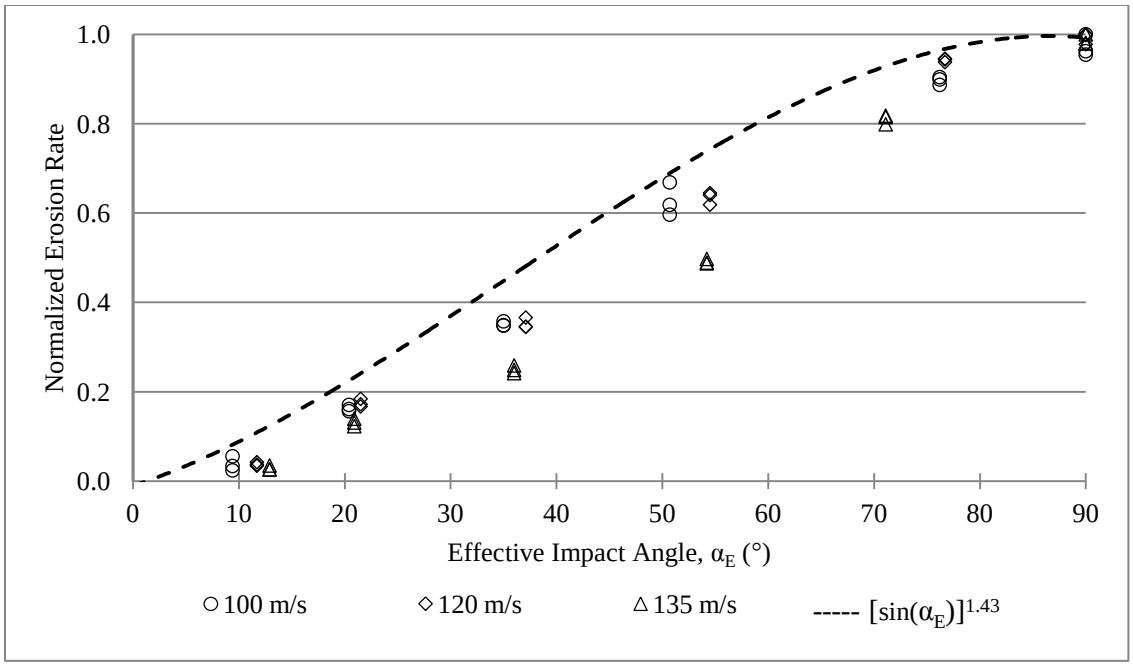

Figure 5-9: Normalized erosion rate vs. effective impact angle for three different constant total velocities i.e., 100, 120, and 135 m/s for 50 µm alumina. A sine function indicates the expected behaviour were the normalized erosion rate to depend only on the normal component of velocity.

Figure 5-10 shows logarithmic plots of the erosion rate as a function of the normal component of velocity for the same data as was plotted in Figure 5-8. At a certain velocity, the slope of the curve suddenly became steeper. This bilinear behavior indicated the existence of a critical threshold of relative-normal velocity (the corresponding normal velocity where two lines meet). When this threshold is reached, the slope of the erosion rate curve will be increased, and more erosion will occur. Each data point in the curve has a corresponding impact angle (10, 20, 35, 55, 75, and 90º respectively for 6 points). It was also seen from figure 5-10 that at a fixed velocity, the shift of the erosion rate from the first line, stage I, to the second line, stage II, occurs after third data point which corresponds to an impact angle of 35°. This is consistent with the data of Ballout et al. [23] who found this angle to be 30°. This small deviation was probably because they have used 142 µm alumina compared to 50 µm alumina used in this study.

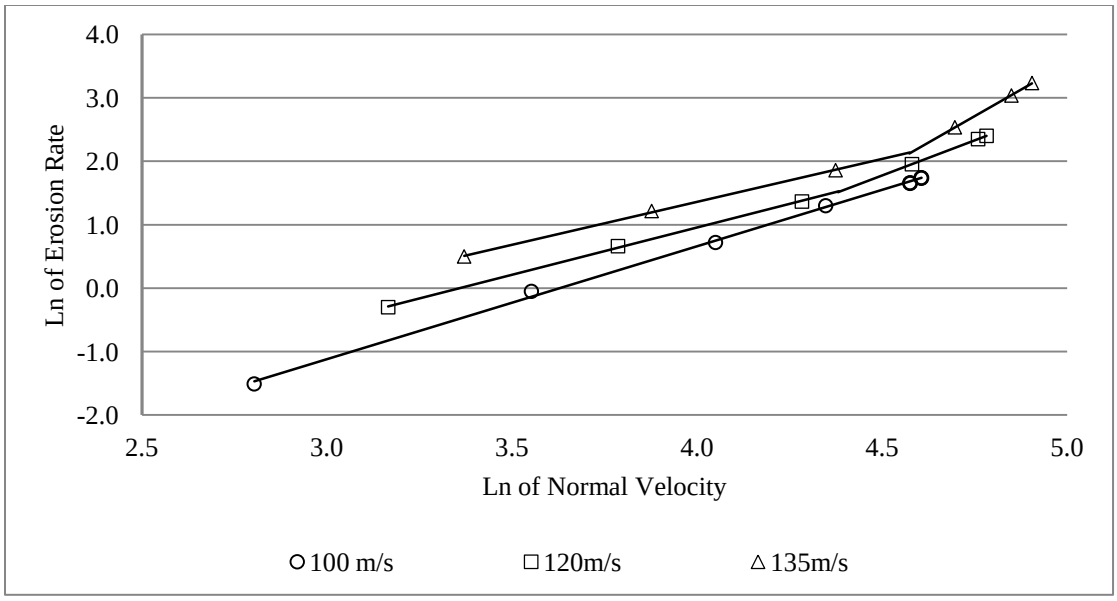

Figure 5-10: Logarithmic plots of erosion rate (mg/g) vs. normal velocity (m/s) at fixed total velocities and increasing impact angles between 10° and 90°.

Ballout et al. [23] found that the first stage of the erosion had a smaller slope than the second stage. They also investigated the erosion mechanism of glass impacted by sharp alumina particles using scanning electron microscope (SEM) [23]. Their SEM images showed that the size of the damage zone increased as the impact angle increased. Moreover, the shape of the damage zone for 15° and 30° impact angles was in one direction relative to the original impact site, while for 45° and 90° the zone was larger and more uniformly distributed around the original impact site (Figure 5-4). As the lateral cracks advanced parallel to the surface they also propagate upward toward the surface causing chipping and material removal. This observation indicated that the direction and extent of the crack propagation from the crack initiation site depended on the impact angle [23].

The importance of the tangential velocity of the particles in determining the bilinear behavior can be shown by conducting a special test on the rotating disc. The rotational speed of the disc was determined and set in such a way that the relative effect of the tangential velocity of the particles was eliminated. A comparison of the results of this zero relative tangential velocity test was compared with the logarithmic plot for erosion rate versus normal velocity bilinear plot

of 120 m/s constant total velocity, which is presented in Figure 5-11. It is shown that the logarithmic erosion rate for glass with the eliminated particle tangential velocity follows a linear path. Furthermore, for larger impact angles, the erosion rates for zero tangential velocity tests are close to those in stage II for the 120 m/s constant total velocity test. However, as the impact angle decreased, the erosion rates of zero tangential velocity test became progressively smaller than they are in stage I for the 120 m/s constant total velocity test (presence of tangential velocity) This shows that, even though the measured erosion rate values in stage II are larger than those of stage I, the erosion process is relatively more efficient in stage I. This also indicates that the bilinear behavior of the logarithmic erosion rate is related to the importance of the tangential velocity at low impact angles [23].

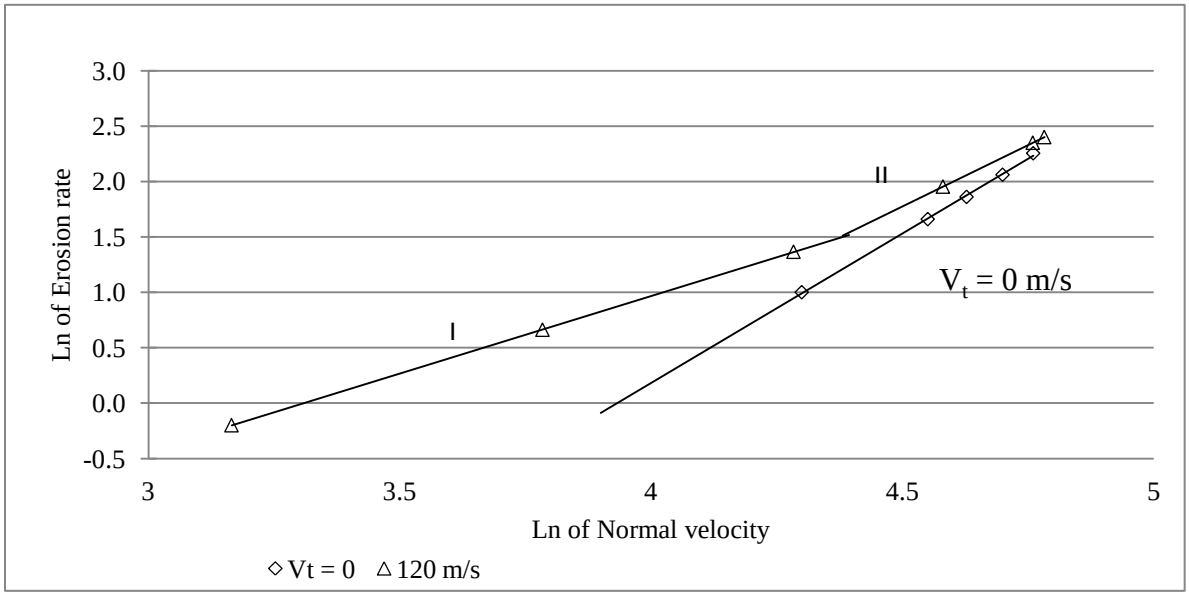

Figure 5-11: Comparison plots of the logarithmic erosion rate (mg/g) vs. normal velocity (m/s) with a zero tangential velocity experiments.

The difference between the two stages might be attributed to the mechanism of lateral crack propagation [23]. In the first stage the lateral crack propagated in the direction of the tangential velocity thus causing concentrated damage. However, in the second stage, the tangential impact forces were weaker and the normal forces of impact were stronger, therefore,

the lateral cracks are diffused around the impact site, and are relatively less concentrated, thus causing a less effective erosion process (Figure 5-4).

Figure 5-12 shows that at a fixed angle of impact, the logarithm of erosion rate versus logarithm of the normal component of velocity plots as a straight line. Despite this, consistent with earlier results, the graph also clearly shows that the erosion rate does not uniquely depend on the normal component of velocity.

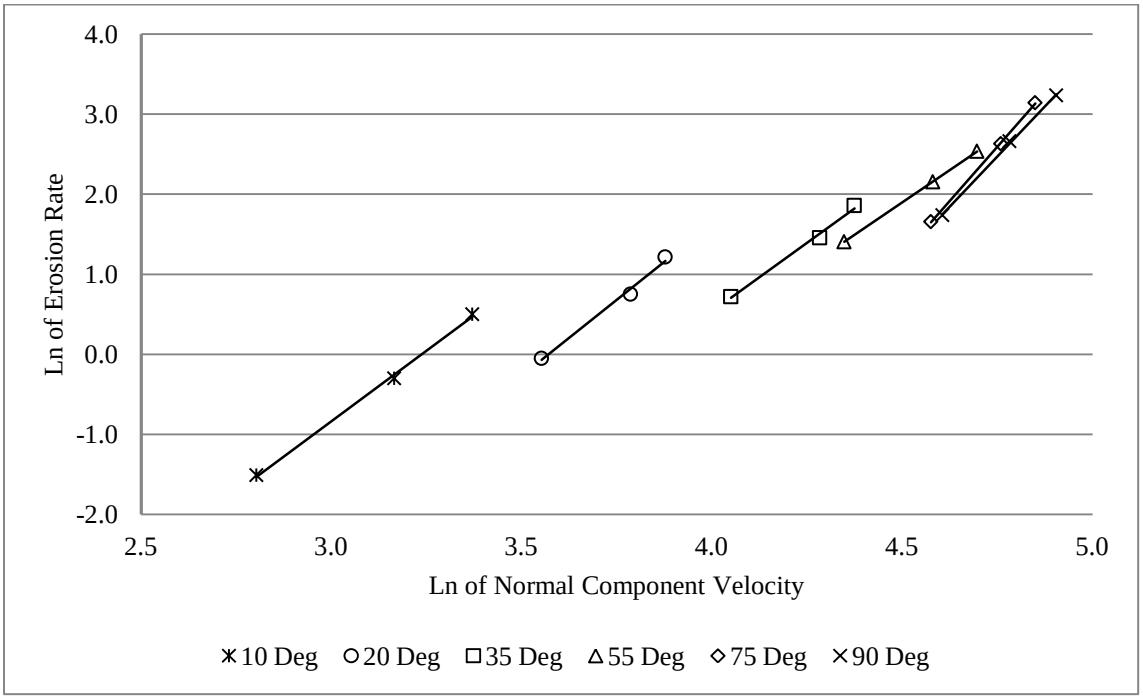

Figure 5-12: Logarithmic plots of erosion rate (mg/g) vs. normal velocity (m/s) at fixed impact angles with an increasing velocity ranging from 100-135 m/s.

5.3 Velocity Exponent

The erosion rate of materials has a power law dependency on the particle impact velocity at normal incidence [1-5, 39-41]. The velocity exponent is a strong function of impact velocity and size, and the mechanical properties of the substrate and particles [67]. Previously, under the assumption that the erosion rate depends only on the normal component of velocity, Ghobeity et al. [1] determined the velocity exponents experimentally by measuring the erosion rate at a constant velocity and varying the impact angle. They plotted the normalized erosion rate as a

function of normal velocity, and found a velocity exponent value of 1.43, which was very low compared to the other researchers [2-5, 39-41]. In is noted, however, that the test of Ghobeity et al. involved varying the impact angle so that each data point involved a different tangential velocity. In contrast, the present rotary disc apparatus was used to determine velocity exponent without changing the blasting pressure, while keeping the tangential velocity zero. This was accomplished by varying the angle of attack of the nozzle, while simultaneously adjusting the rotational speed of the disc in order to cancel out the tangential velocity component. This methodology effectively allows a wide variety of impact velocities (at effectively normal impact) to be attained while using a single (or at least limited) blasting pressure (i.e., particle velocity). This is of great convenience because of the difficulty in measuring particle velocities at different blasting pressures.

The velocity exponent experiments were performed for borosilicate glass using 25 μm and 50 μm alumina particles at a fixed blasting pressure of 200 and 300 kPa. The experimental parameters for these velocity exponent experiments can be found in Table 5-12, and 5-13. Then erosion rates were plotted as a function of normal velocity in Figure 5-13 and, although the number of data points was limited, a power relationship gave a very good least squares fit to the data points (R^2= 0.99 for both particle sizes).

Table 5-12: Experimental parameters for velocity exponent at effective normal impact for 25 μm alumina particles.

Disc Speed (rpm)	Impact Angle (°)	Tangential Velocity (m/s)	Normal Velocity (m/s)	Total Velocity (m/s)	Effective Impact angle (°)	Blasting Pressure (kPa)
770	93	0.0	138.2	138.2	90	300
2040	98	0.0	137.1	137.1	90	300
4045	106	0.0	133.0	133.0	90	300
7110	119	0.0	121.0	121.0	90	300

Table 5-13: Experimental parameters for velocity exponent at effective normal impact for 50 µm alumina particles.

Disc Speed (rpm)	Impact Angle (°)	Tangential Velocity (m/s)	Normal Velocity (m/s)	Total Velocity (m/s)	Effective Impact angle (°)	Blasting Pressure (kPa)
650	93	0.0	116.8	116.8	90.0	200
4240	110	0.0	109.9	109.9	90.0	200
6010	119	0.0	102.3	102.3	90.0	200
7285	126	0.0	94.7	94.7	90.0	200

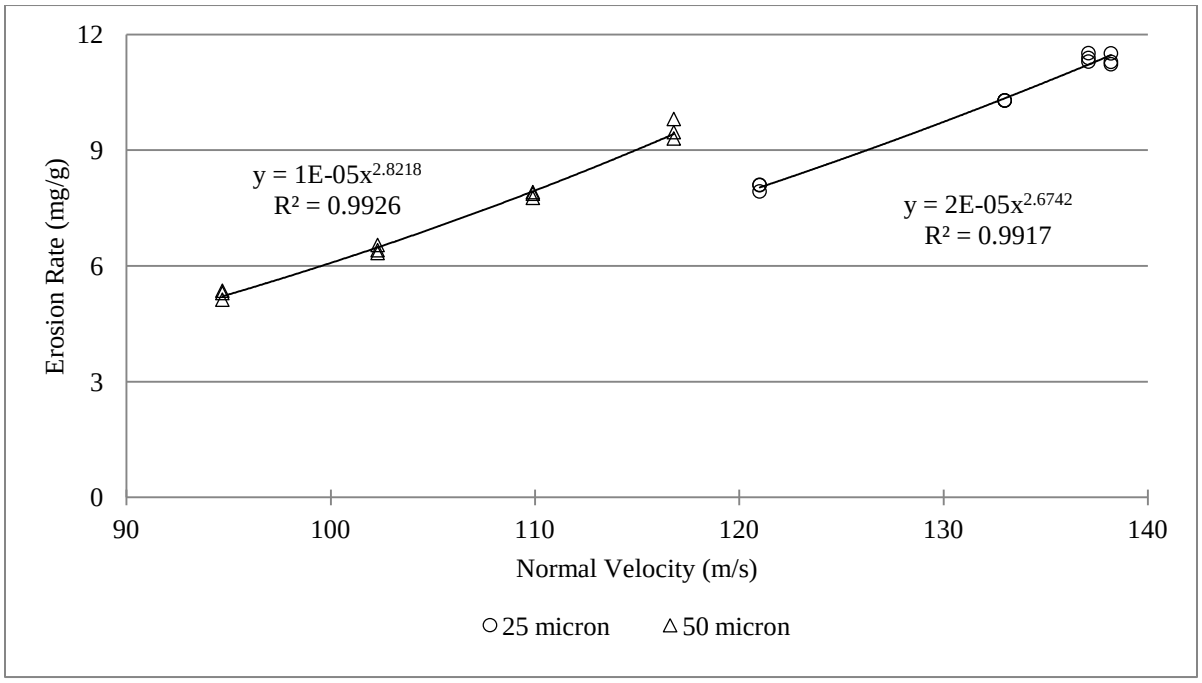

Figure 5-13: Erosion rate vs. total velocity for borosilicate glass at effective normal impact using 25 and 50 µm alumina particles.

The velocity exponent was found to be 2.67 for 25 µm alumina, and 2.82 for 50 µm alumina; which was almost double than the velocity exponent 1.43 found by Ghobeity et al. [1] for the 25 µm alumina blasted towards borosilicate glass target. However, the velocity exponents found here compare very well to the values of 2.46 found by Slikkerveer et al. [2, 3]. Wensink et

al. [5], and Buijs and Pasmans [41] also mentioned that the velocity exponent to be 2.3 for glass. Feng and Ball [39] also found a velocity exponent close to 2 for glass impacted by angular particles. Verspui [40] indicated that the experimental velocity exponent was 3.86 for glass impacted by angular alumina. So from the literature survey of velocity exponent, it can be concluded that the found velocity exponent was valid for borosilicate glass and alumina particle system.

The surface evolution models for the abrasive jet micro-machining of glass [1, 2, 5, 19] assumed that the relationship between erosion and speed of local surface evolution depends simply on the normal component of velocity raised to a velocity exponent that is in the neighbourhood of 1.4-1.5 (normalized erosion would follow simply the sine curve shown in Figure 5-9). The velocity exponents found here are almost double than that of Ghobeity et al. [1], although the measurement methods were different. They have neglected the effect of tangential velocity component during velocity exponent measurements, the main reason for their finding a lower velocity exponent. The results indicated that the tangential component of velocity effect is not negligible, and should be included in surface evolution modelling to improve the prediction of the feature shape machined using abrasive jet micro-machining. However, Figure 5-9 shows that the tangential velocity effect is not large, unless high incident velocities are used. This is an excellent topic for future research in this area.

Chapter 6: Conclusions and Recommendations

6.1 Summary

A mechanically powered wheel blaster system consisting of a particle feeding mechanism, particle acceleration mechanism, and vacuum chamber, was designed and constructed. The vacuum chamber was constructed using 1.27 cm thick polycarbonate sheets and sealing it from all edges. A vacuum pressure pump was used to evacuate the chamber. The particle feeding mechanism was constructed with a linear actuator and a two-tube power feeding device. The particle launching mechanism was constructed with a speed controllable AC motor which rotated a cogwheel made of rigid HDPE sheet. There was a belt and pulley system designed in between the motor and cogwheel to increase the rotational speed of the cogwheel. The rotary cogwheel was supposed to launch the abrasive particles falling from the abrasive feeder when they come in contact. After determining the launched particle trajectory the sample could be placed for micro-machining. Although the rotating mechanism and particle feeding mechanism worked, they system failed due to the presence of air inside the chamber.

The failure of the implemented design occurred due to the fact that only 78 kPa (77%) vacuum was achieved with the chamber, while the required vacuum for this type of test was ultrahigh vacuum (99.99%). The design could not attain the desired vacuum because of the leakage from rotary sealing in the motor shaft and sealing at the linear actuator. Due to the presence of air, particles could not come in contact with the rotary cogwheel, but were blown away by the air movement generated by the rotating wheel. It was concluded that this type of erosion tester is impossible to practically use without an ultrahigh vacuum chamber. Instead, the designed mechanism was adapted to rotate a target holder disc which was blasted using a traditional air blast system.

The effect of tangential velocity on borosilicate glass impacted by granular alumina particles (25-150 μm) using a rotary disc target holder, was investigated. This was done by machining channels on the mounted glass samples with an abrasive jet and measuring the volume loss using a profilometer. The erosion rate dependence on the tangential velocity was established, in contrast to long held assumptions in the literature. The velocity exponent for borosilicate glass and alumina particle system was also determined.

6.2 Conclusions & Contributions

To the knowledge of the author, this was the first time a relative change in erosion rate magnitude due to only tangential component of velocity change, while keeping the normal velocity constant, was measured. Moreover, experiments of this type, i.e., to determine the role of tangential velocity on erosion rate, had never before been attempted using an erosive system typical of that used in abrasive jet micro-machining applications. The main conclusion of the research was that the tangential velocity cannot be neglected in the micro-machining of borosilicate glass. The other important findings and contributions can be summarized as follows:

- A rotary disc target holder was constructed. This new technique appears be a powerful tool to investigate the solid particle erosion mechanisms, especially those related to normal and tangential velocities. The rotating disc movement allows the reduction or increase of the relative particle tangential velocity. The system enables separate investigation of the effect of the normal and tangential particle velocity components on the resulting erosion rates and mechanisms.
- Erosion rate on borosilicate glass as a function of tangential velocity at three different constant normal velocities i.e., 75, 102, and 121 m/s for 50 µm alumina particles were measured. As expected, the higher constant normal velocity caused a higher erosion rate. It was also found that there was a significant increase in erosion rate (55% for 75 m/s, 13% for 102 m/s, and 44% for 121 m/s) due to a tangential velocity increase of 93 m/s, although the normal velocity was constant. At a same constant normal velocity, the unidirectional behaviour of the tangential velocity caused relatively larger pieces of target material to be chipped than the same normal impact velocity with zero tangential.
- The erosion rate at different tangential velocities was measured experimentally for three different alumina particle sizes i.e., 50, 100, and 150 µm at 75 m/s constant normal velocity. As expected, the erosion rate increased with increasing particle size. Furthermore, the magnitude of the change in erosion rate with increasing tangential velocity was found to be greatest for smaller particles (55% for 50 µm, 36% for 100 µm, and 43% for 150 µm due to a tangential velocity increase of 93 m/s).
- The erosion rate as a function of impact angle for three different constant total velocities i.e., 100, 120, and 135 m/s was determined and it was found that, as expected, the

maximum erosion rate occurred at normal impact, and the magnitude of erosion rate increased with the impact velocity. However, the normalized erosion rate was found to depend slightly on the impact velocity. Moreover, logarithmic plots for erosion rate and normal velocity showed a bilinear phenomenon, which were due to the tangential velocity dominance at shallower impact angles. It was shown that at shallower impact angles, the erosion process was more efficient with the presence of tangential velocity.

- In the modeling of the surface evolution of abrasive jet micro-machined features in brittle materials, it is commonly assumed that dependence of normalized erosion rate on angle of attack should depend only on the normal component of velocity. This was proven to be only approximately true. Therefore future refined models of surface evolution should also take into account the tangential component of velocity since that also affects the erosion rate.
- The velocity exponent was found to be 2.67 and 2.82 for 25 and 50 µm alumina particles, respectively. The experimentally found velocity exponent for borosilicate glass and alumina system was in a good agreement with the velocity exponent found by other researchers for similar erosive systems [2-5, 39, 40]. Although the velocity exponent was almost double than the velocity exponent found by Ghobeity et al. [1] for the same system, the measurement technique was different as Ghobeity et al. ignored the effect of tangential velocity.
- The average roughness and RMS roughness was plotted against tangential velocity using 50 µm alumina for two constant normal velocities i.e., 75 and 121 m/s. Although roughness increased with a normal velocity increase from 75 to 121 m/s (within 2-3µm), there was no apparent correlation with a tangential velocity increase of 93 m/s. Also the roughness increases with particle size; it again did not show a correlation with the tangential velocity. Using 50 and 100 µm particle size the average roughness was within 2-3 µm, while having 4-6 µm when 150 µm particles were used. It can thus be concluded that the surface roughness was independent of tangential velocity component, and depended solely on the normal component of the kinetic energy.

6.3 Recommendations for Future Work

With the new apparatus constructed, many aspects of this research can be investigated further:

- The mechanically powered erosion tester can be improved by designing a centrifugal type erosion tester similar to Ref. [4-8]. A professionally built vacuum chamber, with rotary and linear feedthrough for the motor and actuator, is recommended for this ultrahigh vacuum requirement, although such chambers are very expensive.
- The primary source of leakage in the mechanically powered erosion tester was the rotary shaft inlet into the chamber. This might be solved in the future using a magnetic shaft coupler, although it is an expensive alternative.
- The rotating target apparatus should be modified in order to achieve higher tangential velocities, by either changing the motor or increasing the disc diameter. This would allow the investigation of erosion mechanisms at very low impact angles, and determination of the velocity exponent using a wider range of particle velocities. The effect of tangential velocity on other brittle materials can be investigated using various particle types.
- Ductile materials give maximum erosion at a shallow impact angles. At a shallower impact angle, the abrasive jet spreads over a larger area of the substrate, causing a large range of local impact angle. But using this apparatus it was possible to lower the effective impact angle by even half of the actual (geometric) impact angle. So, more erosion data at shallower impact angles can be determined using this apparatus without causing a large variation in local impact angles.

Appendices

A. Earlier Designs of the Mechanically Powered Erosion Tester

The vacuum chamber was made of aluminum 6061-T6 alloy and 1018 cold rolled steel. Dimensions of the assembled device were height 99 cm, width 30.5 cm, length 63.5 cm. The general principle of the device was acceleration of abrasive particles towards a target in a vacuum chamber. The mechanism was consisted of an aluminum blade rotating at high speed (depending on the motor rpm). The rotating blade needed to be well balanced because it was going to rotate at a very high speed. It also required high speed bearings for the rotating shaft. The tips of the blade accelerated the particles by hitting a pile of abrasive located just below the blade. It was assumed that the particles impacting the tips of the blade have the same speed of the tangential velocity of the tip due to rotation. The motor was kept outside the chamber to allow for adequate cooling and to protect it from abrasive particles.

The abrasive powder was pushed up through an aluminum pipe by an actuator at controlled rate. The chamber had a linear feed through opening at the bottom plate for actuator. There was also place for linear stage for target holder. Figure A-1 shows the major parts and components of the initial design. Two windows at front and top of the chamber would provide visibility of the accelerated particles path and allow imaging. The initial plan was to create a vacuum environment using a venturi vacuum pump (model RK-78165-20, KNF Neuberger Inc., Trenton, NJ, USA) attached to the chamber. Theoretical maximum vacuum attainable with the venturi device was 95 kPa below atmospheric pressure. There was a pressurized air source (550 kPa) required for venturi pump operation. Sealing of the vacuum chamber against outside pressure was planned to be done using oil seal and gaskets.

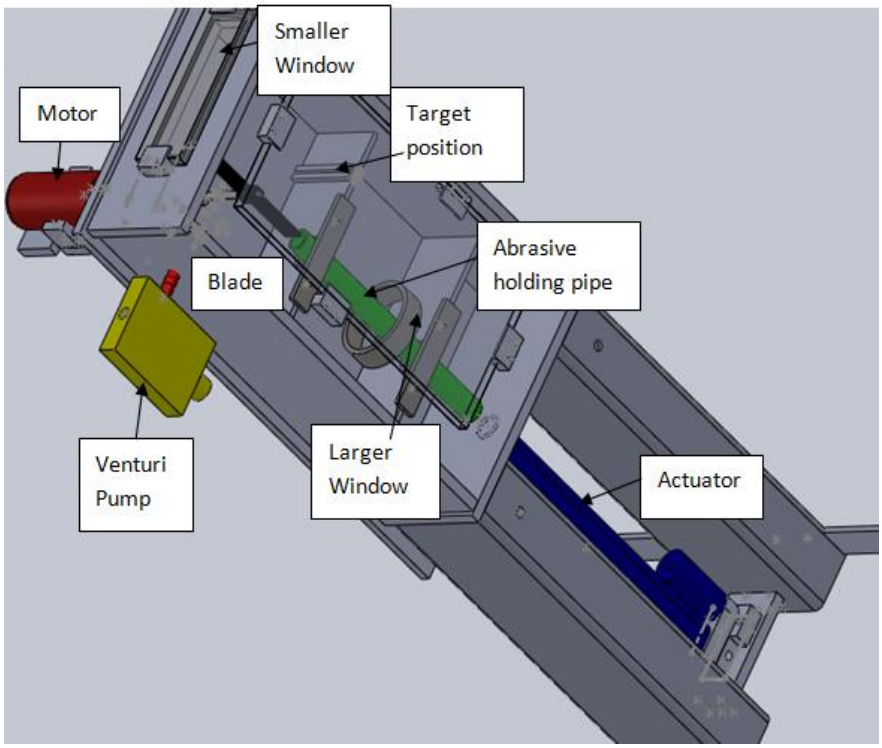

Figure A-1: Initial design of the vacuum chamber and particle acceleration mechanism.

A prototype was built and tested in order to determine if the mechanism could produce sufficiently high particle speeds to allow machining. The motor mounting platform, steel shaft connecting the motor and the blade, aluminum blade, abrasive holding pipe, steel base plate for actuator inlet were manufactured. A Jobmate rotary tool kit (model 54-4778-8, Canadian Tire Corp., Canada) was used as a motor and a 30.5 cm stroke actuator from Firgelli Automations Inc. was used initially. The mechanism worked but the resulting rotational speed was found to be too low to allow for machining. There was a need to find a reliable and high speed motor. A brushed 14.4V DC hobby motor Monster truck (model 57900, LRP Electronic GmbH, Schorndorf, Germany) was used to rotate the blade. However, the brushed DC motor could not handle the resisting torque of the bearings. Finally the Dayton AC/DC 1HP motor was selected and used as AC motor to eliminate the need for a power supply. The maximum no load rpm for the motor was 10,000 rpm and speed could be changed via a speed controller.

The second design utilized a belt and pulley system to increase the speed about 3.5 times. The larger pulley was attached to the motor shaft with a shaft coupling and the smaller pulley was attached with the main shaft. The main shaft was kept shorter to minimise the vibration, using two bearing holders which were attached to the wall. The size of the side viewing window was also increased. Figure A-2 shows the apparatus after these modifications to the initial design. There was also a plan for an aluminum propeller design. After testing if aluminum was eroded quickly by the abrasive particle impacts, it was possible to design a propeller with replaceable tip which came in contact with the abrasive. The replaceable tip could be made of some other erosion resistant material i.e., nylon, HDPE.

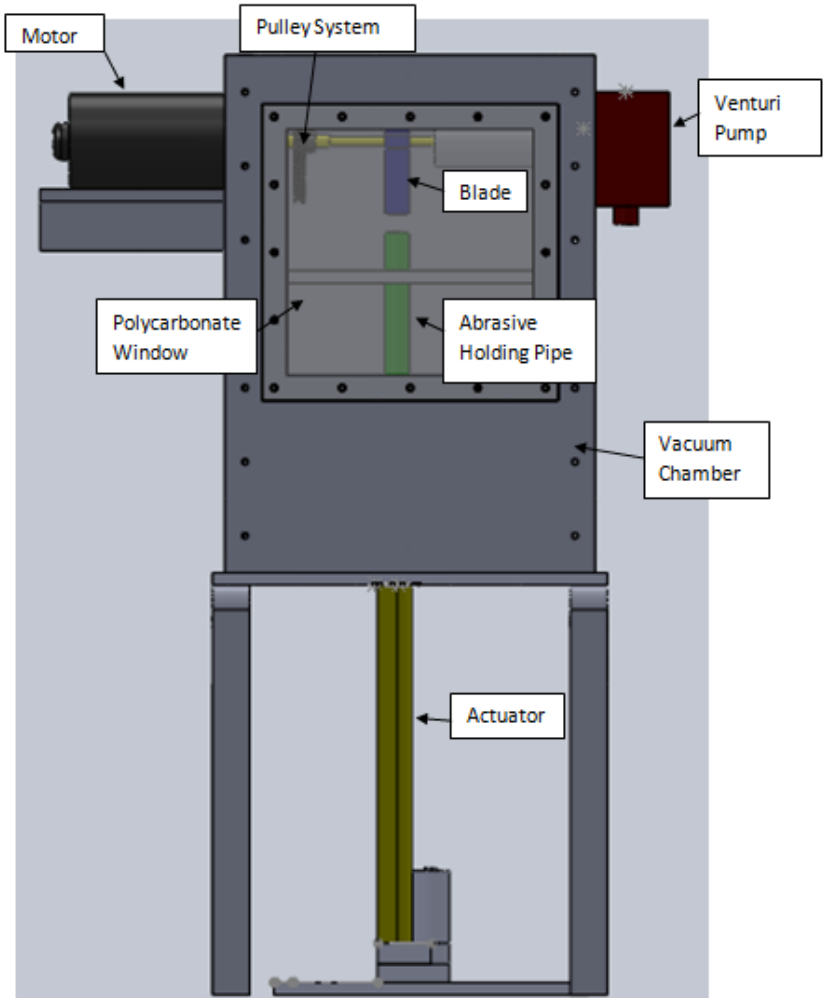

Figure A-2: Modified design of the vacuum chamber.

Ultimately, rather than using an aluminum blade to accelerate the abrasives, a very thin disc with cogs was chosen instead, because it was thought that the 1.27 cm wide aluminum blade might cause too much aerodynamic resistance. Initially, it was thought that an 18.4 cm diameter and 0.16 cm thick carbide tipped steel saw blade could be used as a disc. However, this was found to be too heavy and to reduce the motor load, the high density polyethylene (HDPE) was selected as a disc material. The HDPE disc had 19.1 cm diameter and 0.32 cm thickness and was cut using a water jet cutter. The HDPE disc weighted only 97.8 grams compared to the steel blade which weighted 331.9 grams. The HDPE disc also had twice the thickness of the steel blade, which means it could launch more powder than the steel blade.

The actuator orientation was also changed in the assembly. Previously, the actuator pushed the abrasive vertically. In the modified design, the actuator and the abrasive holding pipe were placed horizontally in order to reduce the friction inside the pipe.

The aluminum 6061-T6 alloy housing box, disc, and motor mounting assembly were manufactured to test the mechanism. The polycarbonate enclosure was then built and the vacuum pressure pump CPS-8B was selected. Primarily, the chamber was sealed by Permatex (form-a-gasket) sealant pouring the inner surfaces of the chamber. The sealant did not work well as it could achieve only about 17 kPa vacuums. The edges were then sealed using buna-N rubber seals with an adhesive backing. The corners were also sealed with the Permatex sealants and silicon sealants. After sealing the chamber with rubber seals, about 78 kPa vacuums was achieved. The main leakage was investigated to be from the rotary shaft inlet from the motor side. This problem could be solved using a magnetic rotary seal for shaft.

Appendix B: Stresses Analysis of the Rotating Disc

There were two types of stress on a rotating disc, the tangential stress and the radial stress [68]:

$$\text{Tangential stress, } \sigma_t = \rho\omega^2 \left(\frac{3+\nu}{8}\right)\left[r_i^2 + r_o^2 + \frac{r_i^2 r_o^2}{r^2} - \left(\frac{1+3\nu}{3+\nu}\right) r^2\right] \qquad \text{(B-1)}$$

$$\text{Radial stress, } \sigma_r = \rho\omega^2 \left(\frac{3+\nu}{8}\right)\left(r_i^2 + r_o^2 - \frac{r_i^2 r_o^2}{r^2} - r^2\right) \qquad \text{(B-2)}$$

where, ρ = mass density, ω = angular velocity (in rad/s), v = Poisson's ratio, r_i= inner radius of the disc, r_o= outer radius of the disc, r = radial location of interest where the stress needs to be measured.

For the HDPE disc,

Density, ρ = 0.95 g/cm^3 = 950 kg/m^3

Poisson's ratio, v = 0.40

Yield strength, σ_Y = 29.5 MPa

Assuming, ω = 15,000 rpm = 1,571 rad/s

Outer radius of the disc, r_o= 0.0953 m

Inner radius of the disc, r_i= 0.00794 m

The equations are plotted in Figure B-1 to determine the variation of the stresses along the radius of the disc.

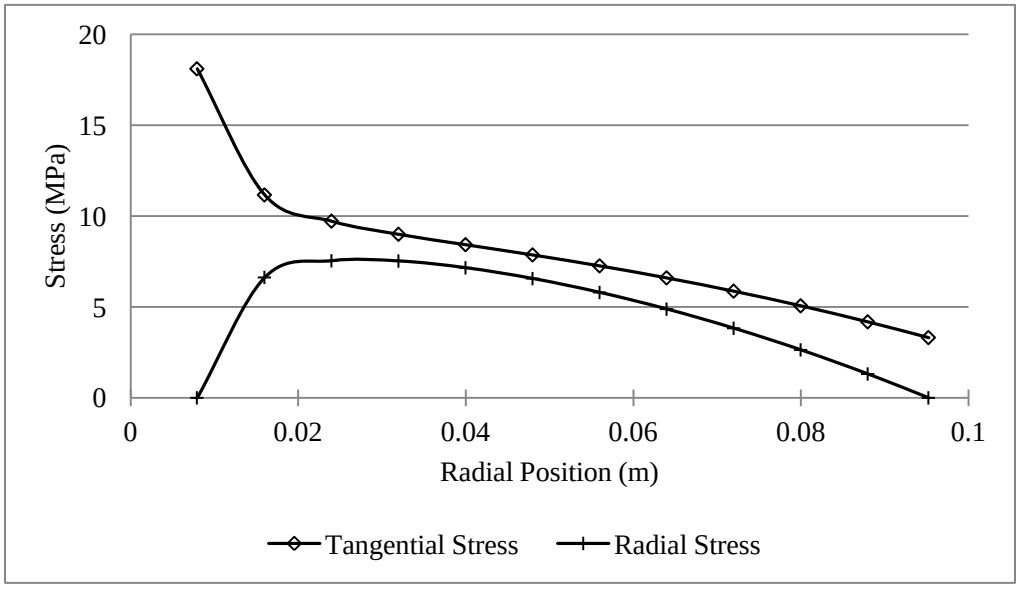

Figure B-1: Stresses in the HDPE rotary disc along the radial position.

Figure B-1 shows that the tangential stress was the maximum at the inner radius where the radial stress was the minimum. The tangential stress decreased monotonically with an increase in radial distance. The maximum total stress was at the inner diameter of the disc which was covered with flanges. The Von Mises stress was found to be 18.1 MPa, which was then compared with the yield strength for HDPE 29.5 Mpa. Applying a factor of safety 1.5 and using Von Mises yield criterion for ductile materials the disc was safe. Thus, there was no chance of failure within the specified range of velocity.

Appendix C: Vacuum Chamber Calculations

C.1: Stress and Deflection Calculations in Polycarbonate Plates

The polycarbonate plates were assumed as rectangular flat plates with uniform loading and edges clamped (Figure C-1). The equations for this type of problems are [69]:

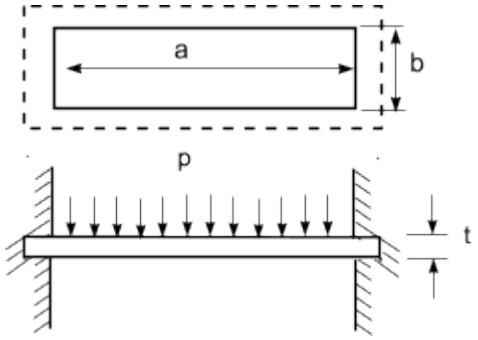

Figure C-1: Rectangular flat plate, uniform load, edge clamped [69].

$$\sigma_m = \frac{pb^2}{2t^2\,[0.623(\frac{b}{a})^6+1]} \tag{C-1}$$

$$y_m = \frac{0.0284\,pb^4}{Et^3\,[1.056(\frac{b}{a})^5+1]} \tag{C-2}$$

where, p = uniform compressive surface pressure on plates = 1atm = 101 kPa,

b = supported width of the plate,

a = longer length of the plate,

t = thickness of the plate = 1.27 cm,

E = Young's modulus of elasticity = 2.0 GPa (for polycarbonate sheet)

(i) For, motor and pump side walls, a = 61 cm and b = 35.6 cm

Thus, the maximum stress at the mid edge of the plate: σ_m = 38.6 Mpa

The maximum deflection at the centre: y_m = 1 cm

(ii) For, top and base walls, a = 61 cm and b = 30.5 cm

σ_m = 29.0 MPa and y_m = 0.6 cm

(iii) For, Actuator side and back walls, a = 35.6 cm and b = 30.5 cm

σ_m = 23.4 MPa and y_m = 0.4 cm

From the above calculation, the maximum deflection on the pump and motor side walls were 1 cm each, i.e., the outside pressure pressed the longer walls inward direction. The motor shaft and the rotary sealing were displaced due to deflection. It was thus confirmed that some type of reinforcement was necessary for the longer walls of the chamber. Hard fibre bars available in the lab were placed along the longer walls for reinforcement of the walls. A permanent reinforcement could have been made by making ribs in the longer walls.

C.2: Pump-Down Time

For constant speed pumps on system with low leakage and low outgassing, the relation between time and pressure is [70]:

$$t = 2.3\frac{V}{S} ln \frac{p_1}{p_2} \quad \text{(C-3)}$$

where, t = evacuation time (s), V = enclosed evacuated volume (m^3), S = volume flow rate capacity of the vacuum pump (m^3/s), p_1 = initialization pressure (kPa), p_2 = final vacuum pressure (kPa)

Since the system was found to have leakage, this calculation was merely a theoretical approach and it did not have any relation with the actual pump down-time.

For the particular scenario, V = 0.61 x 0.356 x 0.305 = 0.066 m^3,

S = 8 CFM = 0.0038 m^3/s, p_1 = 101 kPa, p_2 = 1 kPa (assuming 99% vacuum)

So, t = 185.4 s or 3 minutes and 5 seconds.

Appendix D: Radial Motion Effect of the Rotary Disc Target Holder

During the tests using rotary disc target holder, there was radial velocity of the abrasive particles acting toward the centre of the disc generated by the centripetal acceleration. The radial motion was ignored during the erosion rate calculations. In this section, the effect of the radial motion is analysed following the work of Talia et al. [24].

Alumina Particle: Young's modulus, E_1 = 379 GPa

Poisson's Ratio, v_1 = 0.25

Mean Diameter, R = 25 μm to 150 μm

Mass, m = volume x density

= (4/3 πR^3) (4000 kg/m^3) = (1.6755 x 10^{-14}) R^3 (R in μm)

Borosilicate Glass Sample: Young's modulus, E_2 = 64 GPa [62]

Poisson's Ratio, $v_2 = 0.20$

Material and geometry dependent generalized parameter (K) for sphere on half-space contact was:

$$K = 0.424(R / (h_1 + h_2))^{1/2} \quad \text{(D-1)}$$

$$\text{where, } h_1 = 1- [v_1^2 / (\pi E_1)] = 0.7874 \text{ x } 10^{-12} \quad \text{(D-2)}$$

$$h_2 = 1- [v_2^2 / (\pi E_2)] = 4.775 \text{ x } 10^{-12} \quad \text{(D-3)}$$

$$\text{then, } K = 77.8 \text{ x } 10^9 (R)^{1/2} \text{ N/(m)}^{1/2}$$

The maximum indentation at the end of compression phase δ_m, for a particle initial normal velocity $V_0 = 50$ m/s, yields:

$$\delta_m = (2.5*m*V_0^2/ 2*K)^{2.5} = 0.0498\ R \quad \text{(D-4)}$$

$$\text{Then the maximum force becomes: } f_m = K\delta_m^{1.5} = \text{o.865 x } 10^9\ R^2 \quad \text{(D-5)}$$

$$\text{To estimate the particle-sample contact period: } D_t = 2.94\ \delta_m/ V_o = 2.93 \text{ x } 10^{-3}\ R \quad \text{(D-6)}$$

Evaluating D_t for the largest and the smallest particle size R yields: for $R = 25$ μm, $D_t = 0.07$ μs and for $R = 150$ μm, $D_t = 0.44$ μs. So, for two extreme values of particle size the total contact periods are very small. The acceleration vector of the particle on impact can be written as follows:

$$\boldsymbol{a_p} = -\boldsymbol{\omega}^2\boldsymbol{r} + 2\boldsymbol{\omega} \text{ X } \boldsymbol{V_{rt}} + \boldsymbol{a_{rel}} \quad \text{(D-7)}$$

The first term represents acceleration of the sample, the second term represents the Coriolis acceleration of the particle, and the last term is the relative apparent acceleration of the particle with respect to the rotating sample which was zero. When the motor speed was 4000 rpm = 419 rad/s, and the radial distance of the sample $r = 0.09$ m, and $V_{rt} = 100$ m/s: $a_p = 68 \text{ x } 10^3$ m/s^2. Finally the radial nominal motion of the particle could be evaluated as follows: For 25 μm particles, $D_s = 1/2a_p(D_t)^2 = 0.015$ μm, then the average radial velocity of the erodent particles was: $V_r = D_s/D_t = 0.21$ m/s. Again for 150 μm particles, $D_s = 1/2a_p(D_t)^2 = 0.37$ μm, then the

average radial velocity of the erodent particles was: $V_r = D_s/D_t = 0.84$ m/s. So, from the above analysis is was obvious that the radial velocity of the particle was very small and negligible compared to the tangential velocity component.

Appendix E: Erosion Rate Using Gravimetric Method

As discussed in Section 4.3.2, the erosion rates were measured using two methods: volumetric and gravimetric. The results shown in Chapter 4 and 5 were on the basis of volumetric measurement using profilometer. The gravimetric results are reported in this section. Experimental parameters were the same for both methods except erosion rate measurement techniques. The scatter plot (Figure E-1) shows the difference between two erosion rate measurement methods. As discussed in Section 4.5, the gravimetric measurement over estimated erosion rate by 6.9%.

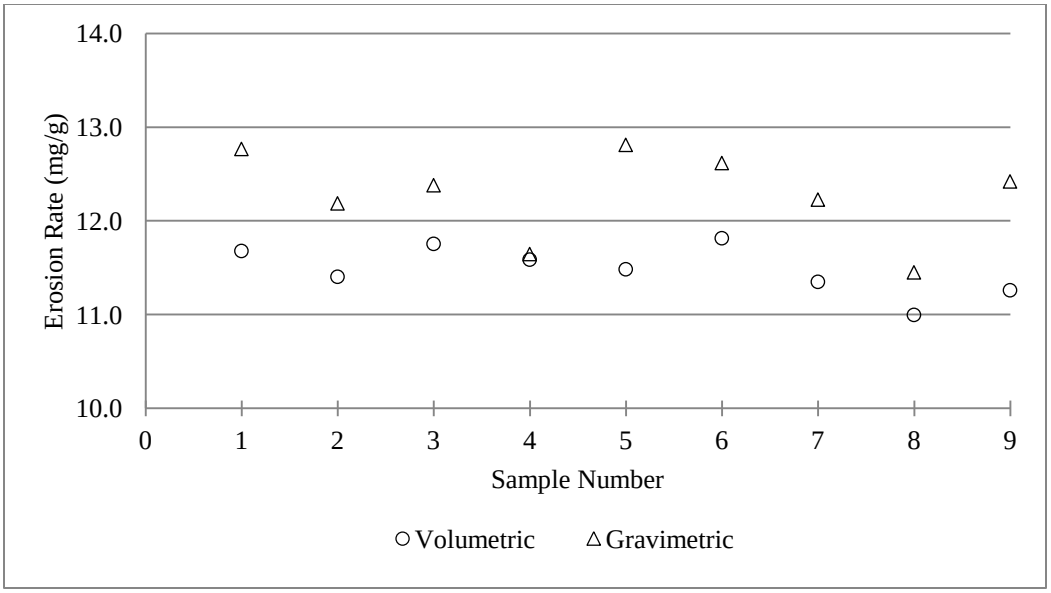

Figure E-1: Scatter plot to show the difference between two erosion rate measurement methods: volumetric and gravimetric.

Figure E-2 shows a plot for erosion rate of borosilicate glass as a function of tangential velocity at three different constant normal velocities i.e., 75, 102, 121 m/s for 50 μm alumina particles. The experimental parameters for this plot were given in Tables 5-1 to 5-4, and this plot is comparable with Figure 5-1.

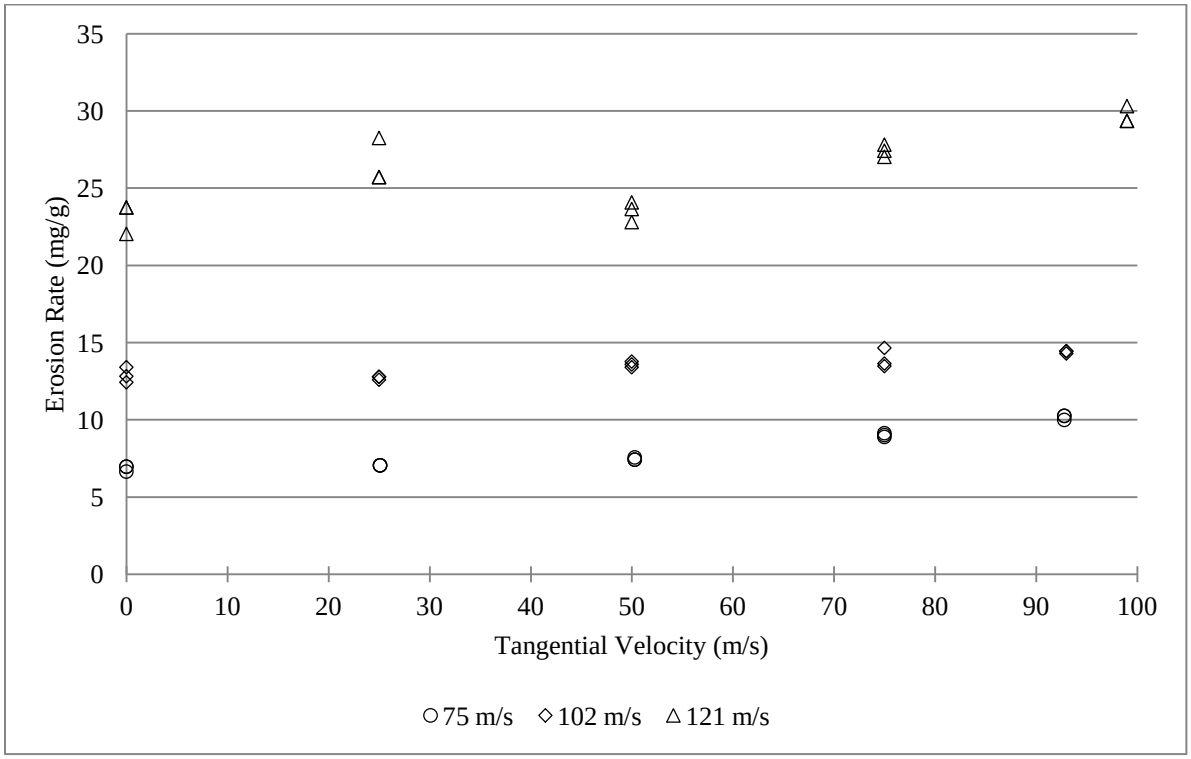

Figure E-2: Mass loss measurements of erosion rate vs. tangential velocity for borosilicate glass impacted by 50μm alumina particles at constant normal velocities of 75, 102, and 121 m/s.

Figure E-3 shows a plot for erosion rate of borosilicate glass as a function of tangential velocity for three different particle sizes i.e., 50, 100, and 150 μm at 75 m/s constant normal velocity. The experimental parameters for this plot were given in Tables 5-2, and 5-5 to 5-7; and this plot is comparable with Figure 5-5.

Figure E-4 shows a plot of impact angle dependence erosion rate of borosilicate glass for three different constant total velocities i.e., 100, 120, and 135 m/s. The experimental parameters for this plot were given in Tables 5-8 to 5-11; and this plot is similar to Figure 5-8.

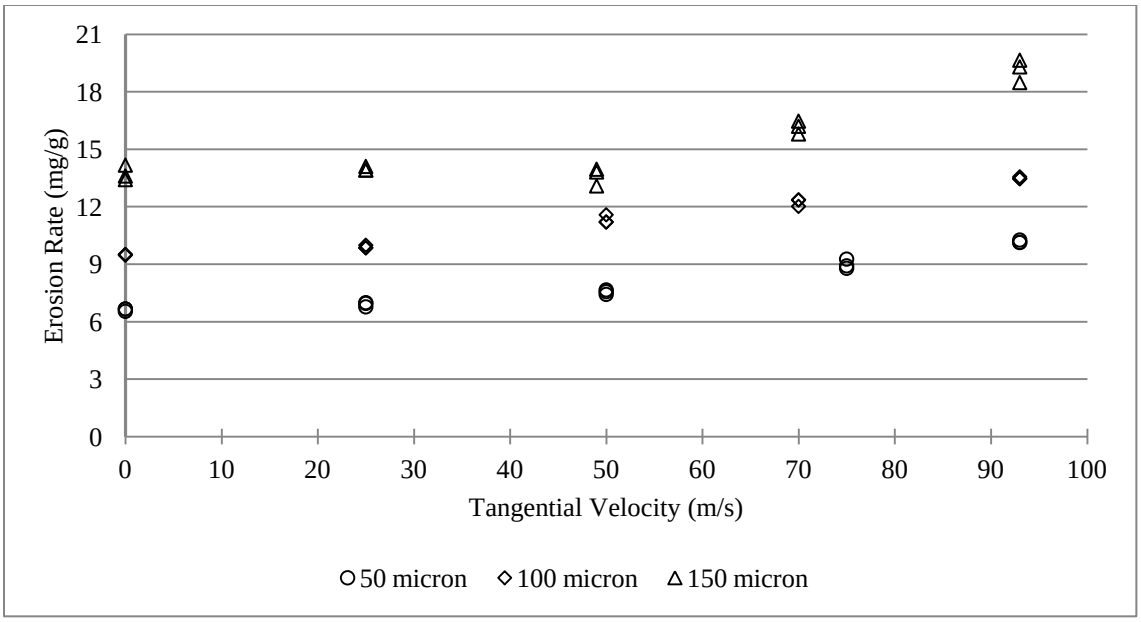

Figure E-3: Mass loss measurements of erosion rate vs. tangential velocity plot for three different alumina particle sizes i.e., 50, 100, and 150 µm at 70 m/s constant normal velocity.

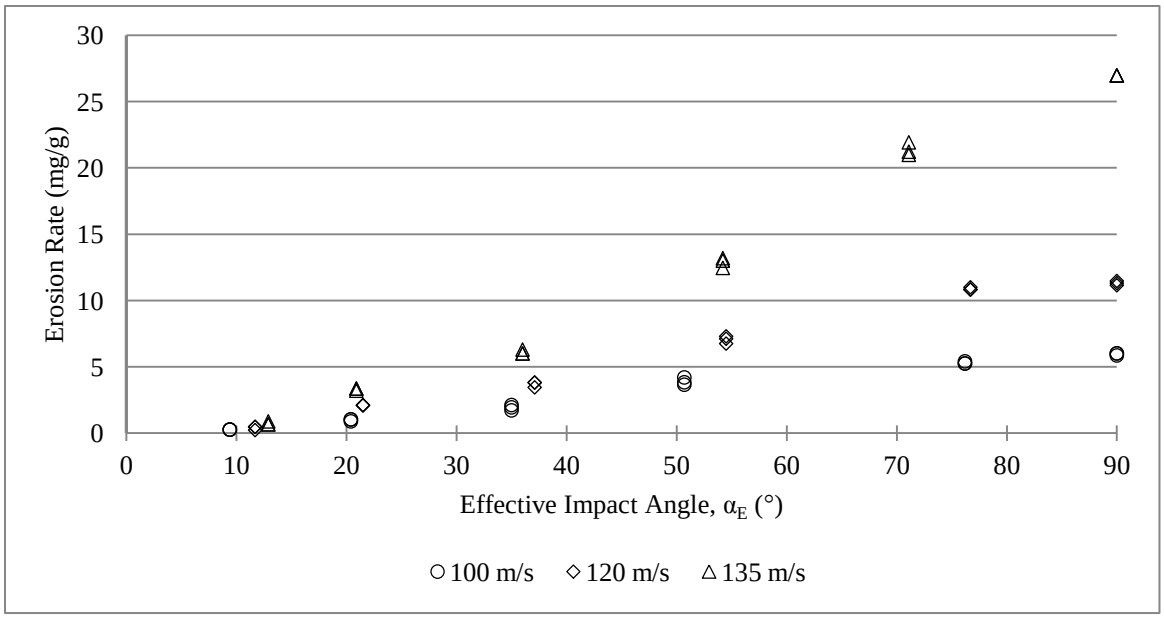

Figure E-4: Mass loss measurements of erosion rate vs. effective impact angle for borosilicate glass impacted by 50 µm alumina with constant total velocity of 100, 120, and 135 m/s.

Appendix F: Surface Roughness Measurements

The surface roughness of the samples at the centre of the eroded channel used in the erosion rate vs. tangential velocity experiments (Section 5.1) were measured using the optical profilometer to determine whether roughness was affected by the tangential component of velocity. Since the surface roughness depends on the cut-off or selection to separate roughness from waviness [59], a Gaussian filter of 250 µm was used throughout the roughness measurements as recommended in Ref. [59]. A sample length of 12 mm along the centre of the channel was selected. Both the arithmetic average roughness (R_a) and the root mean square (RMS) roughness (R_q) were measured. Arithmetic average roughness (R_a) was measured because it is the most commonly used, statistically stable, and repeatable parameter [71]. The RMS roughness (R_q) was measured due to its sensitivity to peaks and valleys [71]. Figure F-1 and F-2 show the average roughness and RMS roughness respectively as a function of tangential velocity for two constant normal velocities i.e., 75 and 121 m/s. Although both roughnesses increased with a normal velocity increase from 75 to 121 m/s, there was no apparent correlation with a tangential velocity increase of 93 m/s.

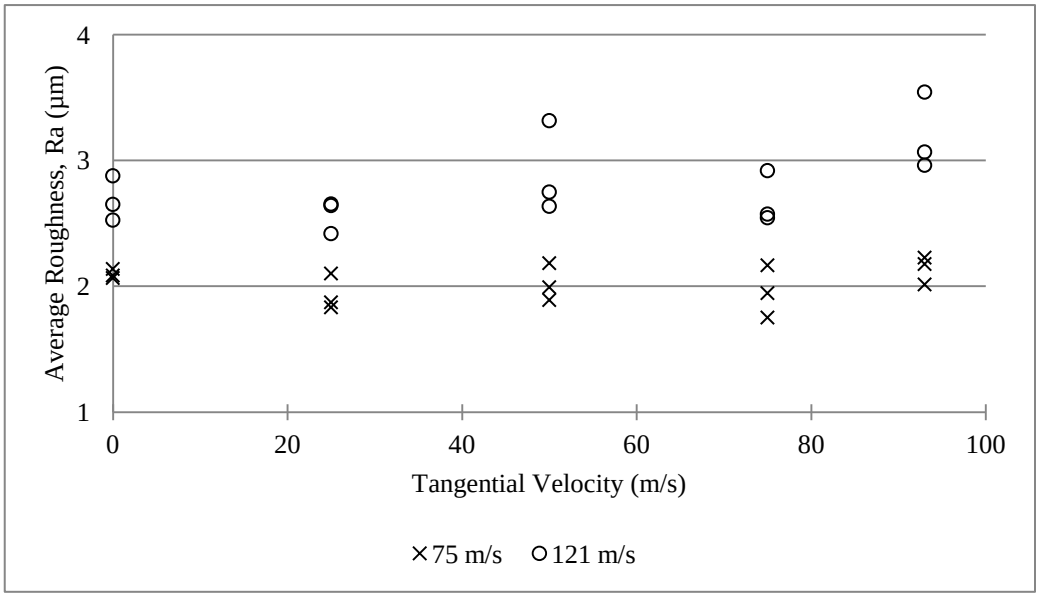

Figure F-1: Arithmetic average roughness vs. tangential velocity for 75 and 121 m/s constant normal velocity using 50 µm alumina.

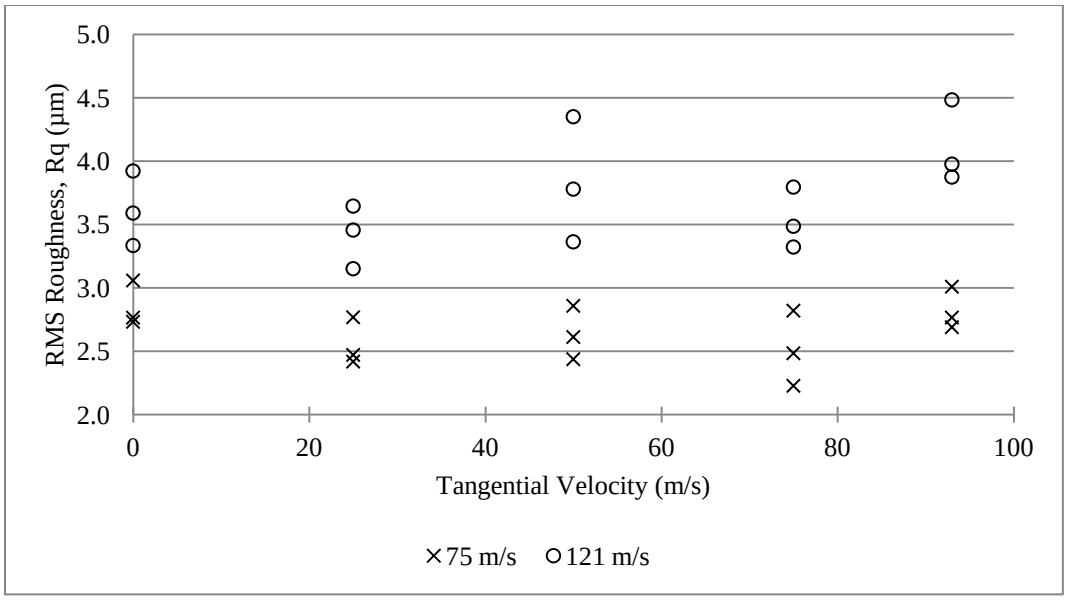

Figure F-2: RMS roughness vs. tangential velocity for 75 and 121 m/s constant normal velocity using 50 µm alumina.

Both roughness parameters were plotted against tangential velocity in Figures F-3 and F-4. As expected, the roughness increased with the particle size increase. Larger particles indent deeper and chip away more material than the smaller ones. Although the roughness increases with particle size, it again did not show a correlation with the tangential velocity. It can thus be concluded that the surface roughness was independent of tangential velocity component, and depended solely on the normal component of the kinetic energy.

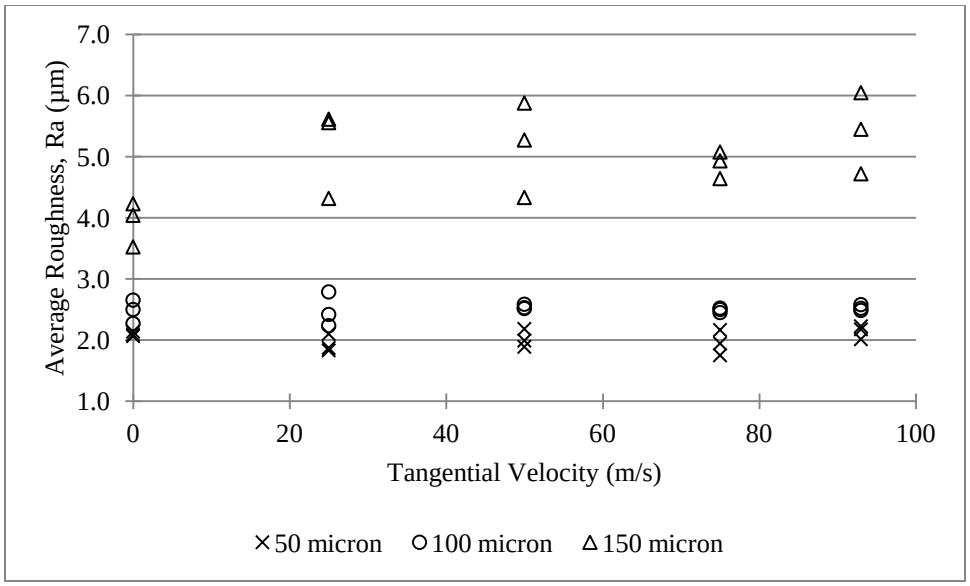

Figure F-3: Average roughness vs. tangential velocity for three different particle sizes i.e., 50, 100, 150 µm alumina at 75 m/s constant normal velocity.

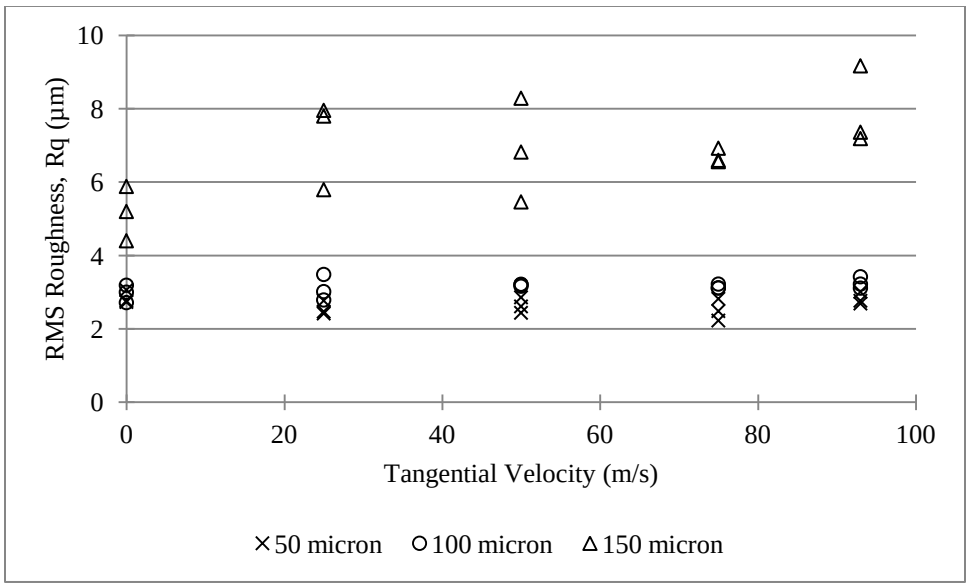

Figure F-4: RMS roughness vs. tangential velocity for three different particle sizes i.e., 50, 100, 150 µm alumina at 75 m/s constant normal velocity.

References

[1] A. Ghobeity, T. Krajac, T. Burzynski, M. Papini, J.K. Spelt, Surface evolution models in abrasive jet micromachining, *Wear 264* (2008) 185–198.

[2] P.J. Slikkerveer, P.C.P. Bouten, F.H. in‘t Veld, H. Scholten, Erosion and damage by sharp particles, *Wear 217* (1998) 237–250.

[3] P.J. Slikkerveer, F.H. in’t Veld, Model for patterned erosion, *Wear 233–235* (1999) 377–386.

[4] P.J. Slikkerveer), P.C.P. Bouten, F.C.M. de Haas, High quality mechanical etching of brittle materials by powder blasting, *Sensors and Actuators 85* (2000) 296–303.

[5] H. Wensink, M.C. Elwenspoek, A closer look at the ductile–brittle transition in solid particle erosion, *Wear 253* (2002) 1035–1043.

[6] Y.I. Oka, S. Mihara, T. Yoshida, Impact-angle dependence and estimation of erosion damage to ceramic materials caused by solid particle impact, *Wear 267* (2009) 129–135.

[7] I. Finnie, J. Wolak, T. Kabil, Erosion of metals by solid particles, *J. Mater. 2* (1967) 682–700.

[8] E. Rodriguez, M. Flores, A. Perez, R.D. Mercado-Solis, R. Gonzaliez, Erosive wear by silica sand on AISI H13 and 4140 steels, *Wear 267* (2009) 2109-2115.

[9] S. Ally, *Master’s Thesis*, Ryerson University, 2011.

[10] H. Getu, A. Ghobeity, J.K. Spelt, M. Papini, Abrasive jet micromaching of polymethylmethacrylate (PMMA). *Wear 263* (2007) 1008-1015.

[11] H. Getu, A. Ghobeity, J.K. Spelt, M. Papini, Abrasive jet micromachining of acrylic and polycarbonate polymers at oblique angles of attack, *Wear 265* (2008) 888-901.

[12] H. Getu, J.K. Spelt, M. Papini, Cryogenically assisted abrasive jet micromachining

of polymers, *Journal of Micromechanics and Microengineering18* (2008) 115010.

[13] H. Getu, J.K. Spelt, M. Papini, Thermal analysis of cryogenically assisted abrasive jet micromachining of PDMS. *International Journal of Machine Tools & Manufacture 51* (2011) 721–730

[14] A.G. Gradeen, J. K. Spelt, M. Papini, Cryogenic abrasive jet machining of polydimethylsiloxane at different temperatures, *Wear* 274–275 (2012) 335–344.

[15] A.G. Pawlowski, E. Belloy, A. Sayah, M.A.M. Gijs, Powder blasting patterning technology for micro fabrication of complex suspended structures in glass, *Microelectron. Eng.* 67–68 (2003) 557–565.

[16] D. Belder, F. Kohler, M. Ludwig, K. Tolba, N. Piehl, Coating of powder-blasted channels for high-performance microchip electrophoresis, *Electrophoresis* 27 (2006) 3277–3283.

[17] C. Iliescu, F.E.H. Tay, Wet Etching of Glass, *Semiconductor Conference*, 1 (2005) 35-44.

[18] E. Belloy, A.G. Pawlowski, A. Sayah, M.A.M. Gijs, Microfabrication of high-aspect ratio and complex monolithic structures in glass, *J. Microelectromech. Syst. 11 (5)* (2002) 521–526.

[19] J.H.M. ten ThijeBoonkkamp, J.K.M. Jansen, An analytical solution for mechanical etching of glass by powder blasting, *J. Eng. Math*. 43 (2002) 385–399.

[20] A.J. Burnett, S.R. De Silva, A.R. Reed, Comparisons between 'sand blast' and 'centripetal effect accelerator' type erosion testers, *Wear 186–187* (1995) 168–178.

[21] S. Srinivasan, R. O. Scattergood, On lateral cracks in glass, *Journal Of Materials Science 22* (1987) 3463-3469.

[22] Y. A. Ballout, J.A. Mathis, J.E. Talia, Effect of particle tangential velocity on erosion ripple formation, *Wear 184* (1995) 17-21.

[23] Y. A. Ballout, J. A. Mathis, J.E. Talia, Solid particle erosion mechanism in glass, *Wear 196* (1996) 263-269.

[24] M. Talia, H. Lankarani, J.E. Talia, New experimental technique for the study and analysis of solid particle erosion mechanisms, *Wear 225–229* (1999) 1070–1077.

[25] S. Soderberg, S. Hogmark, U. Engmant, H. Swahnt, Erosion classification of materials using a centrifugal erosion tester. *Tribology International 14 (6)* (1981) 333-343.

[26] I. Kleis, K. Priit, Experimental Study of Erosion Characteristics. Solid Particle Erosion: Occurrence, Prediction and Control. London: Springer-Verlag London Limited, (2008) pp 1-47.

[27] A.J. Burnett, M.S.A. Bradley, D.J. O'Flynn, T. Deng, M.S. Bingley, Anomalies in the results obtained from rotating disc accelerator erosion testers: a discussion of possible causes, *Wear 233–235* (1999) 275–283.

[28] T. Deng, M.S.A. Bradley, M.S. Bingley, An investigation of particle dynamics within a centrifugal accelerator type erosion tester, *Wear 247* (2001) 55–65.

[29] T. Deng, M.S. Bingley, M.S.A. Bradley, Influence of particle dynamics on the erosion test conditions within the centrifugal accelerator type tester, *Wear 249* (2001) 1059–1069.

[30] J. Li, T. Deng, M.S. Bingley, M.S.A. Bradley, Prediction of particle rotation in a centrifugal accelerator erosion tester and the effect on erosion rate, *Wear 258* (2005) 497–502.

[31] T. Deng, M. S. Bingley, M. S. A. Bradley, Understanding particle dynamics in erosion testers- A review of influences of particle movement on erosion test conditions, *Wear 267* (2009) 2132–2140.

[32] Y. Petukhov, H. Kalman, A new apparatus for particle impact tests, *Part. Part. Syst. Charact. 20* (2003) 267-275.

[33] T. Poppe, J. Blum, Th. Henning, Generating a jet of deagglomerated small particles in vacuum, *Rev. Sci. Instrum. 68 (6)* (1997) 2529-2533.

[34] Y.I. Oka, H. Ohnogi, T. Hosokawa,M. Matsumura, The impact angle dependence of erosion damage caused by solid particle impact, *Wear 203–204* (1997) 573-579.

[35] D. Aquaro, E. Fontani, Erosion of ductile and brittle materials, *Meccanica 36* (2002) 651–661.

[36] I.M. Hutchings, Ductile–brittle transitions and wear maps for the erosion and abrasion of brittle materials. *J. Phys. D 25* (1992) A212–A221.

[37] Y.I. Oka, K. Okamura, T. Yoshida, Practical estimation of erosion damage caused by solid particle impact. Part 1: Effects of impact parameters on a predictive equation, *Wear 259* (2005) 95–101.

[38] Y.I. Oka, T. Yoshida, Practical estimation of erosion damage caused by solid particle impact. Part 2: Mechanical properties of material directly associated with erosion damage, *Wear 259* (2005) 102-109.

[39] Z. Feng, A. Ball, The erosion of four materials using seven erodents – towards an understanding, *Wear 233–235* (1999) 674–684.

[40] M.A. Verspui, Modelling Abrasive Processes of Glass, *PhD thesis*, Technische Universitieit Eindhoven, 1998.

[41] M. Buijs, J.M.M. Pasmans, Erosion of glass by alumina particles: transitions and exponents, *Wear 184* (1995) 61-65.

[42] J. H. Neilson, A. Gilchrist, Erosion by a stream of solid particles, *Wear II* (1968).

[43] M.A. Verspui, G. de With, A. Corbijn, P.J. Slikkerveer, Simulation model for the erosion of brittle materials, *Wear 233–235* (1999) 436–443.

[44] G.Z. Wang, J.H. Chen, Z.H. Li, Further study on the mechanism of the ductile-to-brittle fracture transition in C-Mn base and weld steel, *Metallurgical and materials transactions28A* (1997).

[45] G.L. Sheldon, I. Finnie, On the ductile behaviour of nominally brittle materials during erosive cutting, *J. Eng. Ind. 88* (1966) 387–392.

[46] I. Finnie, Erosion of surfaces by solid particles, *Wear 3* (1960) 87–103.

[47] J.G.A. Bitter, A study of erosion phenomena, part I, *Wear 6* (1986) 5–21.

[48] J.G.A. Bitter, A study of erosion phenomena, part II, *Wear 8* (1986) 169–190.

[49] M. Papini and J. K. Spelt, Impact of rigid angular particles with fully plastic targets- Part I: Analysis, *International Journal of Mechanical Sciences* 42 (5), (2000), 991-1006.

[50] M. Papini, and J. K. Spelt, Impact of rigid angular particles with fully plastic targets- Part II: Parametric study of erosion phenomena, *International Journal of Mechanical Sciences* 42 (5), (2000), 1007-1025.

[51] D. Ciampini, J.K. Spelt and M. Papini, Simulation of interference effects in particle streams following impact with a flat surface, Part I: Theory and analysis, *Wear* 254 (2003) 237-249.

[52] D. Ciampini, J.K. Spelt and M. Papini, Simulation of interference effects in particle streams following impact with a flat surface, Part II: Parametric study and implications for erosion testing and blast cleaning, *Wear* 254 (2003) 250-264.

[53] C. Gomes Ferreira, D. Ciampini, and M. Papini, The effect of inter-particle collisions in erosive streams on the distribution of energy flux incident to a flat surface, *Tribology International* 37 (2004) 791-807.

[54] T. Burzynski and M. Papini, Analytical models of the interference between incident and rebounding particles within an abrasive jet: Comparison with computer simulation, *Wear* 263(7-12), (2007), 1593-1601.

[55] A. Ghobeity, D. Ciampini, M. Papini, An analytical model of the effect of particle size distribution on the surface profile evolution in abrasive jet micromachining, *Journal of Materials Processing Technology 209* (2009) 6067–6077

[56] T Burzynski and M Papini, Measurement of the particle spatial and velocity distributions in micro-abrasive jets, *Meas. Sci. Technol. 22* (2011) (15pp)

[57] T. Burzynski, M. Papini, Analytical model of particle interference effects in divergent erosive jets, *Tribol. Int.* 43 (3) (2010) 554-567.

[58] A. Ghobeity, H. Getu, T. Krajac, J.K. Spelt, M. Papini, Process repeatability in abrasive jet micro-machining, *Journal of Materials Processing Technology 190* (2007) 51–60.

[59] R. Haj Mohammad Jafar, J.K. Spelt, M. Papini, Surface roughness and erosion rate of abrasive jet micro-machined channels: Experiments and analytical model, submitted to the *Journal of Wear* (2012).

[60] T. Burzynski, M. Papini, Analytical models of the interference between incident and rebounding particles within an abrasive jet: Comparison with computer simulation, *Wear* 263 (7-12) (2007) 1593-1601.

[61] D. Ciampini, J.K. Spelt, M. Papini, Simulation of interference effects in particle streams following impact with a flat surface, Part II: Parametric study and implications for erosion testing and blast cleaning, *Wear* 254 (2003) 250–264.

[62] "SCHOTT BOROFLOAT ® 33" SCHOTT North America Inc., (2012) Web. 25 Aug. 2012. <www.us.schott.com/borofloat/english/download/borofloat_brochure_2010.pdf>

[63] D. Dehnadfar, J. Friedman, M. Papini, Laser shadowgraphy measurements of abrasive particle spatial, size and velocity distributions through micro-masks used in abrasive jet micro-machining, *Journal of Materials Processing Technology 212* (2012) 137– 149.

[64] D. Dehnadfar, *Master's Thesis,* Ryerson University, 2011.

[65] H. Li, J. Wang, J. Fan, Analysis and modelling of particle velocities in microabrasive air jet, *International Journal of Machine Tools & Manufacture* 49 (2009) 850-858.

[66] S. M. Wiederhom, B. R. Lawn, B. J. Hockey, Effect of particle impact angle on strength degradation of glass, *J . Am. Ceram.* Soc., 62 (1979) 639-645.

[67] H. Uuemois, I. Kleis, A critical analysis of erosion problems which have been little studied, *Wear 31* (1975) 359–371.

[68] R.G. Budynas, J.K. Nisbett, J.E. Shigley, Shigley's mechanical engineering design, 9th ed. New York: McGraw-Hill, 2011.

[69] "Loaded Flat Plates" RoyMech Index page. N.p., n.d. Web. 24 Aug. 2012. <http://www.roymech.co.uk/Useful_Tables/Mechanics/Plates.html>

[70] N. T. M. Dennis, T. A. Heppell, Vacuum system design, London: Chapman & Hall, 1968.

[71] "Basic Components & Elements of Surface Topography." B. C. Macdonald & Co., (2007) Web. 1 Nov. 2012. <http://www.bcmac.com/pdf_files/surface%20finish%20101.pdf>